The role of sodium and calcium permeable T-type channels in generating pacemaking currents in invertebrates

by

Jennifer Czekus

A thesis
presented to the University of Waterloo
in fulfillment of the
thesis requirement for the degree of
Master of Science
in
Biology

Waterloo, Ontario, Canada, 2016

Author's Declaration

I hereby declare that I am the sole author of this thesis. This is a true copy of the thesis, including any required final revisions, as accepted by my examiners.

I understand that my thesis may be made electronically available to the public.

Abstract

T-type calcium channels (Cav3) play a key role in generating rhythmic action potentials in excitable cells such as the heart pacemaker and sleep-wake cycles in the thalamus. T-type channels are low voltage-activated channels, which can be opened near rest to cause an inward current that leads to membrane voltage rising to threshold to generate rhythmic action potential firing. The upstroke of the ventricular action potential in the vertebrate heart is attributed mostly to the cardiac-specific voltage-gated sodium channel, Nav1.5. Sodium channels are not expressed in the invertebrate heart, such as *Lymnaea stagnalis*. Instead, the major inward conductances of the invertebrate heart are due to voltage-gated calcium channels. The invertebrate pond snail, *Lymnaea stagnalis*, heart expresses T-type calcium channel, LCav3, which is alternatively-spliced in exon 12, generating a highly sodium selective T-type channel (with exon 12a) compared to a more calcium ion selective channel isoform (with exon 12b). The sodium permeant, LCav3-12a channel is the only T-type channel expressed in the heart, while LCav3-12b is more exclusive to the secretory glands, such as prostate and albumen. Our goal is to understand the functional consequence of differing sodium and calcium ion selectivities of T-type channels for the generation of rhythmic pacemaking in native tissues by conducting elecrophysiology experiments on dissociated ventricle cells and constructing a qualitative mathematical model of the invertebrate ventricular action potential. Mathematical models for both LCav3-12a and LCav3-12b T-type currents were constructed and implemented using current models from the Kyoto model, a guinea pig ventricular action potential model, to reflect the currents found in *Lymnaea stagnalis*. LCav3-12b had a smaller pacemaking current and showed slower rate of spike generation opposed to LCav3-12a which had a larger current and faster pacemaking activity. Spiking activity was not abolished with simulated T-type current block but had the greatest effect on rate of pacemaking. Simulations involving reduced current conductance or varying ion concentration show that LCav3 was primarily responsible for generating pacemaking activity and initiating the action potential upstroke.

Acknowledgements

I would first like to express my gratitude to my two supervisors, Dr. J. David Spafford and Dr. Sue Ann Campbell. Both of your continuous support and guidance through this project have not only taught me the skills of academia, but as a critical thinker. Your contagious curiosity has taught me to always question and push your limits one step further.

Thank you to my committee, Dr. Todd Holyoak and Dr. Brian Ingalls, for taking the time to read this thesis. Your advice through these finals steps is truly appreciated. Thank you to Dr. Tyler Dunn for the daily technical support in order to set up our brand new recording system.

To my fellow and former lab mates Robert Stephens, Amrit Mehta and David Weiler, thank you for your patience in teaching me the basics of working in a biology lab and lending your expertise when times were tough. You have shown me the beauty of a communal "Eureka!" moment.

Finally, to those I hold closest. To my parents, thank you for your constant encouragement and motivation to reach one step further. To my partner, you have been my biggest cheerleader and believed in me when I didn't.

To all of those who have offered their support, I am truly grateful.

Dedication

To my family,

those who I have chosen

and those who have chosen me.

Table of Contents

List of Tables

List of Figures

1 Introduction

1.1 Cardiac Electrophysiology

The human heart beats at a steady rate of 60-100 beats per minute due to its own rhythmic capabilities (Gavaghan, 1998). The heart beat is caused by an electrical signal which is propagated throughout heart cells leading to contractions of muscular walls of the two atria followed by two ventricles (Gavaghan, 1998). The electrical signals, called both action potentials or spikes, are endogenously generated in specific pacemaker cells which pass their excitation through gap junctions (Boyett, 2009). Action potentials propagated through each cell are due to the movement of ions inside or outside the cell across its plasma membrane. A variety of channels are embedded within the membrane to control the movement of ions by opening and closing under specific conditions (Grant, 2009). Channel types vary by cell type reflecting the cell's role in propagating the signal. The conditions under which these channels opens and close as well as the ions they allow to pass cause them to play a specific role in carrying these electrical signals (Grant, 2009). A specific ion channel carrying a calcium current has been found primarily in cells responsible for initiating electrical signals (Hagiwara, Irisawa, & Kameyama, 1988). This channel is known as the T-type channel and has been isolated to characterize the biophysical features, however little is known of its physiological role in the signal responsible for heart contraction (Ono & Iijima, 2010).

The pond snail *Lymnaea stagnalis* has been used as a simple invertebrate model for electrophysiological studies, and features a discovery in T-type channels (Senatore, Guan, Boone, & Spafford, 2014). In 2014, Senatore *et al.* found two isoforms of the T-type channel, each of which are specific to some tissues and only differ in the ions each passes (Senatore et al., 2014).

The goal of the studies described in this thesis is to examine the physiological role of the T-type current in the snail heart action potential and compare the physiological difference between the two T-type channels isoforms by both conducting electrophysiology recording

experiments of snail heart cells and constructing a mathematical model of the *Lymnaea* cardiac action potential.

1.1.1 Cardiac Action Potentials

The electrical signals of the heart are initiated from a distinct pacemaking region near the top of the heart and propagated through a specific cardiac conduction system to result in the muscle contraction of a heart beat (Boyett, 2009). The signals propagate to the muscular walls of each of the four chambers in the heart. The two atria are chambers responsible for receiving blood returning from circulating in the body and pumping it into one of the two ventricles responsible for pumping blood back into systemic circulation (Gavaghan, 1998). Cells of the conduction system play one of three roles: pacemaking, signal transmission, or contraction. Pacemaking regions such as the sinoatrial (SA) node initiate a signal that is transmitted through the heart via cells capable of rapidly transmitting this signal. The signals are sent to contractile muscle cells of the atria and ventricles to generate the heart beat (Gavaghan, 1998).

Adjacent cells of the conduction system are connected by nonspecific ion channels called gap junctions. Gap junctions allow cells to be electrically coupled because ions may flow from one cell directly into another (Ahir & Pratten, 2014). This method for transmission of electrical signals is responsible for rapid signal propagation throughout the cardiac conduction system and coordinated instantaneous cell contraction for a heart beat (Ahir & Pratten, 2014).

A signal is generated because of an electrical and chemical gradient caused by a difference in ionic concentration between the inside and outside of the cell (Hille, 2001). The signal is represented as a change in voltage (also called potential) between the inside and outside of the cell. The signal consists of an increase in voltage called *depolarization* followed by a decrease in voltage called *repolarization* or *hyperpolarization* (Hille, 2001). This creates a time trace of the voltage with a distinctive shape which is called an action potential or

spike. The influence of both concentration and charge inside and outside the cell dictate the electrochemical gradient and the direction of ion flow. If the concentration of an ionic species is higher inside the cell than outside, an outward moving ion current will be generated; conversely if there is a larger concentration outside the cell than inside, an inward moving ionic current will be generated. Given a set internal and external ion concentration, the voltage at which the current may change direction is the Nernst potential. This potential is further discussed in section 1.3. Ions may not freely pass through the lipid bilayer and require passage through gated transmembrane ion channels (Hille, 2001).

Ion channel behaviour is dictated by opening and closing mechanisms that may be voltage, stretch, or ligand dependent (Hille, 2001). The majority of channels are voltage dependent and typically open upon depolarization and close with time. Channels have activation mechanisms and inactivation mechanisms controlled by physical gates (Hille, 2001). At rest, channels are in a deactivated state. Here, their inactivation gate is open but their activation gate is closed. Upon depolarization, activation gates open and ions are able to flow through the channel. With time and continued depolarization, the inactivation gate closes while the activation gate remains open, closing the channel from passing current and putting it into an inactive state (Hille, 2001). After repolarization of the cell, the membrane potential returns to rest where inactivation gates open and activation close putting it back into a deactivated state (Hille, 2001). This is the common mechanism of opening and closing of voltage dependent gates found in excitable cardiac cells (Hille, 2001).

As the electrical signal is transmitted from cell to cell, the shape of the action potential varies (Monfredi, Dobrzynski, Mondal, Boyett, & Morris, 2010) but each action potential spike is generated in a similar way. Each signal is initiated by the cell voltage increasing due to positive ions entering the cell until a threshold level is reached opening a large enough fraction of channels to initiate an action potential. The coordination of these channels opening at this threshold level allows sodium and calcium ions to enter the cell causing an increase in voltage responsible for generating the upstroke of the action potential in the cell (Hille,

2001). The action potential is then terminated by repolarization as sodium and calcium ions no longer enter the cell and potassium ions leave the cell (Hille, 2001). The duration and shape of this spike varies based on cell type due to differences in ion channel expression in order to perform different physiological roles (Monfredi et al., 2010).

The ventricular muscle cell action potential features a longer spike of about 200 ms (Grant, 2009) contrary to neuronal impulses lasting only a few miliseconds (Hille, 2001). This prolonged action potential features four distinct phases (Figure 1.1). During each of these phases, the permeability to sodium, calcium and potassium change to depolarize and repolarize the cell. Phase 4 is the resting membrane potential which is stable (Grant, 2009). At rest, the cell is impermeable to sodium ions but permeable to potassium ions. Potassium ions leak out of the cell through ion channels carrying the inward rectifier current I_{K1} which keeps the potential at a stable resting potential (Nattel & Carlsson, 2006) and prevents spontaneous action potential generation (Grant, 2009). The cell remains in this phase until an impulse arrives from an adjacent cell (Grant, 2009).

Phase 0 consists of the rapid upstroke after the threshold voltage is reached (Figure 1.1) (Nattel & Carlsson, 2006). Sodium channels open briefly (< 1 ms) after threshold and close quickly with time as they inactivate (Grant, 2009). The rapid depolarization from sodium channels is responsible for rapid action potential propagation to adjacent cells, with the wave of depolarization traveling at roughly 1 $\frac{m}{s}$ across the ventricles (Grant, 2009).

After phase 0, potassium currents begin to activate. Immediately after the upstroke, the transient outward current, I_{to}, activates briefly to cause phase 1, the early or transient repolarization (Figure 1.1) (Nattel & Carlsson, 2006). Soon after, calcium ions enter the cell via the L-type calcium current and potassium ions continue to exit the cell via the ultra rapid potassium current, I_{Kur}. During this phase the cell is able to contract because of the influx of calcium (Nattel & Carlsson, 2006). Calcium entering the cell causes further release of calcium from sarcoplasmic reticulum calcium stores inside the cell to prolong contraction (Hille, 2001) These two currents are approximately equal and opposite causing little change

in the membrane potential. This results in phase 2, the plateau phase of the action potential (Nattel & Carlsson, 2006).

After some time, the L-type calcium current inactivates and the delayed rectifier potassium currents activate. With no activated inward current, the rapid and slow delayed rectifier currents, I_{Kr} and I_{Ks} activate to bring the cell to the resting potential during phase 3, repolarization (Figure 1.1) (Nattel & Carlsson, 2006). As the cell returns to rest, ion pumps and exchangers return sodium and calcium ions to the outside of the cell and potassium to the inside of the cell. Potassium is brought in as sodium is expelled via the sodium-potassium pump, and calcium is returned to the outside via the sodium-calcium exchanger (NCX) which brings sodium ions inside and calcium ions outside of the cell (Nattel & Carlsson, 2006). The cell then remains at rest until stimulated by another depolarizing wave.

The SA node action potential features its own phases different from the ventricular action potential. Rhythm generating cells do not possess a stable resting potential but an unstable pacemaker potential due to small inward currents. After an action potential as the potassium currents causing repolarization decay, the hyperpolarized activated channel (HCN) opens. The current is named the "funny" current, I_f, because of its atypical mechanism of opening upon hyperpolarization opposed to depolarization which slowly depolarizes the cell after final repolarization (Monfredi et al., 2010). I_{K1} in ventricle cells prevent a pacemaker potential by keeping the cell at its resting membrane potential. Pacemaking cells do not have this current and I_f is free to depolarize the cell (Grant, 2009).

Pacemaker cells also possess a sodium-calcium exchanger. Three sodium ions are pumped into the cell and one calcium ion is pumped out, causing a net inward current (Monfredi et al., 2010). This inward current also contributes to the pacemaker potential once the funny current has been activated (Monfredi et al., 2010).

The calcium channels are the last to activate in the pacemaker potential. After the NCX and I_f has depolarized the cell, the low voltage-activated transient T-type calcium current carries the pacemaker potential to the activation voltage of the high voltage-activated L-type

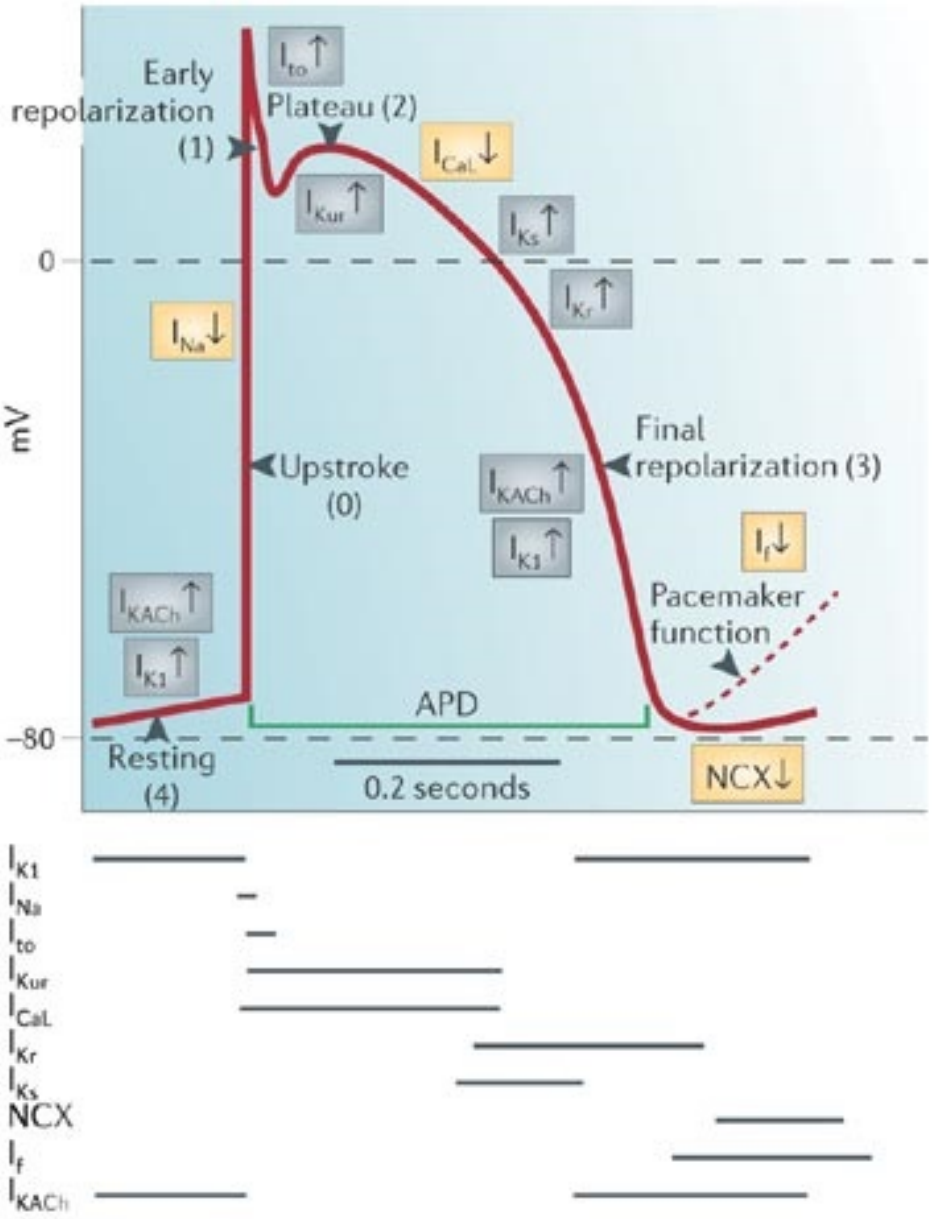

Figure 1.1: Ionic currents during a ventricular action potential. (*Top*): Voltage-time plot of a ventricular action potential. Currents responsible for each phase are shown in boxes. Blue boxes indicate outward currents and yellow boxes indicate inward currents. Each phase is labeled in brackets. The action potential duration (APD) is between the upstroke and return to resting potential, lasting approximately 200 ms. The dotted line indicates the pacemaker function carried by I_f found only in SA node to compare to the resting potential of ventricular cells. The acetylcholine activated potassium current I_{KAch} is also highly expressed in pacemaking cells where, when activated by binding of acetylcholine, causes an outward K^+ current countering the inward I_f current. This slows spike frequency by making it more difficult to reach threshold. (*Bottom*): Horizontal lines indicate time during the action potential above that each current is activated. (Nattel & Carlsson, 2006)

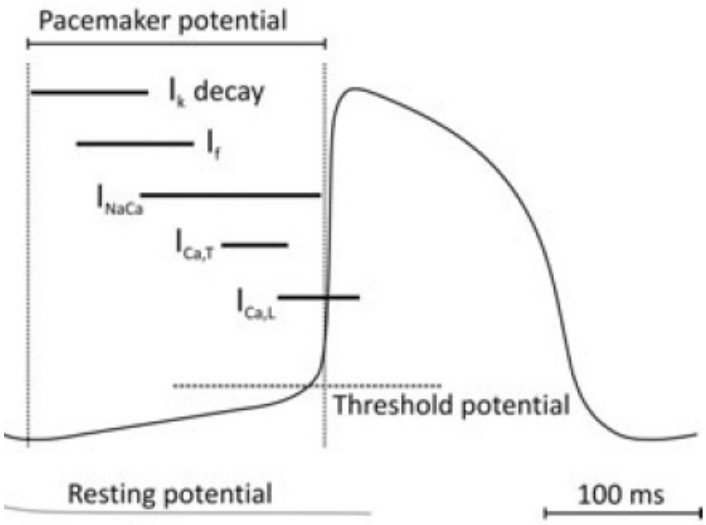

Figure 1.2: Action potential shape from the SA node and the currents contributing to the characteristic pacemaker potential. The pacemaker potential replaces the resting membrane potential found in ventricle cells. As the potassium currents causing repolarization decay, inward currents are activated to cause a slow rise in potential until threshold. First the funny current, I_f, activates by hyperpolarization from the repolarization phase of the previous action potential. The Na-Ca exchanger exchanges sodium and calcium ions creating a net inward current. These currents raise the potential to threshold for the T-type calcium channel to activate, and finally the L-type calcium current until threshold for an action potential is reached. The upstroke is then carried by the L-type calcium channel until it inactivates. The delayed rectifier potassium currents activate to repolarize the cell and drive the potential down causing I_f to activate once again. (Monfredi et al., 2010)

calcium current (Monfredi et al., 2010). The L-type current carries the pacemaker potential to threshold where it is also responsible for the upstroke. Sodium channels are absent from pacemaking cells, therefore the upstroke is due only to calcium influx (Monfredi et al., 2010). Pacemaker cells lack a plateau phase since they are not involved in contraction, and the cell repolarizes by activated delayed rectifier potassium currents as L-type currents inactivate with time (Monfredi et al., 2010).

Each ionic current in the cardiac conduction system plays a physiological role in generating the action potential propagated from cell to cell, however the physiological roles of some of these individual currents is not yet known. The recently discovered T-type current has been a key area of interest as it is found almost exclusively in pacemaking cells and is linked

to rhythmic disorders such as epilepsy (Cheong & Shin, 2013) and arrhythmias (Vassort, Talavera, & Alvarez, 2006).

1.1.2 T-Type Calcium Channels

T-type channels were first described by Hagiwara et al., 1988. Previously, the difference between T-type and L-type calcium channel currents was unknown and they were considered a single calcium current (Kakei, Noma, & Shibasaki, 1985). Because of the rapid kinetics of T-type currents and slow inactivation of L-type currents passing barium, the single calcium current commonly referred to the L-type current only. In 1988, Hagiwara et al. proved the calcium current was composed of two currents active at different potentials.

Hagiwara et al. performed whole cell voltage clamp experiments on rabbit sinoatrial node cells. To isolate the calcium currents, tetrodotoxin (TTX) was used to block sodium currents and Cs^{+} was used to block delayed rectifier currents. The two calcium currents were separated from each other with two different holding potentials, and two series of experiments were perfomed. In one series, the cell was held at -80 mV with voltage steps taken up to -40 mV; in the second series, the cell was held at -40 mV with voltage steps takes up to 20 mV (Hagiwara et al., 1988).

Voltage steps taken from -80 mV holding potential revealed a rapidly activating and decaying inward current which activated between -60 mV to -50 mV and peaked at -10 mV. The current was completely inactivated at potentials more positive than -40 mV (Hagiwara et al., 1988). Voltage steps taken from -40 mV revealed the conventional slow decaying current that was previously referred to as the calcium current (Hagiwara et al., 1988).

To ensure that the low voltage-activated current was carried by calcium, the experiments were performed again with Ba^{2+} replacing Ca^{2+}, and again in Na^{+} free solution containing Ca^{2+}. The low voltage-activated current possessed the same rapid kinetics in all three experiments while the high voltage-activated current displayed slower inactivation in Ba^{2+} solution than Ca^{2+} (Hagiwara et al., 1988). This difference of inactivation kinetics in Ba^{2+} solution

gave rise to the clear separation of two individual calcium currents: the low voltage-activated **t**ransient **T**-type calcium current and the high voltage-activated **l**ong-lasting **L**-type calcium current (Hagiwara et al., 1988).

The T-type calcium channel is characterized by its low voltage activation and transient kinetics (Ono & Iijima, 2010; Perez-Reyes, 2003; Senatore, Zhorov, & Spafford, 2012). T-type currents are also known for having a small and tiny conductance compared to the long lasting L-type calcium current (Senatore et al., 2012). Initial single channel recordings in rabbit sinoatrial node cells compared single channel conductance between T-type and L-type calcium channels in identical conditions. The T-type channel had approximately 8.5 pS conductance compared to 16.0 pS of the L-type channel, showing its smaller conductance relative to the L-type calcium channel (Hagiwara et al., 1988). Experiments using barium instead of calcium in the external solution contrast the kinetics between the two channels. The T-type current could only be observed within the 30 ms of a test pulse compared to the L-type current which continued to show activity over the full 300 ms recording (Hagiwara et al., 1988). Unlike the L-type calcium current, T-type currents are not inactivated by calcium and display rapid kinetics in both calcium and barium solutions (Perez-Reyes, 2003). Three variations of T-type channels may be expressed in human cells: $Ca_v3.1$, $Ca_v3.2$ and $Ca_v3.3$. $Ca_v3.1$ and $Ca_v3.2$ have similar kinetics and differ in pharmacological sensitivities to blockers, while $Ca_v3.3$ is the slowest T-type (Perez-Reyes, 2003; Senatore et al., 2014).

T-type channels are able to contribute to pacemaking activity because of their window current (Senatore et al., 2012). Window currents occur when the channel's activation and inactivation properties allow some channels to activate while the majority of channels are inactivated near the resting potential (Senatore et al., 2012). For T-type currents, this window current peaks near the resting potential where approximately 1-2% of the channels are able to open (Senatore et al., 2012). Calcium ions are able to leak into the cell through these few open channels and depolarize the cell slowly. This leak is hypothesized to contribute to the pacemaker current of spontaneously active cells (Senatore et al., 2012; Perez-Reyes,

2003), secretion in endocrine cells, and even contraction of smooth muscle cells (Perez-Reyes, 2003).

T-type channels have been found in various tissues such as muscle, neurons, heart and kidney where they are believed to play roles in pacemaking and secretion (Perez-Reyes, 2003). In the thalamus, $Ca_v3.1$ and $Ca_v3.3$ T-type channels are found in neurons responsible for non-REM sleep where they activate at low potentials to depolarize the cell to generate low threshold spikes that lead to burst firing and oscillatory behaviour (Perez-Reyes, 2003; Lambert, Bessaïh, Crunelli, & Leresche, 2014). Neurological disorders linked to T-type channels include absence epilepsy, tremors from Parkinson's disease, and neurogenic pain (Perez-Reyes, 2003). $Ca_v3.3$ is also notable because it is not found in the cardiovascular system (Lambert et al., 2014). Endocrine cells rely on T-type and L-type calcium currents to generate spontaneous spikes and carry the inward current in action potentials leading to excitation-secretion coupling since they lack sodium channels (Perez-Reyes, 2003). Excitation-secretion coupling requires an action potential to increase cytosolic calcium from L-type calcium currents or released from calcium stores within the cell (Misler, 2009). Pancreatic β cells rely on the low voltage activation of T-type currents to begin the oscillatory pacemaking behaviour needed for insulin secretion (Perez-Reyes, 2003).

T-type channels are found in abundance in pacemaking cells of the human heart yet are nearly undetectable in ventricular myocytes (Ono & Iijima, 2010; Perez-Reyes, 2003). T-type channels are known to activate at negative potentials which overlap with the pacemaker potential of rhythm generating cells (Ono & Iijima, 2010). The density of T-type channels in pacemaker cells varies by species. As the size of the animal decreases the density of T-type calcium channels increases (Ono & Iijima, 2010). This may account for differences in heart rates where smaller creatures have a faster heart rate (Ono & Iijima, 2010). When T-type currents were blocked with nickel in the rabbit sinoatrial node there was marked reduction in firing frequency, however the pacemaker potential was not abolished (Ono & Iijima, 2010). It is also hypothesized that T-type channels contribute to pacemaking by activating the

sodium-calcium exchanger. The small amount of calcium entering the cell from the T-type current is enough to cause calcium induced calcium release from the calcium stores inside the cell necessary for contraction. The slight rise in internal calcium triggers the start of the net inward current produced by allowing 3 sodium ions inside the cell for every one calcium ion sent outside the cell which continues the pacemaker current (Ono & Iijima, 2010).

The physiological role of T-type currents in the action potential has been difficult to determine because of the lack of specific blockers (Ono & Iijima, 2010). Each isoform of the human T-type current features its own sensitivity to blockers leading to difficulties isolating each of these channels (Ono & Iijima, 2010). T-type channels blockers have also be found to block other calcium channels, preventing study on isolated T-type currents and their effect on the action potential (Ono & Iijima, 2010). Conclusions of previous studies now also need to be reconsidered because of the discovery of the calcium channel $Ca_v1.3$ that has similar low threshold activation and may have contaminated T-type current results (Ono & Iijima, 2010).

1.2 *Lymnaea stagnalis* as a Model Organism

The pond snail *Lymnaea stagnalis* is used as a model organism to study rhythm generation. This is due to both the ease of carrying out experiments relative to other invertebrates and mammalian cells, and the the simplicity of the organism both at the organ and molecular level.

Lymnaea stagnalis is favoured over *C. elegans* or *Drosophila* as the central nervous system and peripheral organs are larger and more accessible for examination. Individual adult snail neurons and other cells are much easier to culture *in vitro*, and possess properties that resemble properties *in vivo* (Syed, Ridgway, Lukowiak, & Bulloch, 1992). Snail cells form robust gigaseals for patch clamp and other electrophysiological recording, and the organism is larger. *Lymnaea* has a two chambered heart without a concentrated area of rhythm generation like SA node in human heart (Yeoman & Benjamin, 1999), and an open circulatory

system without a need for unidirectional pumping of blood via capillaries (Bekius, 1971). Blood is pumped into the body and diffuses to the tissues until it is collected again by the atrium and pumped to the ventricle (Bourne, Redmond, & Jorgensen, 1990). The two chambered heart allows simpler separation between one atrium and one ventricle opposed to the mammalian four chambered heart for culture of each tissue.

Invertebrates have less variation in channel types than vertebrates which results in a simpler action potential mechanism. For example, humans contain three variations of T-type currents: $Ca_v3.1$, $Ca_v3.2$, and $Ca_v3.3$, where *Lymnaea* possesses only one T-type channel, Ca_v3 (Senatore et al., 2014). These simplifications make it easier to study the physiological roles of families of currents in the action potential without the complexity of multiple isoforms of the same channel type.

1.2.1 Ion Channels of *Lymnaea stagnalis* ventricle cells

Four currents of *Lymnaea stagnalis* ventricle cells were first identified in 1999, two were identified by Yeoman & Benjamin, and two by Yeoman, Brezden & Benjamin. Four ionic currents were studied by voltage clamp experiments in ventricle cells. Two inward currents were identified as the L-type calcium current (Figure 1.4c) and the T-type calcium current (Figure 1.4d), and two outward currents as the A-type potassium current (Figure 1.4a) and delayed rectified potassium current (Figure 1.4b) (Yeoman & Benjamin, 1999; Yeoman, Brezden, & Benjamin, 1999). Some cells were found to have at least one calcium dependent potassium current, however this current was not studied (Yeoman & Benjamin, 1999). Cells possessing this potassium current were classified as type II, and cells without this current are type I. Type I cells were preferred for study to eliminate the extra complexity of this channel and easily isolate the A-type and delayed rectifier potassium currents (Yeoman & Benjamin, 1999).

The two calcium currents were isolated by using tetraethylammonium (TEA) to block the delayed rectifier potassium current and voltage ramp experiments were performed to identify

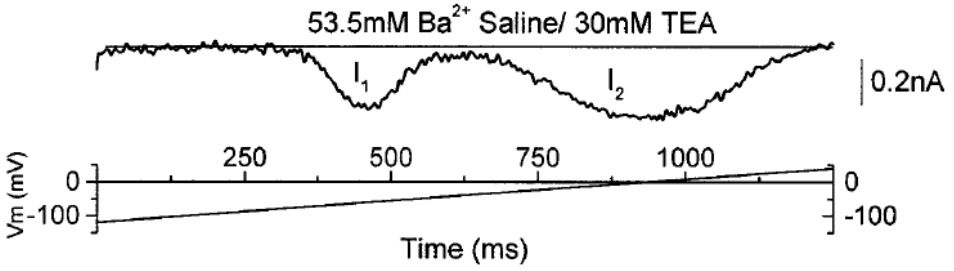

Figure 1.3: Two inward currents of *Lymnaea stagnalis* ventricle cell were identified during a voltage ramp experiment. The potassium channel blocker TEA was added to the external solution, and Ba^{2+} replaced Ca^{2+} to both increase the amplitude of the currents and prevent calcium-dependent processes such as opening Ca^{2+} activated potassium channels. One current is identified as a low voltage activated current (I_1) and the second as a high voltage activated current (I_2). (Yeoman et al., 1999)

two separate currents (Figure 1.3). One activated at a low potential (low voltage activated, LVA) and one activated at a high potential (high voltage activated, HVA) (Yeoman et al., 1999). Using barium instead of calcium in the external solution increased the amplitude of the currents to identify two individual events (Yeoman et al., 1999) (Figure 1.3). The majority of cells possess both HVA and LVA currents, however a small portion have only LVA current lacking an HVA current, or have only HVA current lacking an LVA current (Yeoman et al., 1999).

The LVA current was found to be characteristic of a T-type current. In previous studies, the majority of invertebrate muscle was found to lack a T-type current. The only other recorded T-type current found in invertebrate muscle when Yeoman et al. performed these experiments in 1999 was also from *Lymnaea stagnalis* in the vas deferens (Yeoman et al., 1999). This current was found to activate at -58 $\pm$ 1 mV and peak between -40 to -30 mV (Yeoman et al., 1999) with voltage dependent inactivation (Yeoman et al., 1999). The reversal potential with Ba^{2+} was recorded as +40 mV, however the theoretical reversal potential for a Ba^{2+} selective channel should be +175 mV. Yeoman et al. hypothesized that the T-type current may pass another type of ion such as K^+ to lower the reversal potential. The low activation threshold and voltage dependent inactivation to create a transient current upon depolarization are characteristic of T-type currents (Yeoman et al., 1999).

The HVA current was characteristic of an L-type current. The current activated at -34 ± 2 mV and peaked between -10 to 0 mV (Yeoman et al., 1999). These events occur at a much more depolarized voltage than the T-type current (Yeoman et al., 1999). When recorded in a solution containing Ca^{2+}, the current inactivates completely after peaking from a depolarizing step. When Ca^{2+} is replaced with equimolar Ba^{2+}, there is a marked reduction in inactivation suggesting calcium induced inactivation (Yeoman et al., 1999). This creates a "long lasting" current in the absence of Ca^{2+} characteristic of L-type currents. The HVA current was also found to be blocked by the drug nifedipine, a known blocker of L-type calcium channels (Yeoman et al., 1999). These electrophysiological and pharmacological characteristics of the HVA channel allowed Yeoman et al. to conclude it was an L-type calcium current. The L-type current was also characterized in *Lymnaea stagnalis* respiratory neurons where their slow activation and inactivation kinetics as well as calcium dependent inactivation resembled the properties of mammalian L-type channels (Spafford, Dunn, Smit, Syed, & Zamponi, 2006).

The two potassium currents were studied in type I cells as Ca^{2+} dependent K^+ currents were not studied in these experiments (Yeoman & Benjamin, 1999). Currents were isolated by using a known blocker and subtraction of two recordings. The A-type current was isolated by blocking the delayed rectifier current by using TEA. The delayed rectifier current was isolated by first recording voltage steps in physiological conditions, then recording voltage steps in 5 mM TEA and subtracting the two traces. Since the delayed rectifier was blocked in the trace using TEA, it is revealed as the only difference between the two recordings and can be isolated (Yeoman & Benjamin, 1999). The TEA-insensitive current activated at -45 ± 1 mV with a peak that increased with increasing depolarization followed by significant inactivation (Yeoman & Benjamin, 1999). When treated with TEA followed by the known A-type blocker 4-aminopyridine (4-AP), there was reduction in the peak of the current showing that current was blocked by 4-AP (Yeoman & Benjamin, 1999). Since the current was blocked by 4-AP, insensitive to TEA, and showed marked inactivation after depolarization it was concluded

to be an A-type potassium current (Yeoman & Benjamin, 1999).

Finally the TEA-sensitive current was characterized and concluded to be a delayed rectifier potassium current. It was found to be largely composed of potassium and activated at -27 ± 1 mV, a more depolarized potential than the A-type potassium current which is typical of delayed rectifier currents (Yeoman & Benjamin, 1999). Another characteristic feature of delayed rectifier currents was the little time dependent inactivation after the peak current (Yeoman & Benjamin, 1999). The lack of inactivation, higher activation threshold and TEA sensitivity allowed Yeoman and Benjamin to classify this current as a delayed rectifier potassium current.

During the ramp protocols performed beginning from -90 mV, there was no activity in the voltage range below activation of the T-type current, indicating no inward rectifier current or "funny" current found in vertebrate pacemaking SA node cells (Yeoman & Benjamin, 1999). The lack of inward rectifier causes the cells to have high input resistance, allowing small currents to cause a larger change in voltage since the cell is not leaky (Yeoman & Benjamin, 1999). The lack of hyperpolarized activated currents suggests that another channel must be responsible for pacemaking in these ventricle cells.

The currents found in *Lymnaea stagnalis* ventricle cells have similarities to both mammalian SA node and ventricle cells. A-type potassium currents are also found in mammalian ventricle cells and are responsible for the transient repolarization phase of the action potential (Yeoman & Benjamin, 1999). Delayed rectifier currents with high activation threshold as seen in *Lymnaea* are also characteristic of mammalian ventricle cells (Yeoman & Benjamin, 1999). The *Lymnaea* ventricle cells have more similarities to mammalian SA node cells including high input resistance, a lack of inward rectifier current, and absence of voltage gated Na^+ channels. The currents of *Lymnaea* ventricle cells were identified collectively by Yeoman, Brezden and Benjamin, but studies were not conducted on their physiological roles in the action potential.

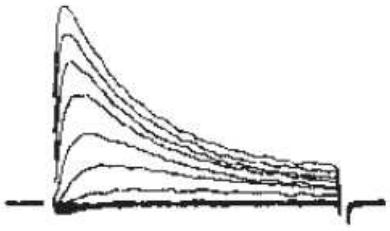

(a) Isolated A-type potassium current identified by blocking other currents and activating the current by voltage steps. The A-type current features rapid activation and inactivation of an inward potassium current. (Yeoman & Benjamin, 1999)

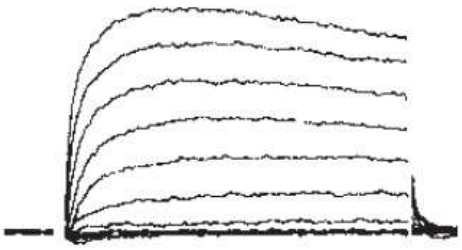

(b) Isolated delayed rectifier potassium current identified by taking voltage steps in phsyiological conditions, again in the presence of TEA which blocks the delayed rectifier current, and subtracting the two traces revealing the delayed rectifier potassium current. The current has slow activation and little to no inactivation. (Yeoman & Benjamin, 1999)

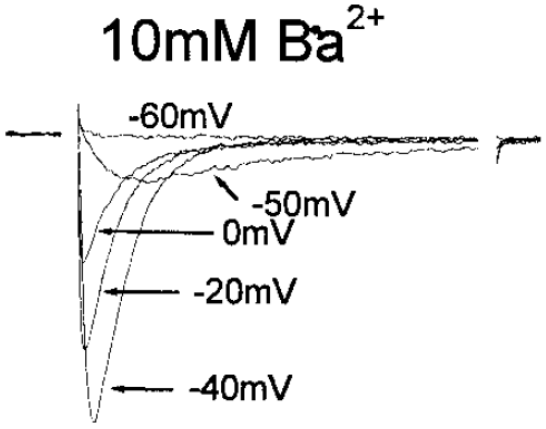

(c) Isolated T-type current during voltage steps in Ba^{2+} containing solution. The current shows rapid low voltage activation and inactivation in the presence of Ba^{2+}, typical of T-type currents. (Yeoman et al., 1999)

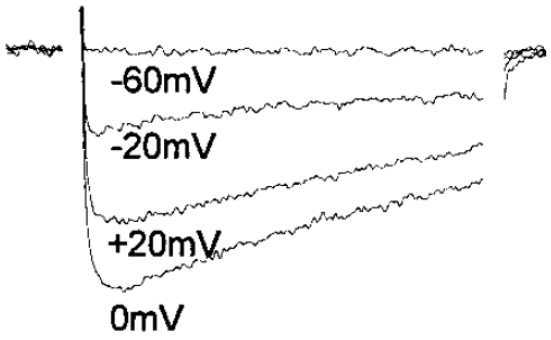

(d) Isolated L-type current during voltage steps in Ba^{2+} containing solution. The current shows high voltage activation with little inactivation when passing Ba^{2+} because of the lack of Ca^{2+} dependent inactivation, typical of L-type currents. (Yeoman et al., 1999)

Figure 1.4: Isolated inward and outward currents identified during voltage step experiments. Outward currents are (a) A-type potassium current, and (b) delayed rectifier potassium current; inward currents are (c) T-type calcium current, and (d) L-type calcium current. (Yeoman et al., 1999; Yeoman & Benjamin, 1999)

1.2.2 Action Potentials of Ventricle Cells

In 1999, Yeoman and Benjamin performed microelectrode recordings on dissociated *Lymnaea stagnalis* ventricle cells. The resting membrane potential was recorded as -55 ± 5 mV, with spontaneous action potentials occurring at a rate of 8.5 ± 1.2 spikes per minute when the membrane was hyperpolarized between -70 to -63 mV (Yeoman & Benjamin, 1999). Each ventricle cell was capable of producing two types of spikes: a spike-plateau and a fast spike action potential (Figure 1.5) (Yeoman & Benjamin, 1999). The fast-spike action potential follows the shape of a neuronal action potential with a fast rising phase and immediate repolarization (Yeoman & Benjamin, 1999). These action potentials take on a similar shape to the sinoatrial node action potential in humans, and are not associated with muscle contraction (Yeoman & Benjamin, 1999). Cells may also generate a spike-plateau action potential with the characteristic plateau elongating the action potential and allowing muscle contraction while delaying repolarization (Yeoman & Benjamin, 1999). Cells are able to generate either type of action potential, but cell tends to only fire completely sporadically or with a high degree of rhythmicity. Cells that tend to fire rhythmically do not tend to switch to a sporadic firing behaviour, and similarly sporadically firing cells do not tend to become rhythmic (Yeoman & Benjamin, 1999).

Sodium currents are necessary for cardiac action potential upstroke in vertebrate hearts. Yeoman et al., 1999 assumed sodium played no role in the ventricular action potential of invertebrates such as *Lymnaea* (Yeoman et al., 1999) because of the lack of sodium channels in ventricle cells (Senatore et al., 2014). In the absence of sodium channels, the upstroke is thought to be due solely to inward calcium currents from L-type and T-type channels (Yeoman & Benjamin, 1999). The transient LVA current begins the upstroke and upon inactivating, the HVA L-type current activates and continues the upstroke and plateau phase with its long lasting current (Yeoman *et al.*, 1999).

Yeoman *et al.* generated action potentials by a rebound spike in three different conditions: normal saline solution, with no sodium ions present, and with no calcium ions present. To

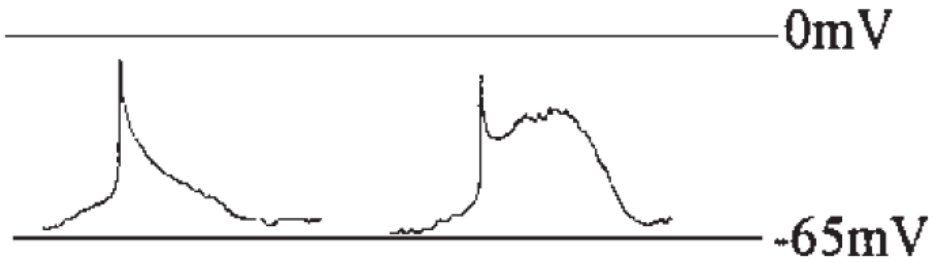

Figure 1.5: *Lymnaea stagnalis* ventricle cells are capable of producing two types of action potentials. Current clamp experiments where the membrane potential was hyperpolarized produced spontaneous electrical activity of variable shape, but two general shapes of action potentials were described. Left: Fast spike action potential features rapid upstroke and repolarization and does not have a plateau phase. Right: Spike-plateau action potential possesses the general phases of the human ventricular action potential. Rapid upstroke, transient repolarization, a plateau phase, and repolarization. (Yeoman *et al.*, 1999)

generate a rebound spike, the cell is first hyperpolarized by an applied current stimulus to remove inactivation. The hyperpolarizing stimulus is removed causing the membrane potential to increase and activate the newly deactivated currents. Spikes were generated with no sodium ions present, and appeared to have the same properties as a spike in normal saline solution. With no calcium present, there was no upstroke in recordings in zero applied current or when the cell was hyperpolarization first (Yeoman *et al.*, 1999). This led to the conclusion that calcium is the exclusive ionic carrier of the upstroke and sodium does not contribute to rhythm generation of the heart and (Yeoman *et al.*, 1999), however a contradiction to this conclusion was discovered in 2014 by Senatore et al..

1.2.3 T-Type Ca^{2+} Channel Splice Variance

The influence of sodium ions on the isolated calcium currents were not examined until 2014 by Senatore et al.. Cultured *Lymnaea stagnalis* ventricle cells were recorded both in the presence of sodium, and with the impermeant monovalent cation N-Methyl-D-glucamine (NMDG) in place of sodium (Figure 1.6). Recordings found no T-type current in the presence of NMDG and barium, and a T-type current in the presence of sodium and barium. In both cases, the L-

type current was not affected (Senatore et al., 2014). This contradicts Yeoman's conclusions regarding sodium ions having no contribution to the action potential, and suggests T-type currents are the major carrier of sodium currents.

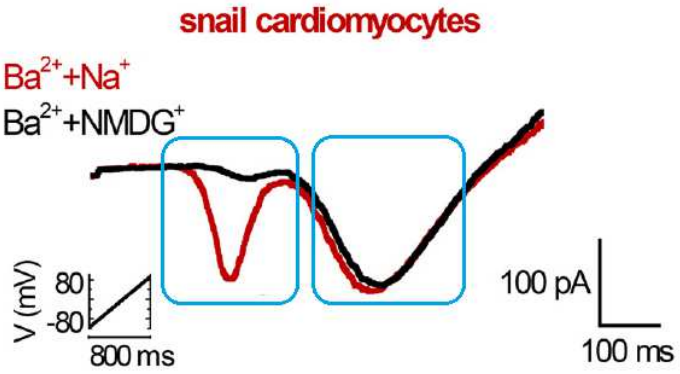

Figure 1.6: A voltage ramp was performed to isolate the T-type (left box) and L-type inward (right box) currents of a snail cardiomyocyte. When the ramp was performed in external solution containing both sodium and barium, both T-type and L-type currents are present (red curve). When sodium is removed and replaced with the impermeable monovalent ion NMDG, the T-type current is absent and the L-type current remains unchanged (black curve). (Senatore et al., 2014)

A splice variance was found in the T-type calcium channel of *Lymnaea stagnalis* LCa_V3 for exon 12 which causes a variant in ion selectivity (Senatore et al., 2014). The T-type channel isoform containing exon 12a is largely sodium permeant and calcium impermeant, while the T-type channel containing exon 12b is equally sodium and calcium permeant (Senatore et al., 2014). The 12a isoform is permeable to monovalent cations with the ion conductance decreasing as atomic radius increases, but ion conductance decreases with increasing calcium concentration suggesting calcium acts as a channel blocker (Senatore et al., 2014).

Quantitative polymerase chain reaction (qPCR) was used to determine the density of the two isoforms in different tissues of adult and juvenile snails (Figure 1.7) (Senatore et al., 2014). The 12a isoform is exclusive in the heart where the 12b isoform is absent. In secretory glands such as prostate and albumin gland, the reverse situation appears to occur where 12a is absent and the major isoform present is 12b (Senatore et al., 2014). The

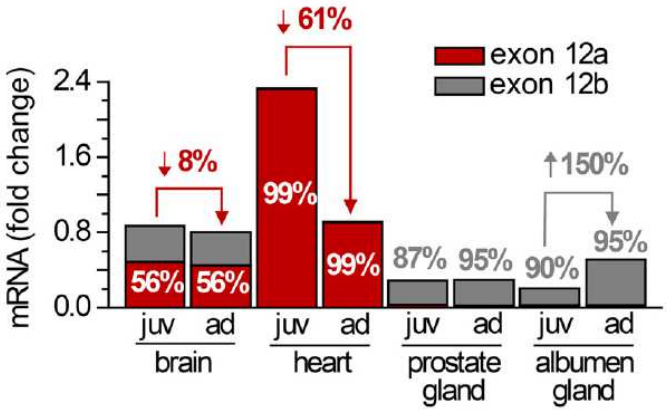

Figure 1.7: qPCR was performed on various tissues of the pond snail *Lymnaea stagnalis* to determine where 12a and 12b T-type channel isoforms are expressed. Differences in expression levels between juvenile and adult snails are also shown. The 12a isoform is found exclusively in heart with expression levels declining from juvenile to adult snails. The 12b isoform is found almost exclusively in prostate and albumen gland cells. The 12a and 12b isoform is found in equal proportions in CNS neurons. (Senatore et al., 2014)

expression pattern of these isoforms in specific tissues suggest permeability of the T-type channels plays specific roles for certain cell types. Sodium currents are likely required to act as a pacemaker for ventricle cells, where a pacemaker is not required for secretory glands such as prostate or albumen gland (Senatore et al., 2014). The permeability to sodium ions in invertebrate T-type channels suggests that these T-type channels may act in lieu of the absent sodium channels (Senatore et al., 2014).

1.3 Mathematical Modeling

Two types of mathematical models may be constructed to provide hypotheses about the behaviour of excitable cells. Models may either be developed by parameterizing quantitative data to reproduce experimental results exactly, or developed as a qualitative model to provide hypotheses of general behaviour seen in various types of action potentials and currents. To study the T-type current, a quantitative model of the current is constructed and implemented in a qualitative action potential model to describe its qualitative role in the action potential.

1.3.1 Classical Models

Goldman, Hodgkin and Katz developed the initial formalism for representing membrane permeability through their constant field theory in 1949 (Hille, 2001). The constant field theory is based on the following simplifying assumptions. The cell membrane is assumed to be homogenous with ions passing through the membrane instantaneously from the external solution (Hille, 2001). As the ions pass through the membrane, it is assumed they pass independently of one another without interaction. Finally, the name "constant field" is derived from the assumption that the electric field is constant and therefore the potential drops linearly across the membrane (Hille, 2001). These assumptions provide the Goldman-Hodgkin-Katz current equation to describe the current of ion species S across the membrane (Hille, 2001)

$$I_S = P_S z_S^2 \frac{EF^2}{RT} \frac{[S]_i - [S]_o \exp(\frac{-z_S FE}{RT})}{1 - \exp(\frac{-z_S FE}{RT})} \tag{1.1}$$

where P_S is the permeability, z_S is the valence charge, E is membrane voltage, F is Faraday's constant, R is the ideal gas constant, T is the absolute temperature, and $[S]_i$ and $[S]_o$ are the internal and external concentrations of ion S respectively.

It is commonly assumed that the number of ions that move in or out of the cell during an action potential is negligible allowing the internal and external ionic concentrations to remain constant (Hille, 2001). The potential at which the net movement of ions is zero across the membrane is termed the equilibrium, Nernst or reversal potential, E_{rev}, because it dictates the potential at which the current changes direction (Hille, 2001). The equilibrium potential of the current is derived by setting I_S to 0 and solving for E,

$$E_{rev} = \frac{RT}{zF} \ln \frac{[S]_o}{[S]_i}. \tag{1.2}$$

The constant field equation continues to be implemented in models where the ion concentrations are subject to change. This provides a nonlinear model that better describes current

when V_m is far from E_{rev} than a linear model. Changing the ion concentrations causes a shift in equilibrium potential that can be adjusted using the constant field equation without needing to constantly recalculate new values for E_{rev}.

The GHK current equation assumes ions are able to freely pass through the membrane according to their electrochemical gradient. Modeling of excitable cells expanded in 1952 with the addition of gating to current models. These additions to the currents allowed for the first models of action potentials three years later by Hodgkin and Huxley.

The groundbreaking foundation for quantitative modeling of ion currents was developed by Hodgkin and Huxley in 1952. Voltage clamp experiments were performed on the giant axon of the squid to determine changes in ion permeability to the membrane as membrane potential changed. It is important to note that their work was performed before the discovery of ion channels; all descriptions of current relate to permeability of ions to the membrane without a clear mechanism of how ions were able to cross the membrane. Their models of voltage dependent permeability that can allow or impede ion flow across the membrane translated to the gating we understand today as the physical mechanisms controlling ion channels embedded in the membrane.

Hodgkin and Huxley (1952) described the membrane as a simple RC circuit which contains a resistor (R) and capacitor (C) (Figure 1.8). Since the lipid bilayer separates ions between the extracellular space and intracellular space, it plays the role of a capacitor separating charge (Hodgkin & Huxley, 1952). Capacitance is proportional to the area of the layer separating charge and is used to describe the size of a cell. Ion flow through the membrane is controlled by embedded ion channels, allowing channels to act as resistors (Hodgkin & Huxley, 1952). The presence of the cell capacitor and resistors allows the membrane to be modeled as an RC circuit as reviewed below.

Voltage across the membrane is measured as a difference between the voltage inside and outside of the cell called the membrane potential, V_m. This potential is a result of the membrane separating charge between the inside and outside of the cell (Hodgkin & Huxley,

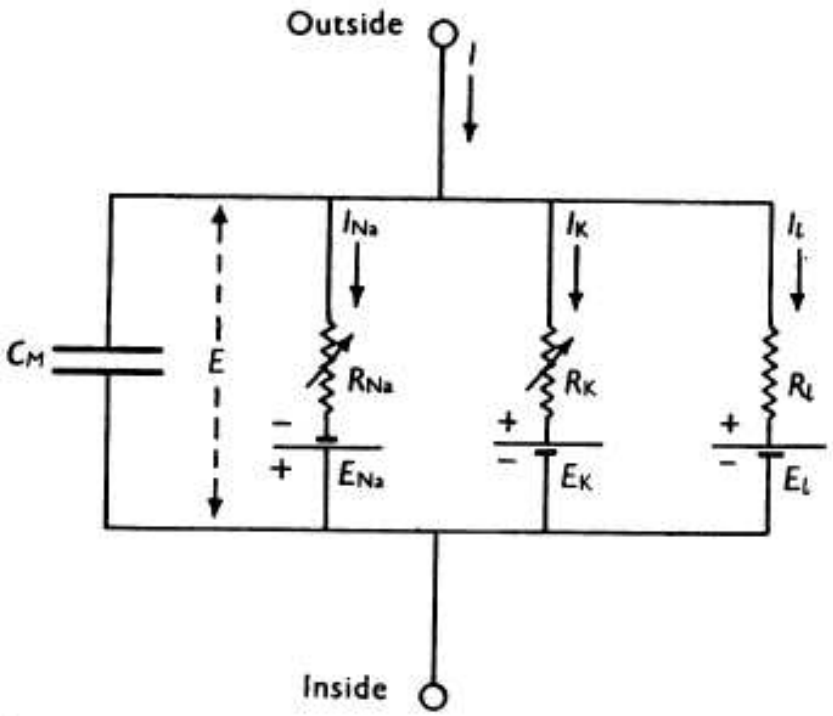

Figure 1.8: Circuit diagram of the squid giant axon. Since the membrane acts to separate charge, it acts as a capacitor with constant capacitance C_M. An extremely rapid capacitance current charges the capacitor. Ionic currents were previously described strictly in terms of ion permeability to the membrane since ion channels had not been discovered. Ionic resistance through the membrane is described as controlling the movement of ions. We now know this control is through transmembrane proteins with complex gating mechanisms controlling the pore. (Hodgkin & Huxley, 1952)

1952). This leads to a difference in ionic concentration and therefore charge between the two sides of the membrane.

Current flowing through an RC circuit is described by the following differential equation

$$C\frac{dV_m}{dt} = I \tag{1.3}$$

where C is the constant capacitance of the membrane, V_m is the membrane voltage, and I is the current flowing through the circuit. According to Ohm's Law, current may also be expressed as a ratio of voltage to resistance

$$I = \frac{V}{R} \tag{1.4}$$

however in electrophysiology, it is the common convention to discuss the ease at which current flows through the membrane instead of its resistance. The conductance, g, is the inverse of resistance

$$g = \frac{1}{R} \tag{1.5}$$

and is used instead in Ohm's law for describing current through electrically active cells

$$I = gV. \tag{1.6}$$

Equation (1.6) can be used to describe the current carried by each ionic species through each different channel where the voltage is shifted by the equilibrium potential (Hodgkin & Huxley, 1952)

$$I_{ion} = g_{ion}(V_m - E_{ion}). \tag{1.7}$$

This shifted voltage is referred to as the driving force. Driving force also dictates the direction of current. When $V_m < E_{ion}$, I_{ion} is negative and represents an inward current; when $V_m > E_{ion}$, I_{ion} is positive and represents an outward current.

The variability in modeling each different channel current is held in g_{ion}. The conductance carries the probability of gates being in an overall open state to pass current, ($p(open)$), and a maximal conductance ($\bar{g}_{ion}$) determined by the number of channels present on the membrane (Hodgkin & Huxley, 1952)

$$g_{ion} = \bar{g}_{ion} p(open). \tag{1.8}$$

The probability of the channel may be a function of voltage, time, or ligand binding. Simple gates may alter between a state that passes current (open) and a state that does not (closed) controlled by specific rates (Hodgkin & Huxley, 1952). Activation gates tend

to increase the probability of being open with increasing depolarization while inactivation gates tend to decrease the probability of being open with depolarization (Hodgkin & Huxley, 1952). The rates may be dependent on voltage or ligand concentration.

Independent voltage dependent gates are the most common gate models. These gates are assumed to alternate between states allowing or preventing current flow independent of the state of other gates (Hodgkin & Huxley, 1952). Each gate is time and voltage dependent and represented by voltage dependent rates $\alpha(V_m)$ and $\beta(V_m)$ described by the following chemical equation (Hodgkin & Huxley, 1952)

$$(Closed) \underset{\beta(V_m)}{\overset{\alpha(V_m)}{\rightleftarrows}} Open. \tag{1.9}$$

Since the gate is represented as being in either an open or closed state, the equation can be written in terms of the proportion of gates which are open, $y(t, V_m)$. It follows that the proportion of channels that are not in an open state and thus closed would be $(1 - y(t, V_m)$. Differential equations are formulated to describe $y(t, V_m)$ using mass action kinetics with the rates $\alpha(V_m)$ and $\beta(V_m)$,

$$\frac{dy(t, V_m)}{dt} = \alpha(V_m)(1 - y(t, V_m)) - \beta(V_m)y(t, V_m). \tag{1.10}$$

Rates $\alpha(V_m)$ and $\beta(V_m)$ can be expressed in terms of parameters that can be obtained from voltage clamp recordings. Steady state activation and inactivation parameters, $y_\infty(V_m)$, describe long term behaviour of the gates, and time constants, $\tau_y(V_m)$, describe the rate of current rise and decay at various membrane potentials. These parameters can be used instead to represent $\alpha(V_m)$ and $\beta(V_m)$,

$$\alpha_y(V_m) = \frac{y_\infty(V_m)}{\tau_y(V_m)} \tag{1.11}$$

$$\beta_y(V_m) = \frac{1 - y_\infty(V_m)}{\tau_y(V_m)}. \tag{1.12}$$

The model (1.10) can also be expressed using the parameters $y_\infty(V_m)$ and $\tau_y(V_m)$:

$$\frac{dy(t,V_m)}{dt} = \frac{y(t,V_m) - y_\infty(V_m)}{\tau_y(V_m)}. \tag{1.13}$$

To assemble a model to represent an action potential, each ionic current model must be incorporated into equation (1.3). The total current I through the cell is a sum of the ionic currents, I_{ion}, and an applied current I_{app}, acting as a stimulus. The net ionic current is a sum of each individual ionic current model and is taken as negative by convention of current direction. The final differential equation to determine voltage fluctuations caused by activation of each ionic current is

$$\frac{dV_m}{dt} = \frac{I_{app} - I_{ion}}{C}. \tag{1.14}$$

This voltage equation is coupled to each gating and rate equation which may create a large system of equations necessary to solve to model changes in voltage with time.

1.3.2 Cardiac Action Potential Models

The Hodgkin-Huxley models of the ionic currents of the squid axon set the foundation for modeling currents in various excitable cells. Such models are considered first generation cardiac action potential models as they contain relatively few details (Moreno & Clancy, 2011). Currents were modeled using Hodgkin-Huxley equations featuring limited gating variables and lacking details of pumps and exchangers. The development of more detailed models began the transition into the second generation of cardiac action potential models (Moreno & Clancy, 2011).

The second generation of cardiac models became much more detailed recognizing the differences in both cells and species (Moreno & Clancy, 2011). Models became cell specific by representing the cell's specific system of currents and reflecting its own action potential

shape (Moreno & Clancy, 2011). Dynamic ionic concentrations were introduced to include changing calcium concentrations caused by sarcoplasmic reticulum uptake and release dynamics (Moreno & Clancy, 2011). Second generation models continue to expand to include further details of the cell as discoveries continue to be made.

In 2003, Matsuoka, Sarai, Kuratomi, Ono, & Noma, 2003 developed a second generation model for cardiac action potentials of guinea pig ventricle and sinoatrial node cells. The Kyoto model features the fine details of the cardiac action potential including the inward and outward currents for upstroke and repolarization, background currents allowing a steady leakage of ions, ion exchangers and pumps, and sarcoplasmic reticulum dynamics (Matsuoka et al., 2003). The same core Kyoto model is used for both the ventricle and SA node models with some defining differences in currents used between the two models. Some currents such as the hyperpolarized activated current, are only represented in the SA node, while the transient outward current responsible for the transient repolarization phase of the ventricular action potential is unique to the ventricle model (Matsuoka et al., 2003).

The Kyoto model uses aspects of qualitative and quantitative modeling. The original rates of the current models were taken directly from the literature which were obtained quantitatively through fitting data (Matsuoka et al., 2003). The rates implemented in the Kyoto model are adjusted to provide meaningful simulations at unphysiological voltage levels. Voltage dependent rates were fit to the general equation

$$k = \frac{1}{A \exp \frac{V_m}{B} + C \exp \frac{V_m}{D}} \tag{1.15}$$

where constants A, B, C, and D are chosen such that the rates provide the same results at physiological voltages but do not interfere with integration of the model at extreme voltages. Instead, these rates cause saturation at large and unphysiological values of V_m (Matsuoka et al., 2003).

The current models implemented in the Kyoto model include aspects of both the Hodgkin-Huxley model and the GHK current equation. Ion concentrations of the model are dynamic

which would cause a change in reversal potential as ionic concentrations change. The model is built to reflect these changes instead of using a static reversal potential. Gating is contained inside a function defining the probability of the channel being open. This function may have various dependencies such as time, voltage, and calcium and varies between each current model. The general equation used to represent each current model in the reduced Kyoto model is as follows

$$I = P \cdot CF \cdot p(open) \tag{1.16}$$

where $p(open)$ is unitless representing the fraction of channels available to pass current, CF is the constant field equation carrying units of mM, and P is the convert factor similar to permeability carrying units of $\frac{nA}{mM}$. This model is built from the GHK current equation (Equation 1.1) with the addition of gating kinetics. The constant field equation and convert factor are equivalent to the GHK current equation. The constant field equation carries units of mM by removing a factor of Faraday's constant, permeability and valence charge,

$$CF = \frac{zFV_m}{RT} \frac{[X]_i - [X]_o \exp(\frac{-zFV_m}{RT})}{1 - \exp(\frac{-zFV_m}{RT})} \tag{1.17}$$

which is then carried by the convert factor for units of $\frac{nA}{mM}$,

$$P = zFP_S. \tag{1.18}$$

In the Kyoto model, P is constant and analogous to maximal conductance by providing an upper bound on the peak current.

The many details included in the Kyoto model are not necessary in representing the simpler invertebrate heart, therefore only a select few current models are discussed and presented in a reduced form of the Kyoto model. These currents include the L-type calcium current, rapid delayed rectifier current, and transient outward (A-type) current.

1.4 Objectives and Hypotheses

The objective of the study was to examine both the role of T-type currents in a simple invertebrate action potential and contrast the physiological differences between the 12a and 12b isoforms found in *Lymnaea stagnalis*. Identification of currents present in ventricle cells and characterization of the 12a and 12b T-type isoforms led to the following hypotheses for this study:

- The T-type current is hypothesized to be a major pacemaker in *Lymnaea stagnalis* ventricle cells. Its low voltage activation and window current suggest it is responsible for spontaneous electrical activity in the cell by providing a leak current responsible for slowly depolarizing the cell to threshold. Changes to sodium concentration in experiment and simulation are expected to alter pacemaking rate and ability.

- Action potentials of the prostate and albumen cells will be slower than those seen in ventricle cells. Prostate and albumen cells are secretory cells and thus are expected to feature long waves of depolarization to allow a surge of calcium into the cell for secretion. The 12b current is expected to carry calcium as well as sodium to begin a calcium signaling process necessary for secretion.

- The 12a T-type current may be responsible for upstroke of the cardiac action potential acting in lieu of the absent sodium channels. Previous studies in zero sodium showed spiking capabilities only with a rebound spike, suggesting the sodium dependent current may be responsible for spike generation.

The hypotheses were to be tested using two approaches. Electrophysiological experiments were to be performed on ventricle, prostate and albumen cells. Details can be found in Appendix B. Numerical simulations were run on a mathematical model built by reverse engineering a qualitative representation of the ventricular action potential. Experiments were to be performed on each cell type to provide recordings of action potentials in physiological conditions and variations on ionic concentration to compare the shape of the spikes generated

in each condition. The simulations run mimicked the conditions of the experiments to provide predictions of current behaviour and ultimately their physiological roles.

2 Numerical Modeling

A numerical model was constructed in MATLAB to represent the action potentials recorded in *Lymnaea stagnalis*. The model contained the four currents described by Yeoman and Benjamin (1999) and Yeoman *et al* 1999 in type I *Lymnaea* ventricle cells. Currents implemented in the model were taken from the Kyoto model, modified from the Kyoto model, or fitted from current recording data. The A-type potassium current is represented as the transient outward current taken unaltered from the Kyoto model. The delayed rectifier current is represented by the rapid delayed rectifier current of the Kyoto model. The Kyoto model features both rapid and slow delayed rectifier currents, however the rapid delayed rectifier current was chosen because the slow delayed rectifier current contained a calcium ion dependence, and the delayed rectifier current of *Lymnaea stagnalis* was not shown to contain a calcium dependence (Yeoman & Benjamin, 1999). The L-type current model was taken from the Kyoto model with some modifications. Rates were adjusted to produce similar results to voltage ramp experiments performed on dissociated *Lymnaea stagnalis* ventricle cells of Senatore et al., 2014. The T-type current was created using parameter fittings performed by Senatore et al., and activation time constant fittings were performed for this thesis.

The *Lymnaea* cardiac action potential model follows the Hodgkin-Huxley model. Voltage is determined by the RC circuit equation

$$\frac{dV}{dt} = \frac{I_{app} - I_{ion}}{C_m} \tag{2.1}$$

where I_{app} is the amplitude of the applied current to the model cell and I_{ion} is the sum of the ionic currents present. I_{ion} is the sum of T-type, L-type, delayed rectifier, and transient outward (A-type) currents

$$I_{ion} = I_{CaT} + I_{CaL} + I_{Kr} + I_{to}. \tag{2.2}$$

Details for each ionic current model are discussed in the following sections.

2.1 LCa$_v$3-12a and LCa$_v$3-12b Current Models

Numerical current models for the two *Lymnaea* T-type channel isoforms LCa$_v$3-12a and LCa$_v$3-12b were assembled using recordings from Dr. Adriano Senatore of the Spafford lab. Both current models are constructed following the same structure as Equation (1.16).

The 12a current model, $I_{CaT-12a}$, is carried almost exclusively by sodium ions (Senatore et al., 2014) and is modeled as a sodium current, $I_{CaT-12a}Na$,

$$I_{CaT-12a} = I_{CaT-12a}Na \tag{2.3}$$

$$I_{CaT-12a} = P_{CaT-12a} \cdot CF_{Na} \cdot y_{1,12a} \cdot y_{2,12a}. \tag{2.4}$$

$P_{CaT-12a}$ is the 12a convert factor, CF_{Na} is the constant field equation for sodium, $y_{1,12a}$ is the activation gate and $y_{2,12a}$ is the inactivation gate. Each gate is solved by the different equation (1.13) using steady state parameters $y_{1,12a,\infty}(V_m)$ and $y_{2,12a,\infty}(V_m)$, and the inactivation time constant parameter $\tau_{y_{2,12a}}(V_m)$ previously determined by Dr. Adriano Senatore. Activation time constants $\tau_{y_{1,12a}}(V_m)$ were fit for this thesis and are further described in the following section.

The 12b current model, $I_{CaT-12b}$, equally carries both sodium and calcium ions. The total current is separated as the sum of a sodium, $I_{CaT-12b}Na$, and calcium, $I_{CaT-12b}Ca$ current with identical gates and half of the total convert factor, $P_{CaT-12b}$,

$$I_{CaT-12b} = I_{CaT-12b}Na + I_{CaT-12b}Ca \tag{2.5}$$

$$I_{CaT-12b}Na = 0.5P_{CaT-12b} \cdot CF_{Na} \cdot y_{1,12b} \cdot y_{2,12b} \tag{2.6}$$

$$I_{CaT-12b}Ca = 0.5P_{CaT-12b} \cdot CF_{Ca} \cdot y_{1,12b} \cdot y_{2,12b}. \tag{2.7}$$

$$\tag{2.8}$$

Gates $y_{1,12b}$ and $y_{2,12b}$ are also solved by equation (1.13). Parameters for steady states and inactivation time constants were also previously determined by Dr. Adriano Senatore. The activation time constants were fit for this thesis and described in the following section.

2.1.1 Parameterizing LCa_v3-12a and LCa_v3-12b

Parameters for steady state inactivation, steady state activation and the voltage dependent time constants of inactivation and activation were taken from the electrophysiology recordings performed by Dr. Adriano Senatore of the Spafford lab. Some parameters had been previously fit and were taken from Senatore et al., 2014 or Dr. Senatore's data analysis files. Senatore et al., 2014 provided parameters for modeling steady state activation and inactivation and Dr. Senatore's data analysis provided fittings for time constants of inactivation. Time constants of activation were not available, thus fittings were carried out in order to build the current model.

Voltage dependent time constant parameters are taken from voltage step protocols. During a voltage step, the cell is hyperpolarized at a holding potential then instantaneously depolarized to invoke a current. The duration of the step depends on the current of interest and must be long enough such that it is able to inactivate. From this data, current-voltage curves may be generated based on the size of currents activated at specific voltage steps, and time constants describing speed of activation and inactivation may be fit.

The current evoked from an instantaneous voltage step has two components (Figure 2.1): an exponential rise in amplitude (Figure 2.1 blue box) followed by an exponential decay (Figure 2.1 black box). Time constants of activation describe the rate of exponential growth of the first phase, and time constants of inactivation describe the rate of exponential growth during the second phase. Data points of either phase of the current are fit to the general equation

$$I = a \exp\left(\frac{-t}{\tau}\right) + b \tag{2.9}$$

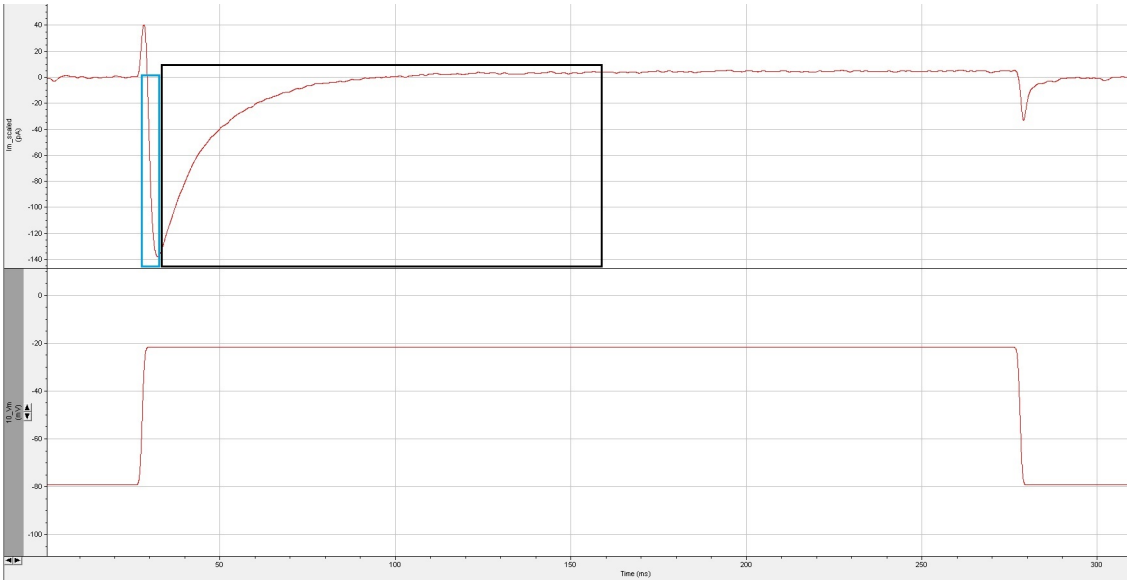

Figure 2.1: Sample voltage step trace from a whole cell recording of LCa$_v$3-12a expressed in HEK 239T cell performed by Adriano Senatore displayed with Clampfit software (pClamp 10, Molecular Devices). The top trace shows the current evoked by the voltage stimulus waveform at the bottom. Voltage dependent time constants are fit from these current traces. An exponential curve is fit in the blue box for activation time constants and inactivation time constants are fit for curves in the black box at each voltage step.

such that in either activation or inactivation, the time constant is given as τ. The signs of a and τ can be used to determine the proper curve is being fit. The shape of the curve must be consistent for proper parameterization. For activation, a and τ must be positive to give the proper shape. Constants a and b of the fittings are not recorded as they are not necessary for modeling.

Time constants for activation and inactivation are voltage dependent and yield a separate τ for each voltage step. The τ values collected for each voltage step are averaged (inactivation time constant values were previously averaged by Dr. Senatore) and plotted on a voltage vs τ curve (Figure 2.2). Points were fit to a single exponential curve

$$\tau(V_m) = a \exp \frac{V_m}{b} + c \tag{2.10}$$

to be implemented in the gating equations. Results of the averaged time constants of activation and curve fittings are displayed in Figure 2.2. The voltage dependent activation time

constant equations for the 12a and 12b models are

$$\tau_{y_{1,12a}} = 0.1194 \exp\left(\frac{-V_m}{15.2577}\right) + 0.3453 \tag{2.11}$$

$$\tau_{y_{1,12b}} = 0.8162 \exp\left(\frac{-V_m}{31.3185}\right) + 0.3865 \tag{2.12}$$

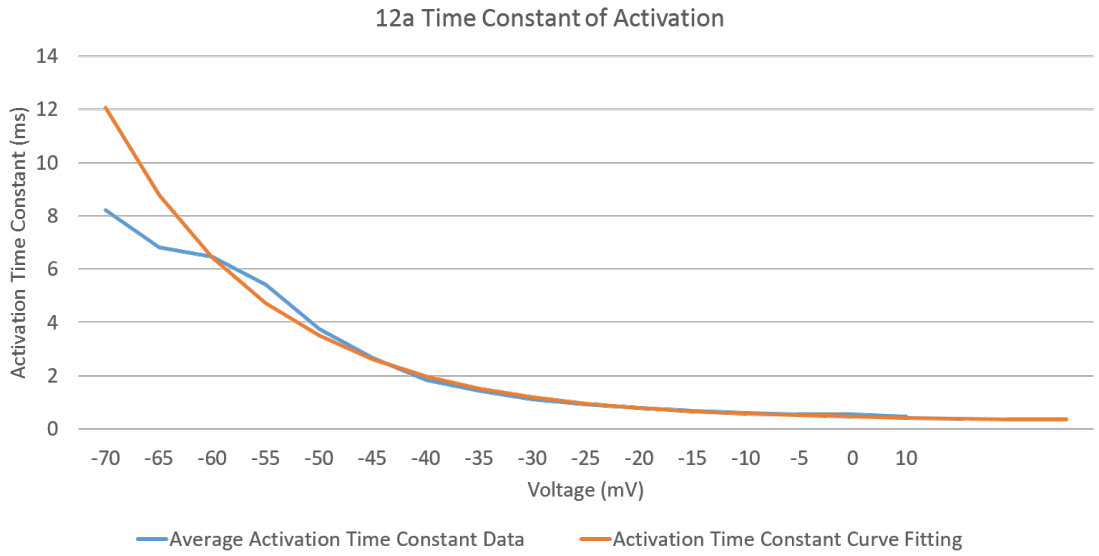

Figure 2.2: Averages for activation time constants for LCa_v3-12a and curve fitting for activation time constant.

Voltage dependent inactivation time constants were fit by Dr. Adriano Senatore to similar curves as shown in the black box of Figure 2.1. Inactivation time constants were fit the portion of the current curve between its peak amplitude and return to zero with equation (2.9) to gather each τ value for the voltage step. For this thesis, the set of inactivation time constants gathered by Dr. Senatore were plotted against voltage and fit to equation 2.10 to create a voltage dependent inactivation time constant function for the 12a and 12b current models. Details are found in appendix A.6.

Steady state inactivation values were fit by Dr. Adriano Senatore from a specific protocol (Figure 2.3). First, a series of increasing voltage steps were performed to determine approximately which potential invoked the largest current. This peak current was used to

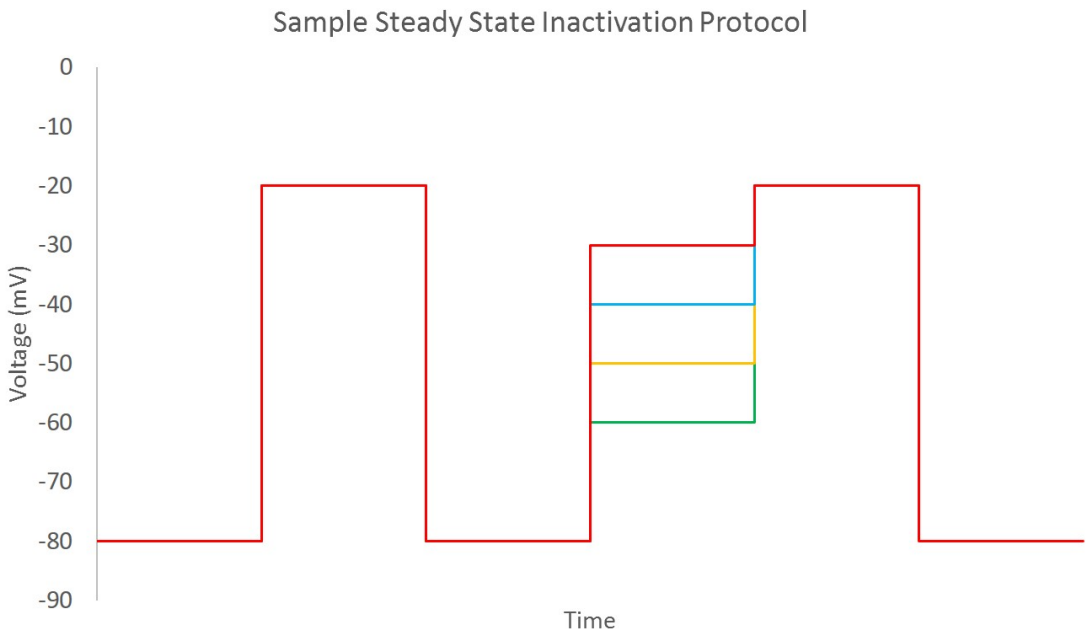

Figure 2.3: Sample steady state inactivation protocol. The coloured steps indicate the various levels of each prepulse used to inactivation a portion of the channels.

determine the steady state inactivation value at each voltage level. The steady state inactivation protocol consists of three voltage steps. The voltage is held at a hyperpolarized holding potential until the voltage is stepped up briefly to the predetermined potential evoking the largest amplitude current and returned to its holding potential. The cell is maintained at this holding potential until the channels recover from inactivation. The final two voltage steps consist of an inactivating prepulse followed by a voltage step. The prepulse is a short voltage step which evokes a small current and allows a portion of the channels to inactivate. Immediately after the prepulse, the voltage is stepped up to the peak potential as in the first voltage step. The prepulse is the only voltage step which increases in potential with each run of the protocol. Since the prepulse causes inactivation of a portion of channels, the current peaks of the first and third voltage steps will vary. Steady state inactivation data was provided following this protocol by recording I/I_{max} ratios of the two current peaks for each voltage step of the prepulse. The I/I_{max} steady state inactivation values versus voltage plots provide a sigmoid shaped curve which was fit to the Boltzmann equation

$$y_\infty = \frac{1}{1 + \exp\left(\frac{V_{\frac{1}{2}} - V_m}{k}\right)} \tag{2.13}$$

to determine parameters $V_{\frac{1}{2}}$ and k. $V_{\frac{1}{2}}$ is the voltage at which half of the channels have been inactivated, and k is the slope of the sigmoid. Values for $V_{\frac{1}{2}}$ and k are taken from Senatore et al., 2014 for the 12a and 12b steady state inactivation functions found in appendix A.6.

Steady state activation was fit by Dr. Adriano Senatore from voltage step protocols also used for activation time constants. First, the reversal potential was determined for the current. Next, each current peak at its respective voltage step was used to calculate its conductance from the equation

$$g = \frac{I}{V - E}. \tag{2.14}$$

The highest conductance of the data set for the voltage steps was set as g_{max} and ratios of g/g_{max} were calculated at each voltage. The steady state activation plot of g/g_{max} versus voltage also has a sigmoid shape and is fit to equation (2.13) giving the parameters $V_{\frac{1}{2}}$ and k found in Senatore et al., 2014. Details of the equations are found in appendix A.6.

2.2 Transient Outward Current Model

The transient outward current model of the Kyoto model was created by Dumaine et al., 1999 as a model to study Brugada syndrome in a modified version of the Luo-Rudy model of the cardiac action potential. The model originally featured a maximal conductance three activation gates, an inactivation gate, and a voltage dependent outward rectifier factor (Dumaine et al., 1999). A modified form of this equation was implemented in the Kyoto model (Matsuoka et al., 2003). The outward rectifier factor was removed and the rates were adjusted to fit Equation 1.15. The constant field equation (Equation 1.17) was used instead of the driving force (Matsuoka et al., 2003).

As this fast outward potassium current of the Kyoto model resembles the A-type potas-

sium current described by Yeoman & Benjamin, 1999 it was chosen in our cardiac model to play this role. For the model, the transient outward current was modified further. Both sodium and potassium currents were modeled to contribute to I_{to} in the Kyoto model, however the sodium current contributes to less than 10% of the current and hence it was omitted. Thus the transient outward potassium current is represented in our model as

$$I_{to} = P_{to} \cdot CF_K \cdot y_1^3 \cdot y_2$$

with equations describing the activation gate y_1 and inactivation gate y_2 in the form of Equation 1.10 with voltage dependent rates as given in appendix A.3.

2.3 Delayed Rectifier Current Model

The delayed rectifier potassium current used in the Kyoto model was taken from Ono & Ito, 1995. Ono & Ito, 1995 developed the model by parameterizing voltage steps performed on rabbit sinoatrial node cells in presence of the blocker E-4031 to isolate the delayed rectifier current. Driving force and conductance are used instead of the constant field equation, and gating consists of two activation and one inactivation gate. Activation consists of two components, a fast gate and a slow gate(Ono & Ito, 1995). Each component was associated with a contributing factor to the total activation such that 60% of the activation was due to the fast component and 40% due to the slow component (Ono & Ito, 1995).

The delayed rectifier current model implemented in the Kyoto model was slightly adjusted from what Ono and Ito developed in 1995. The gates are referred to as y_1, y_2 and y_3 for the fast activation, slow activation, and inactivation gates respectively. The maximal conductance is expressed as a function of external potassium. This dependence has not been examined in detail (Matsuoka et al., 2003), but was adjusted by running simulations

of $[K]_o$-voltage relations in the SA node (Matsuoka et al., 2003). Both voltage dependent activation rates for $\beta(V_m)$ of gates y_1 and y_2 take on a slightly modified form of Equation 1.15,

$$k(V_m) = \frac{1}{A \exp \frac{V_m}{B} + C \exp \frac{V_m}{D}} + \frac{1}{E \exp \frac{V_m}{F}} \tag{2.15}$$

such that A, B, C, D, E and F are constants (Matsuoka et al., 2003). All other voltage dependent rates of the delayed rectifier current model follow Equation 1.15 (Matsuoka et al., 2003).

The delayed rectifier current model implemented in our model was further adjusted to the form of Equation 1.16,

$$I_{Kr} = P_{Kr} \cdot CF_K \cdot (0.6y_1 + 0.4y_2) \cdot y_3. \tag{2.16}$$

A convert factor P_{Kr} and constant field equation for potassium, CF_K, were used instead of an equilibrium potential and maximal conductance. Each gate is represented by equation 1.10. See appendix A.4 for details.

2.4 L-Type Calcium Current Model

The L-type current in the Kyoto model is the sum of the currents from the three ionic species sodium, potassium, and calcium (Matsuoka et al., 2003),

$$I_{CaL} = P_{CaL}(CF_{Ca} + P_{Na}CF_{Na} + P_K CF_K)p(open). \tag{2.17}$$

where P_{CaL} is the L-type convert factor and $p(open)$ depends on the state of the various gates below. The permeability for the sodium and potassium equations are represented by a fraction of calcium permeability ($P_{Na} = 0.00185\%$ and $P_K = 0.0365\%$ respectively) (Matsuoka et al., 2003), making the sodium and potassium contributions essentially negligible to the

net L-type current.

The L-type calcium current model contains a complex model for $p(open)$. It features three gates: a voltage dependent gate, a calcium dependent gate, and an ultra slow gate (Matsuoka et al., 2003). The voltage dependent gate features an activation and inactivation gate where at rest, the majority of activation gates are closed and inactivation gates are open (Shirokov, Levis, Shirokova, & Rios, 1993). The calcium dependent gate is responsible for calcium induced inactivation. As local calcium concentration near the channel increases, calcium begins to bind to this gate and stabilize a closed state (Shirokov et al., 1993). The ultra slow gate is responsible for inactivation after the inactivation gates from the voltage dependent gate and calcium dependent gate close the channel (Boyett, Honjo, Harrison, Zang, & Kirby, 1994).

The voltage dependent gate and calcium dependent gate models in the Kyoto model are as described by Shirokov et al., 1993 (Figure 2.4). Shirokov's formulation of this model consisted of 16 states (four states from the voltage gate and four states from the calcium gate) with 64 rate constants (Shirokov et al., 1993), but in the Kyoto model the two gates are calculated independently with four states and eight rate constants for each gate to simplify the model (Matsuoka et al., 2003).

The voltage dependent gate consists of two coupled gates (Shirokov et al., 1993). The activation gate (Figure 2.4, see 1) inside the pore shifts between an active (A) and resting (R) state (Shirokov et al., 1993). The inactivation gate (Figure 2.4, see 2) is a magnesium ion that blocks the pore and prevents current from passing (Shirokov et al., 1993). When the pore is blocked, the channel is in an inactivated (I) state, otherwise it is in a primed (P) state. In order to pass ions, the activation gate must be active and the inactivation gate must be primed (Shirokov et al., 1993). The activation gate is much faster than the inactivation gate to give the characteristic long lasting L-type current (Shirokov et al., 1993).

Since the activation and inactivation gates are coupled, only one gate may change state at a time (Shirokov et al., 1993). Figure 2.5 represents this mechanism with eight voltage

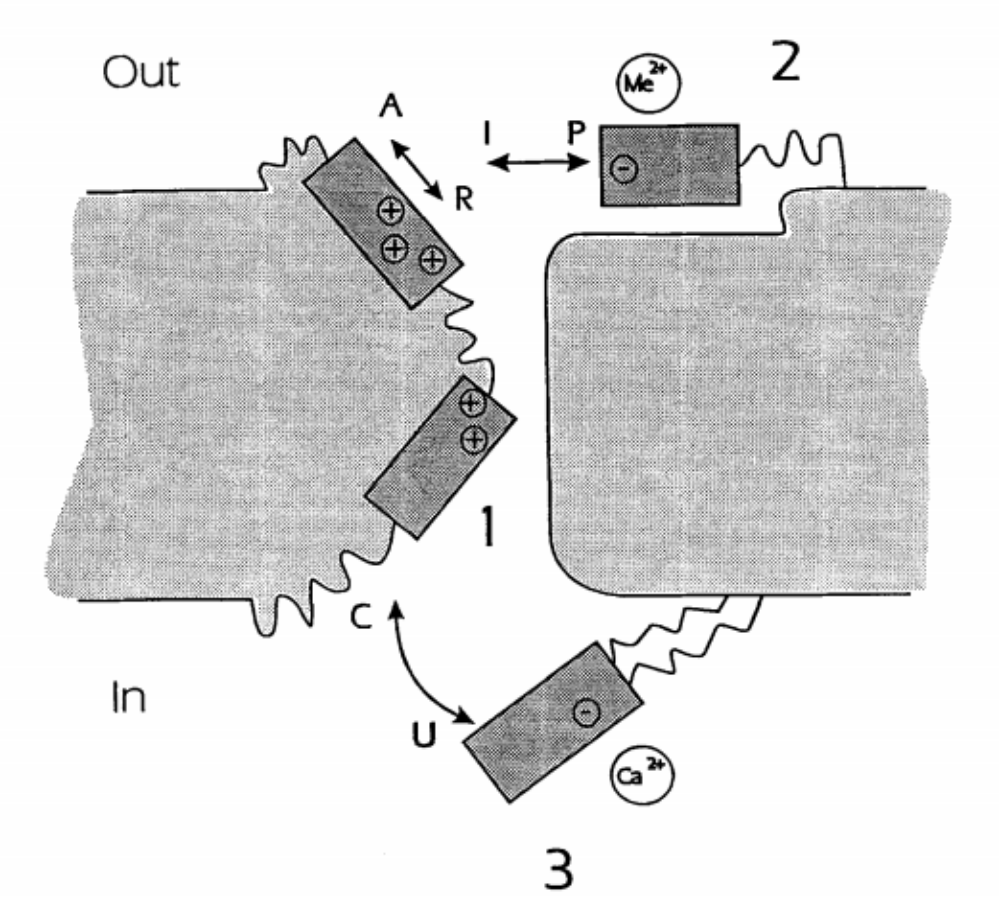

Figure 2.4: Voltage gates and Calcium gate of L-type Channel first described by Shirokov et al. (ultra slow gate not included in this model). 1: Voltage dependent activation gate which transitions between an active (A) state and resting (R) state. The active state is required to pass current. 2: Voltage dependent inactivation gate consisting of a particle that blocks the pore. The gate transitions between a primed (P) state and inactivate (I) state. A primed state is required to pass current. 3: Calcium dependent gate on the intracellular side of the cell. The gate transitions between a covered (C) state and uncovered (U) state. Calcium may bind to this gate to transition to a calcium bound and covered state (CCa) or calcium bound and uncovered state (UCa). When calcium is bound to the gate, it is more likely to be in a CCa state which blocks the pore and causes calcium induced inactivation. (Shirokov et al., 1993)

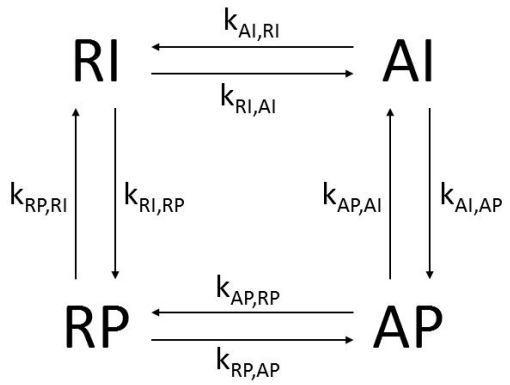

Figure 2.5: Mechanism for states of voltage-dependent gates of the L-type calcium current model. The coupled gates are represented by two letters. The left letter indicates the state of the activation gate (R or A). The right letter indicates the state of the inactivation gate (I or P). Since the gates are coupled, only one gate may change state at a time as indicated by the appropriate rate constant. See appendix A.5 for more detail. (Shirokov et al., 1993)

dependent rates to describe these transitions. The rates are described in the appendix A.5. Six of the rates are voltage dependent, however the two rates between states AP and AI are constants (Matsuoka et al., 2003). Three differential equations describe the dynamics of AI, AP and RP, and one algebraic equation describes RI. The variables AI, AP, RP, RI represent the probability of the gate being in a particular state (Matsuoka et al., 2003).

$$\frac{dAP}{dt} = k_{AI,AP}AI + k_{RP,AP}RP - (k_{AP,AI} + k_{AP,RP})AP \tag{2.18}$$

$$\frac{dAI}{dt} = k_{AP,AI}AP + k_{RI,AI}RI - (k_{AI,AP} + k_{AI,RI})AI \tag{2.19}$$

$$\frac{dRP}{dt} = k_{AP,RP}AP + k_{RI,RP}RI - (k_{RP,AP} + k_{RP,RI})RP \tag{2.20}$$

$$RI = 1 - AP - AI - RP \tag{2.21}$$

The L-type calcium channel also has a calcium dependent gate responsible for calcium induced inactivation (Figure 2.6). This gate does not depend on voltage as the voltage dependent and ultra slow gates do, but instead on intracellular calcium concentration (Shirokov et al., 1993). The gate is either in a covered (C) or uncovered (U) state. Each of these states

may also occur with calcium bound to the gate, giving CCa (covered with calcium bound) and UCa (uncovered with calcium bound) (Shirokov et al., 1993). The two rate constants between C and U are given as constants, and transitioning to a calcium bound state relies on the local concentration of calcium through a single channel current (Shirokov et al., 1993). Increasing calcium increases the probability of being in a calcium bound state and changes the dynamics of the system. Calcium binding to the gate increases the stability of the covered state, thus increasing the probability of the channel being closed causing calcium induced inactivation (Shirokov et al., 1993).

When the voltage dependent gate is in an active and primed state and the calcium dependent gate is uncovered, calcium is able to enter the cell. This increase in local calcium through the channel will affect the transition between a calcium bound and unbound state (Shirokov et al., 1993). To account for this, the transition rate between the uncovered state (U) and calcium bound uncovered state (UCa) is dependent on the probability of the channel being in an AP and U state and the local concentrations of internal calcium, $[Ca^{2+}]_{cm}$ and steady state internal calcium, $[Ca^{2+}]_i$ (Matsuoka et al., 2003) (Equation 2.22); and the transition from covered state (C) to calcium bound and covered (CCa) is dependent on local concentration of internal calcium, the probability of the active and primed (AP) state, and the probability of the covered state (Matsuoka et al., 2003).

$$rate_{U-UCa} = k_{U,UCa}(([Ca^{2+}]_{cm} \cdot p(AP) + [Ca^{2+}]_i(1 - p(AP))) \cdot p(U) \tag{2.22}$$

$$rate_{C-CCa} = k_{C,CCa}([Ca^{2+}]_{cm} \cdot p(AP))p(C) \tag{2.23}$$

The ultraslow gate is modelled as a voltage dependent gate that prevents fast recovery of inactivation and maintains the physiological heart rate frequency (Boyett et al., 1994). This gate was identified as separate from calcium dependent inactivation by performing voltage clamp recordings with barium replacing calcium in the external solution, and calcium buffers

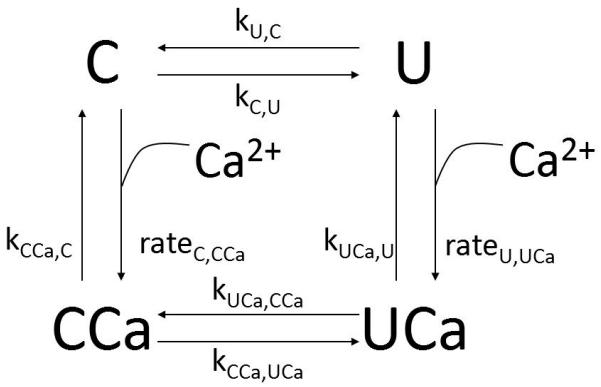

Figure 2.6: Mechanism for calcium dependent gate responsible for calcium induced inactivation of the L-type current. The gate transitions between a covered (C) and uncovered (U) state, where U allows current to pass through the channel. Calcium inside the cell may bind to the gate and transition the gate to a calcium bound and covered state (CCa) or calcium bound and uncovered state (UCa). With calcium bound to the gate, the covered state is more stable which closes the channel and inactivates the current. (Shirokov et al., 1993)

removing free calcium released by internal stores in the cell (Boyett et al., 1994). The additional inactivation gate was found to exhibit much slower kinetics than the voltage dependent inactivation gate described by Shirokov et al.. The ultraslow gate was modeled using equations 1.11 and 1.10 (Boyett et al., 1994).

The ultraslow gate of the L-type current in the Kyoto model is associated with ATP levels. This dependence is drawn from experiments done by Noma & Shibasaki, 1985. Different concentrations of ATP were added to a pipette during whole cell recordings of guinea pig ventricular cells, and a single "calcium current" is described (Noma & Shibasaki, 1985). This work was published three years before Hagiwara *et al.* discovered the presence of a T-type calcium current in addition to the well known L-type current in ventricular cells. Noma & Shibasaki, 1985 concluded that increasing levels of ATP increased the peak of the "calcium current." However many processes in the cell are ATP-dependent that could contribute to an inward current such as ion pumps and exchangers, and the paper lacks evidence that ATP is acting directly on the L-type calcium channels.

In the Kyoto model, the probability of being open depends on the state of the gates described by Shirokov et al., 1993 and Boyett et al., 1994 with an included ATP dependence

described by Noma & Shibasaki, 1985,

$$p(open) = p(AP) \cdot (p(U) + p(UCa)) \cdot \frac{y}{1 + \left(\frac{1.4}{[ATP]}\right)^3}. \tag{2.24}$$

where $p(AP)$, $p(U)$, $p(UCa)$, and y are the probability of gates being in states active and primed, uncovered or calcium bound and uncovered, and of the ultraslow gate being open, respectively.

To make the model better represent the *Lymnaea* action potential, a number of adjustments were made. The L-type current was reduced to an exclusive calcium current. The small sodium and potassium currents relative to the calcium carried current was assumed negligible and omitted in our model. Thus the L-type current is given by

$$I_{CaL} = P_{CaL} C F_{Ca} p(open). \tag{2.25}$$

In addition, since the ATP dependence is not shown to be directly related to the L-type current, it was omitted changing $p(open)$ to

$$p(open) = p(AP) \cdot (p(U) + p(UCa)) \cdot y. \tag{2.26}$$

Further, the rates associated with the L-type calcium current model were adjusted such that the voltage ramp experiment performed on cardiomyocytes described in Senatore et al., 2014 could be recreated. The voltage dependent gate rates were adjusted such that the current peaked at -10 mV and faster kinetics allowed the double hump shape in Senatore et al., 2014 Figure 6F (Figure 1.6) such that the T-type and L-type currents did not overlap during a simulated voltage ramp. Adjusted rates are found in appendix A.5.

Finally, the rates between the calcium bound covered and uncovered states ($k_{UCa,CCa}$ and $k_{CCa,UCa}$) were altered to extend the duration of the plateau phase. $k_{UCa,CCa}$ was decreased by a factor of δ by choosing $0 < \delta < 1$, and $k_{CCa,UCa}$ was increased by a factor of ϵ by choosing $\epsilon > 1$. Slowing the rate of transition from uncovered to covered was done to slow

the rate of inactivation, and speeding the transition of covered to uncovered helped recover more channels from inactivation; both changes in these factors act to prolong the duration of the time the L-type current after a spike, thus prolonging the duration of the plateau phase. However, even with these adjustments the action potentials were shorter than described by Yeoman and Benjamin, 1999.

A second version of the L-type current which has no calcium dependent inactivation (CDI) was used in the action potential model in order to prolong the plateau phase of the simulated action potential to 2-4 seconds as described by Yeoman & Benjamin, 1999. To construct the CDI-free model, $p(open)$ was altered by removing the calcium dependent gate states U and UCa reducing $p(open)$ to

$$p(open) = p(AP) \cdot y. \tag{2.27}$$

2.5 Calcium Model

The final differential equation in the system represents local calcium concentration close to the cell membrane, $[Ca]$. Experiments have not been performed to determine local calcium concentration from internal stores or entry from the L-type and T-type currents across the membrane. Parameters for calcium dynamics were adjusted to slow calcium dependent inactivation while still allowing the model to produce spikes. The general model for local calcium concentration consists of calcium entering through local T-type and/or L-type channels controlled by rate α, and decaying away from the local site at rate β back to its resting internal concentration $[Ca]_i$. The constant α reflects the volume of the cell close to the cell membrane and carries units of $\frac{mmol}{ms \cdot \mu m^3}$, while rate β carries units of $\frac{1}{ms}$. In the 12a T-type current model, calcium may only enter from the L-type current and the local calcium dynamics are described by

$$\frac{d[Ca]}{dt} = -\alpha(I_{CaL}) - \beta([Ca] - [Ca]_i). \tag{2.28}$$

The 12b T-type current model consists of a sodium and calcium current. In the calcium dynamics equation, only the calcium carrying current is included allowing the local calcium dynamics to be described by

$$\frac{d[Ca]}{dt} = -\alpha(I_{CaT}Ca + I_{CaL}) - \beta([Ca] - [Ca]_i). \tag{2.29}$$

The local calcium concentration was input as the internal calcium concentration in the constant field equation for each version of the model implemented to account for the local change in reversal potential near the membrane. To extend the duration of the plateau phase in the calcium dependent inactivation models, α is small ($0 < \alpha < 1$) to reflect the small concentration of calcium entering a small area of membrane providing less calcium available to bind to the L-type calcium dependent inactivation gate; β is large (> 1) to increase the rate of calcium diffusion away from the local area of membrane to further decrease the amount of available local calcium ion for inactivation of the L-type calcium dependent gate.

2.6 Model Summary

Four versions of our model were constructed for *Lymnaea stanglis* ventricular action potential simulation consisting of differences between the L-type and T-type current models. Models were constructed with and without the calcium dependent inactivation (CDI) gate by omitting the calcium dependent gate of the L-type current, and with the LCa_v3-12a or LCa_v3-12b T-type current model. These models are referred to as the "CDI-free 12a model", "CDI-free 12b model", "CDI 12a model", and "CDI 12b model" for the omitted CDI and LCa_v3-12a T-type current model, omitted CDI and LCa_v3-12b T-type current model, present CDI and LCa_v3-12a T-type current model, and present CDI and LCa_v3-12b T-type current, respectively. The final CDI-free model consists of 12 differential equations involving 14 variables and 38 parameters, and the CDI model consists of 16 differential equations involving 18 variables and 52 parameters. The model was implemented in MATLAB for numerical

simulations.

Initial values for the gating variables were taken from Matsuoka et al., 2003. The voltage was set at its recorded resting potential by Yeoman & Benjamin, 1999 at -60 mV, external ionic concentrations were set to those used in the physiological saline solutions, and internal solutions were set to 4.722 mM, 45 mM, and 0.00002049 mM for sodium, potassium, and calcium, respectively.

3 Model Results

Simulations were performed on all four versions of the model with various parameter modifications to represent blocked channels and reduced ionic currents. Channel blocks were studied as convert factor reductions of 25%, 50%, 75% and 100% obtained by multiplying the convert factors by 0.75, 0.5, 0.25, and 0, respectively. This was performed on the T-type conductance and L-type conductance separately to determine the role of the two inward currents in the action potential shape or pacemaking. External sodium and calcium concentrations were altered by reducing them separately to 75%, 50%, 25% and 0% of the physiological level (Tables 6 and 5) as used by Yeoman & Benjamin, 1999 in their microelectrode and patch clamp recordings of *Lymnaea stagnalis* ventricle cells. Reducing sodium or calcium will determine the physiological role of each ion in action potential shape and generation of the model ventricle cell.

In simulation runs using each of the four model versions, results were recorded to describe the shape and frequency of action potential generation. Action potential shape was examined as length of time between each action potential upstroke, length of time of the plateau phase, upstroke peak potential, and length of time for the pacemaker potential by using both approximations from plots and the findpeaks MATLAB function (Figure 3.1). Results for length of time of pacemaker potential and length of plateau were approximated as follows using the plots generated to estimate the starting and end points (Figure 3.1). Start and end times for length of the plateau phase were consistently approximated as the end of the transient repolarization phase marked by the reduced slope of voltage, and the beginning of the final repolarization phase marked by the steep downward voltage slope, respectively. Start and end times for length of the pacemaker potential were consistently approximated as the change in direction of voltage slope from downward to upward after the final repolarization phase, and the steep upward slope in voltage at the beginning of the upstroke, respectively. Peak currents for the T-type current and L-type current were also recorded. Results are not taken as quantitative conclusions about the ventricular action

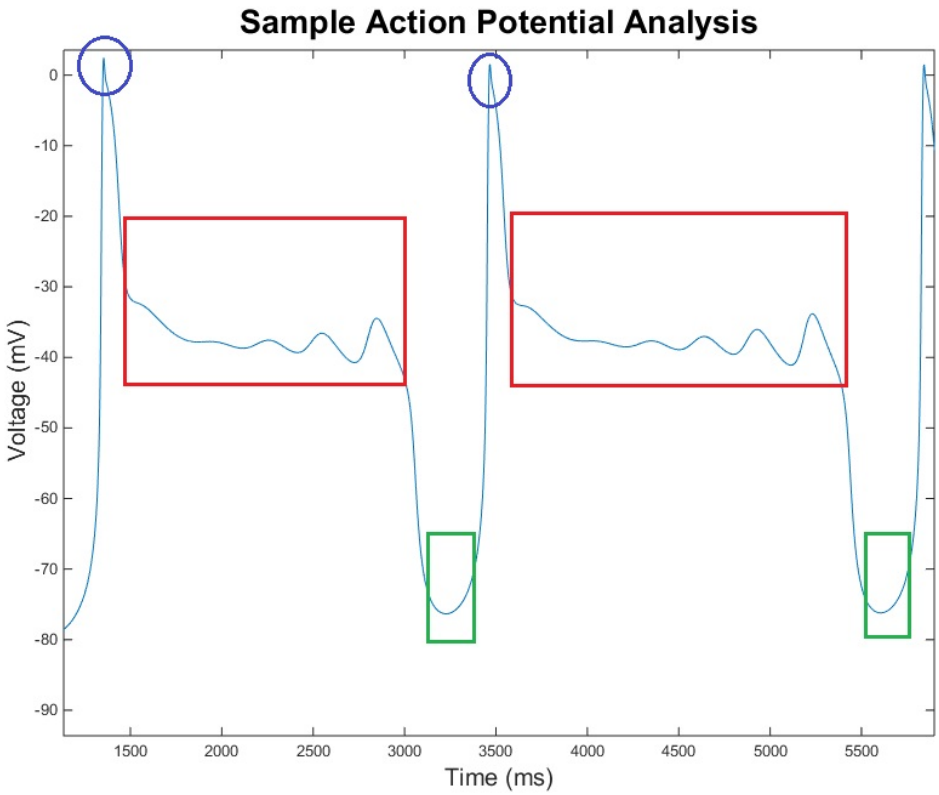

Figure 3.1: Sample analysis of action potentials generated with the model. The blue circle marks the voltage peak of the action potential which was recorded for each run. Time between upstrokes was measured as the time between these peaks. The red box marks the length of the plateau phase measured as the end of the transient repolarization phase and beginning of a relatively stable voltage to the beginning of the final repolarization with a sharp voltage decrease. The green box marks the length of the pacemaker potential measured as the end of the sharp voltage decrease from the final repolarization phase to the sharp voltage increase of the upstroke.

potential but instead are used to describe qualitative trends under various conditions.

3.1 CDI-Free model

Two separate CDI-free models were constructed to examine the differences between LCa_v3-12a and LCa_v3-12b in the cardiac action potential. The CDI-free 12a model was constructed first to determine convert factors necessary to create an action potential similar in shape to that described by Yeoman & Benjamin, 1999. Once final parameters were determined, the same convert factors were implemented in the CDI-free 12b model.

Convert factors of LCa_v3-12a T-type, L-type, transient outward and delayed rectifier currents were chosen such that the model would give oscillating action potentials without an applied current. The P_x values were further adjusted to give an action potential with a plateau phase lasting approximately two seconds and a peak upstroke potential near 0 mV. The final chosen P_x values for both CDI-free models are given in Table 1.

Simulating physiological saline and zero applied current, the CDI-free 12a model features oscillating action potentials with the five phases of the a cardiac action potential (Figure 3.3). A pacemaker potential, phase 4, slowly depolarizes the cell until threshold is reached to initial an upstroke, phase 0. Immediately after the upstroke is a transient repolarization, phase 1, followed by a plateau, phase 2, and final repolarization ending the action potential, phase 3. The CDI-free 12b model also displays the same action potential phases.

Figure (3.2) also displays the currents active during the action potential. Voltage and currents underlying the pacemaker potential are examined in Figure (3.4) and the upstroke is examined in Figure (3.5). The T-type current begins to activate after repolarization to initiate the pacemaker potential. The T-type current slowly rises in amplitude until threshold

Table 1: Parameters used to simulate ventricular action potential without the calcium dependent gate included in the L-type model

P_{CaT}	P_{CaL}	P_{to}	P_{Kr}
0.05	0.6	1.25	3.3

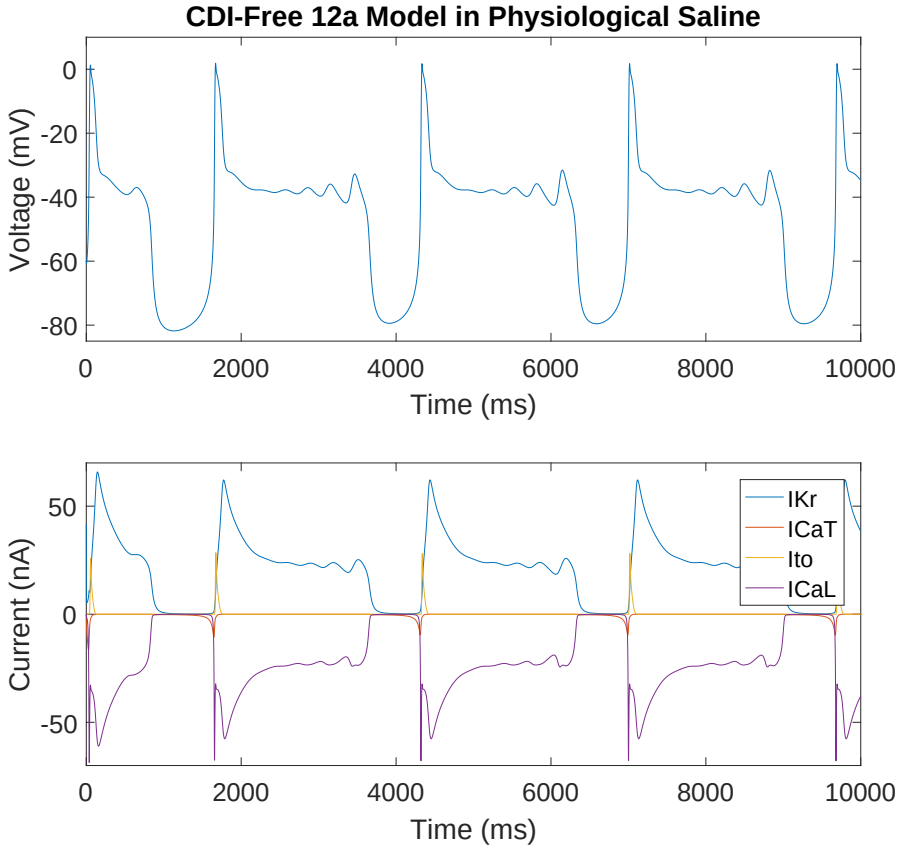

Figure 3.2: CDI-Free 12a Model: Time course of action potentials and currents in physiological saline.

voltage is reached to initiate the upstroke. At the beginning of the upstroke, the T-type current peaks which leads to the activation of the L-type current. The L-type current continues the upstroke as the T-type current inactivates and the transient outward current activates to cause the transient repolarization phase. The delayed rectifier current slowly activates after inactivation of the T-type current and competes with the L-type current. The L-type and delayed rectifier currents are approximately equal and opposite in amplitude causing no net change in voltage and therefore the plateau phase. As the ultra slow inactivation gate of the L-type current gradually reduces the L-type current amplitude, the voltage eventually drops low enough to turn off the L-type current. The delayed rectifier current dominates to repolarize the cell to approximately -77 mV. The CDI-free 12b model also displays the same time course of current activity.

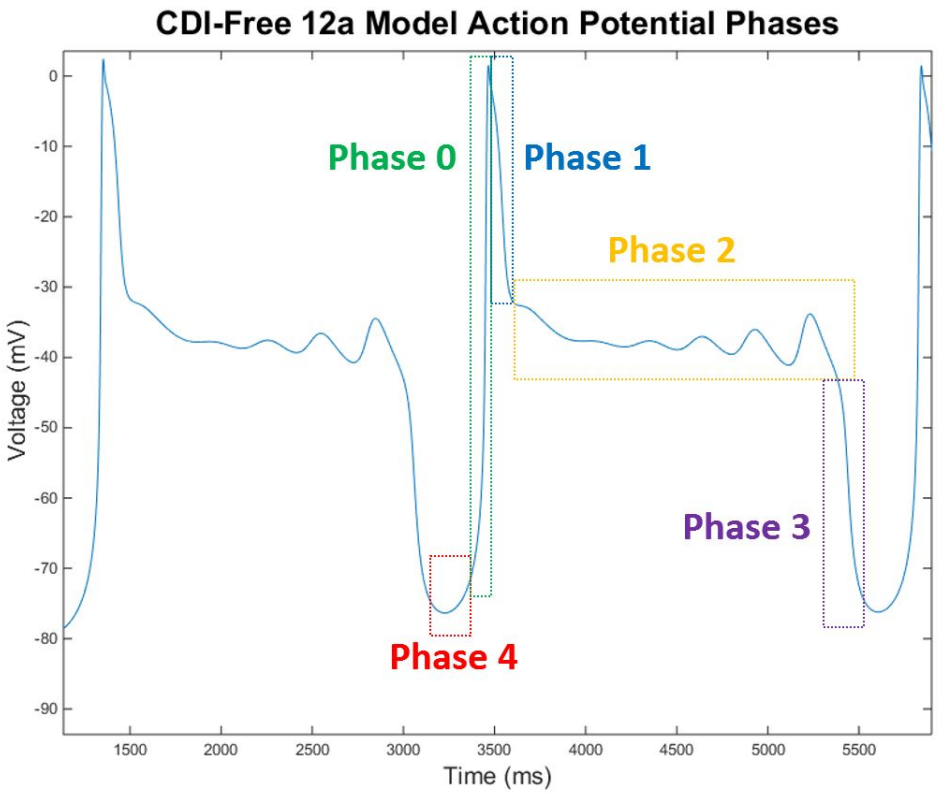

Figure 3.3: CDI-Free 12a Model: Ventricle action potential phases of the simulation.

The two peaks seen in the L-type current are due to the driving force and not a change in gating. The L-type current model peaks at -10 mV, however the action potential upstroke extends past the peak. As the transient outward current activates to drive the potential down to the plateau level, the L-type current peaks a second time as it crosses its peak potential. Both of these peaks are recorded in the following tables for comparison in each condition.

The plateau phase contains oscillations seen both in the potential and the L-type and delayed rectifier currents. Oscillations are due to the voltage dependent activation gate of the L-type current. As the ultra slow inactivation gate inactivates the current, the voltage dependent activation gate oscillates between an active and resting state. As the oscillations in the activation gate increase in amplitude, the voltage eventually reaches a level to close the activation gate and completely inactivate the L-type current. Oscillations seen in the delayed

rectifier current are due to the change in driving force following the voltage oscillations.

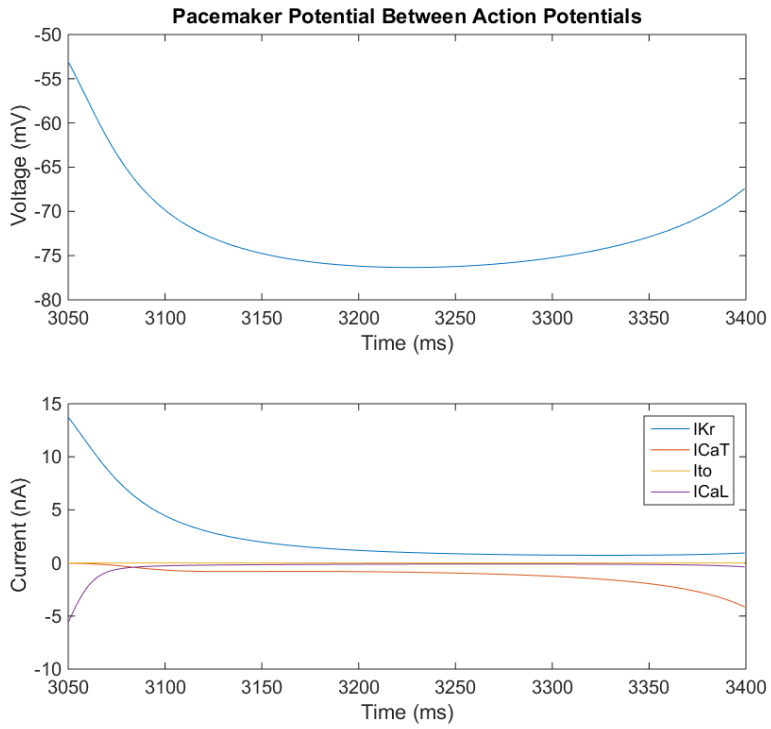

Figure 3.4: CDI-Free 12a Model: Time course of the pacemaker potential and pacemaker currents.

The pacemaker potential and pacemaker currents are examined in Figure (3.4). After the final repolarization phase of the action potential, the delayed rectifier current decreases in amplitude to near zero. As the delayed rectifier current hyperpolarizes the cell, a fraction of the T-type current is activated. This small window current gradually rises in amplitude until it surpasses the small amplitude of the residual delayed rectifier current. The T-type current continues to rise in amplitude until threshold is reached to initiate an upstroke. The L-type current is also active during the pacemaker potential, although its amplitude is approximately 15% of the T-type current. Both L-type and T-type currents contribute to the pacemaker potential, however the T-type amplitude carries the majority of the inward pacemaker current. The CDI-free 12b model displays similar activity during the phases of the action potential (not shown).

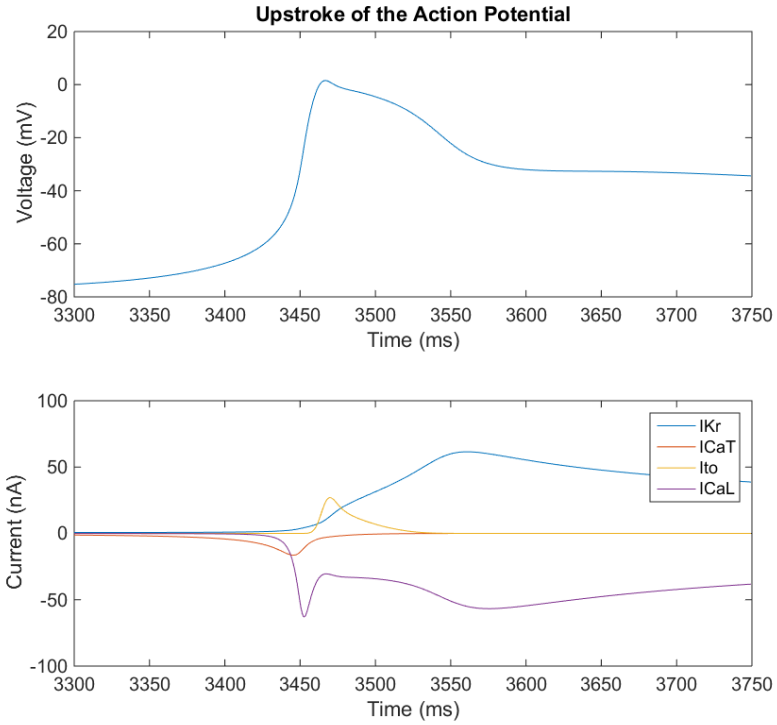

Figure 3.5: CDI-Free 12a Model: Time course of the upstroke and underlying currents.

Simulations were run in identical physiological conditions for the CDI-free 12a and CDI-free 12b models (Table 2). The CDI-free 12a and 12b models display the same qualitative characteristics of their action potential with the largest difference contained in the frequency of action potentials. The CDI-free 12b model was found to have a longer pacemaker potential and longer time between action potential upstrokes than the CDI-free 12a model. There was a smaller peak current to initiate the upstroke for the 12b model than the 12a model.

Table 2: CDI-Free 12a and 12b model results in physiological saline. Percent Difference highlights significant changes in characteristics when implementing the 12a or 12b T-type current model

Physiological Saline	CDI-Free 12a	CDI-free 12b	Percent Difference (%)
Period of Upstroke (s)	2.375	2.673	11.806
Length of Plateau (ms)	1770	1750	1.136
Length of Pacemaker Potential (ms)	250	500	66.667
Upstroke Peak Voltage (mV)	1.53	1.7594	13.947

The upstroke peak voltage, L-type peak current, and length of plateau were found to be similar between the two models. Since the L-type current displays two peaks, one during the upstroke and a second during the beginning of the plateau, the amplitudes of both peaks were recorded and compared.

Simulations were run with increasing T-type current block by reducing P_{CaT} to 75%, 50%, 25%, and 0% of its value given in Table 1. Results are displayed in Figures 3.6, 3.7, and 3.8 where 0 ms duration indicates an abolished phase. Increasing T-type current block showed an increase in length of time of the pacemaker potential and time between upstrokes, slowing the frequency of spikes. Blocking T-type current, however, had a negligible affect on the length of the plateau, peak of the L-type current, or peak of the upstroke. At complete T-type current block, spikes were still capable because of the residual L-type current carrying the pacemaker potentials although at a much slower rate of once per 42 seconds.

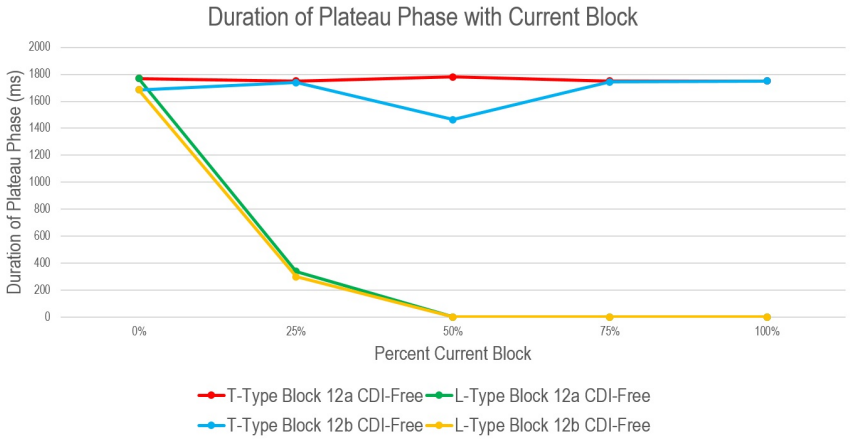

Figure 3.6: CDI-Free plateau duration during current block. Percentages refer to the percent of the current present in the model. 0 ms indicates the plateau phase has been abolished.

Simulations were run with increasing L-type current block by reducing P_{CaL} to 75%, 50%, 25%, and 0% of its value given in table 1. Results are displayed in Figures 3.6, 3.7, and 3.8. Increasing L-type block caused a greater change in the action potential shape than did blocking the T-type current. At 25% L-type current block, the plateau length was severely reduced. By 50% block, the plateau phase was abolished. Frequency of the upstroke was reduced with increasing L-type current block since the plateau phase was greatly reduced

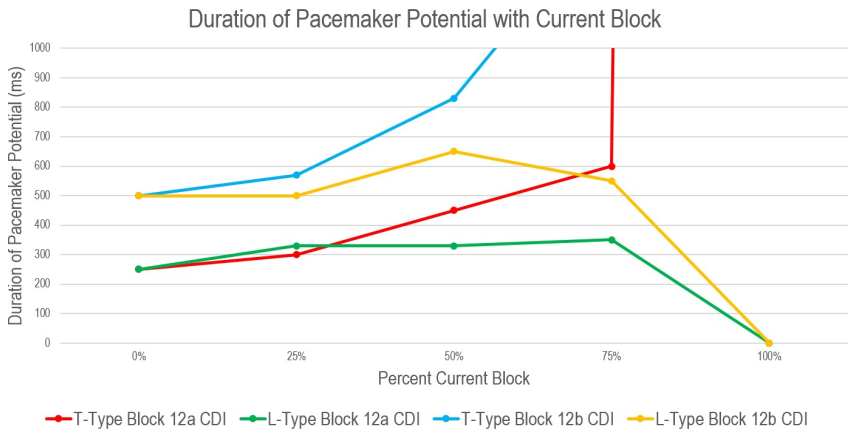

Figure 3.7: CDI-Free pacemaker potential phase duration during current block. Percentages refer to the percent of the current present in the model. 0 ms indicates the plateau phase has been abolished.

or abolished, but the length of the pacemaker potential remained relatively unchanged. Increasing L-type current block reduced the peak of the upstroke. At 100% current block, spiking was abolished. The initial behaviour of the model cell displayed some fluctuations in voltage due to some activation of the T-type current, however these damped oscillations reached a stable equilibrium in voltage and current. The steady state net current was approximately zero; residual currents from the outward delayed rectifier current and inward T-type current were equal and opposite resulting in a steady state voltage level.

Sodium concentrations were reduced to 75%, 50%, 25% and 0% of their physiological concentrations for the CDI-free 12a and CDI-free 12b models. Results are displayed in figures Results are displayed in Figures 3.9, 3.10, and 3.11. Reducing sodium concentrations appeared to have negligible affect on the length of the plateau phase, the peak of the L-type current, or the peak of the upstroke. Reducing sodium caused an increase in the length of the pacemaker potential and therefore time between upstrokes. At 0% sodium, spikes are abolished in the 12a model but not the 12b model. For the CDI-free 12b model, the pacemaker potential is greatly extended but spikes are not abolished. The T-type current continues to be an outward current contributing to the pacemaker potential. Spikes are abolished in 0% sodium for the CDI-free 12a model. The T-type current changes to an

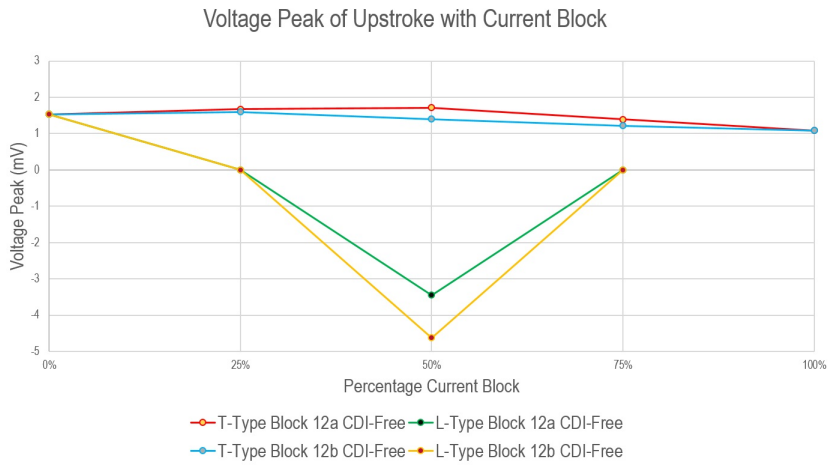

Figure 3.8: CDI-Free voltage peak of the upstroke during current block. Percentages refer to the percent of the current present in the model. Spiking was abolished at 100% L-type block represented in the figure by an absent data point at 100%.

outward current that competes with the small residual L-type current during the pacemaker potential. The outward T-type and delayed rectifier currents oppose the inward L-type current to result in a zero net current. The voltage reaches steady state potential lasting indefinitely.

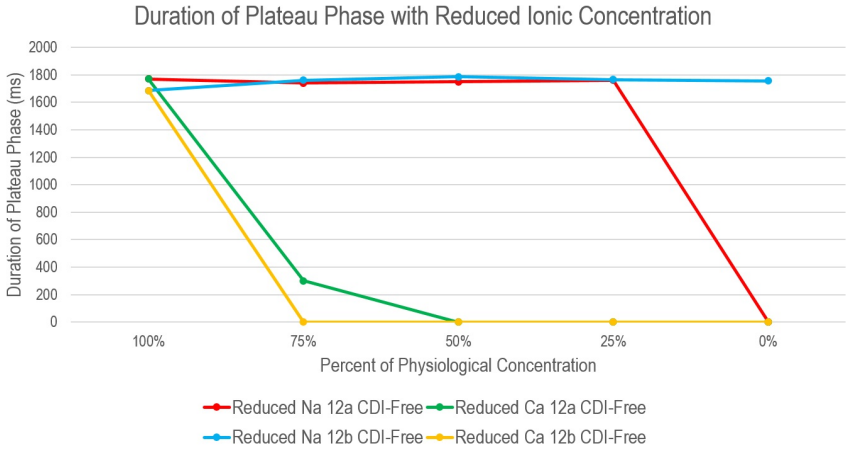

Figure 3.9: CDI-Free plateau duration during current block. Percentages refer to the percent of the current present in the model. 0 ms indicates the plateau phase has been abolished.

Calcium concentrations were reduced to 75%, 50%, 25% and 0% of their physiological concentrations for the CDI-free 12a and CDI-free 12b models. Results are displayed in figures Results are displayed in Figures 3.9, 3.10, and 3.11. The length of the pacemaker

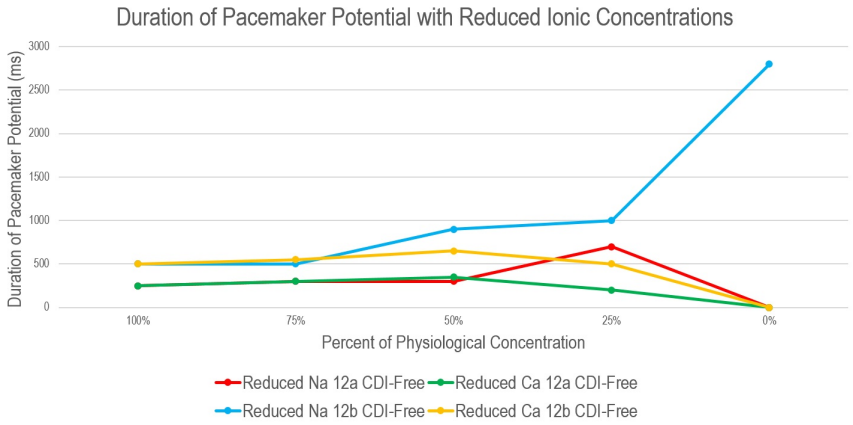

Figure 3.10: CDI-Free pacemaker potential phase duration during current block. Percentages refer to the percent of the current present in the model. 0 ms indicates the plateau phase has been abolished.

potential was relatively unchanged in the CDI-free 12a model, and increased in the CDI-free 12b model. In both models, the peak of the upstroke decreased with decreasing calcium concentration. By 50% calcium concentration, the plateau phase of the action potential was abolished and the action potential presented a fast spike shape. At 0% calcium, spikes were abolished in both models. The initial behaviour displayed some voltage depolarizations due to activated T-type current, however these oscillations were damped and reached a steady state voltage. The steady state net current again was approximately zero due to opposing amplitudes of the T-type and delayed rectifier currents.

3.2 CDI model

Two separate models including the calcium dependent inactivation gate were constructed using the LCa_v3-12a or LCa_v3-12b current models. Including calcium dependent inactivation greatly reduced the length of the plateau phase in comparison to the CDI-free model, and more closely resembled the fast spike action potential shape. Convert factors, P_x, were adjusted from those used in the CDI-free models in order to produce oscillating action potentials under zero applied current. The final P_x values used are found in Table 3. In order to create a longer plateau with a shape possessing a similar arc to the spike-plateau

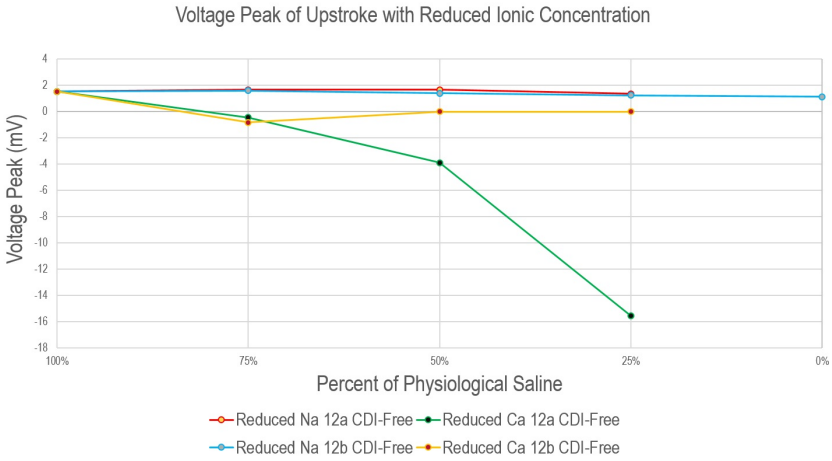

Figure 3.11: CDI-Free voltage peak of the upstroke during current block. Percentages refer to the percent of the current present in the model. Spiking was abolished at 100% L-type block represented in the figure by an absent data point at 100%.

shape described by Yeoman & Benjamin, 1999, two rates of the L-type calcium dependent gate were adjusted to prolong the plateau phase and decrease the difference between the voltage peaks of upstroke and plateau phase. The adjusted rates are found in Appendix A.5. The rate between the calcium bound covered and calcium bound uncovered state was increased by a factor of 30 and the rate between the calcium bound uncovered and calcium bound covered state was slowed by a factor of 100 to slow the rate of calcium dependent inactivation.

The 12a and 12b CDI models feature oscillating action potentials with zero applied current in physiological saline (Figure 3.13). The action potential consists of the five phases described in the CDI-free model (Figure 3.12). A pacemaker potential (phase 4) brings the voltage up to the threshold level to initiate the upstroke (phase 0). There is a very brief transient repolarization (phase 1) followed by a short plateau (phase 2). The action potential terminates with a final repolarization (phase 3) and the pacemaker potential initiates again.

Table 3: Parameters used to simulate ventricular action potential including the calcium dependent gate in the L-type model

P_{CaT}	P_{CaL}	P_{to}	P_{Kr}
0.019231	1.0577	0.28846	1.5385

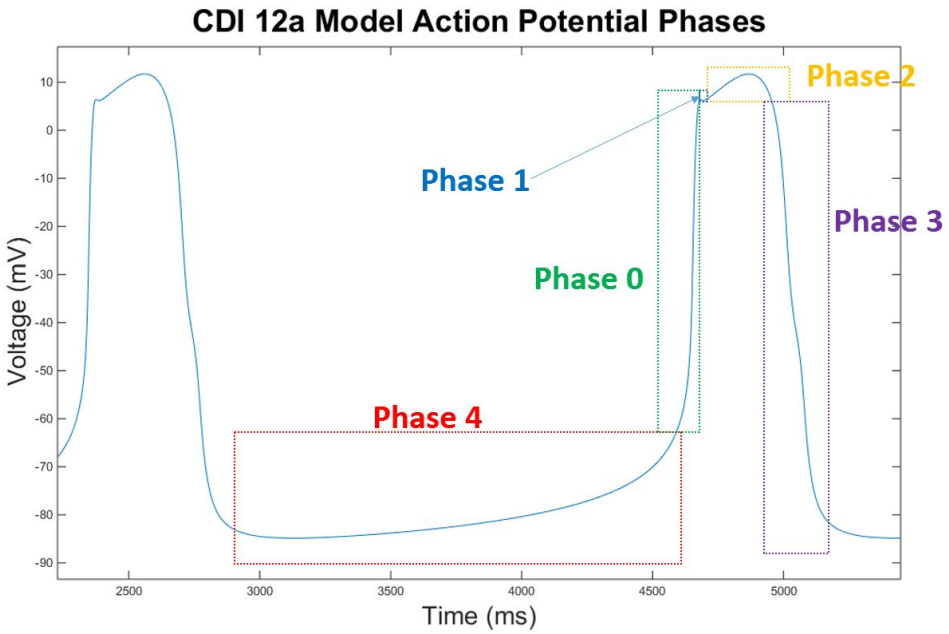

Figure 3.12: CDI 12a Model: Time course of action potential phases.

The CDI 12b model displays the same features.

The time course of activated currents are also displayed in Figure (3.13) and during the plateau in Figure (3.14). The T-type current is active during the pacemaker potential and grows in amplitude until the upstroke is initiated. The T-type current peaks as the L-type current becomes activated. The L-type current spikes during the upstroke as reduces in amplitude at the beginning of the plateau phase. After the peak of the L-type current, the transient outward current is activated and causes the transient repolarization phase. As the transient outward current inactivates during the plateau phase, the delayed rectifier current slowly activates and competes with the L-type current. As the L-type current inactivates, the delayed rectifier current becomes larger causing a net outward current. The L-type current peaks for a second time as the potential drops to its peak potential, and finally inactivates to allow the delayed rectifier current to repolarize the voltage back to the pacemaker potential.

The pacemaker current between the final repolarization phase and upstroke consists of the T-type current and L-type current (Figure 3.15). The delayed rectifier current inactivates slowly at the end of the final repolarization and beginning of the pacemaker potential as

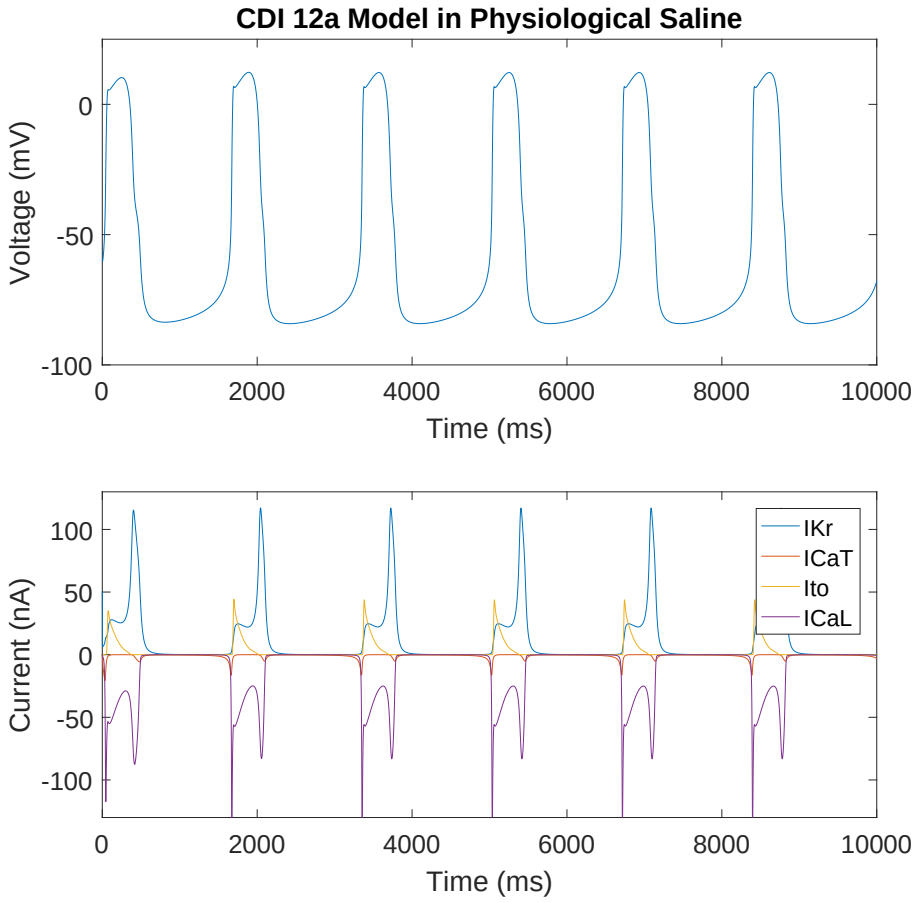

Figure 3.13: CDI 12a Model: Time course of action potentials and currents in physiological saline.

the T-type window current begins to activate. The L-type current also contributes to the pacemaker current, however the T-type window current has a much larger amplitude carrying the majority of the pacemaker current.

Similarities and differences between the CDI 12a and 12b models were examined in physiological saline (Table 4). Both 12a and 12b models features plateaus lasting 260 ms and peak voltages of the upstroke and plateau reaching approximately 6 and 12 mV. Peaks of the L-type current at the upstroke, plateau, and repolarization phase all remain approximately the same amplitude between the two models. Differences between the 12a and 12b models are seen in spike frequency. Pacemaker potentials are longer in the 12b model than the 12a model, and upstrokes are generated with decreased frequency as a result.

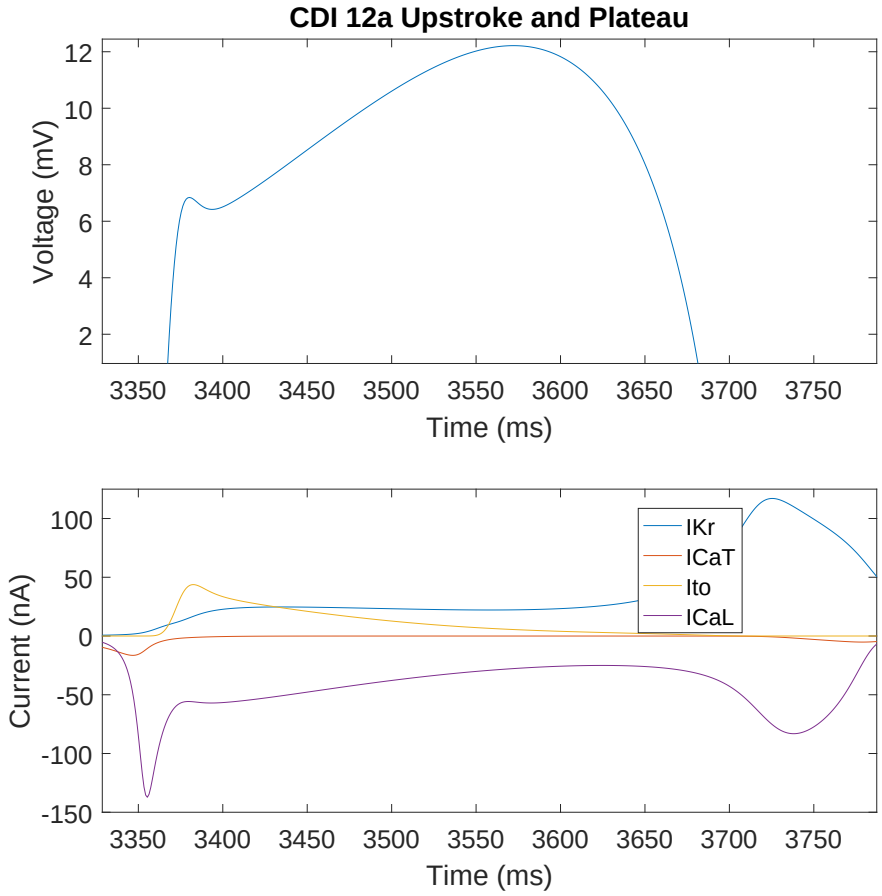

Figure 3.14: CDI 12a Model: Time course of action potentials and currents in physiological saline.

Simulations were run with increasing T-type current block by reducing P_{CaT} to 75%, 50%, 25%, and 0% of its value given in Table 3. Results are displayed in Figures 3.16, 3.17, and 3.18. Reducing T-type current convert factors affected the frequency of action potentials but not their shape. Action potentials remained at the relative same peak of the upstroke and plateau, and plateaus remained at 260 ms in length. The peaks of the L-type current recorded at the upstroke, plateau, and repolarization phases slightly increased with increasing T-type current block. As T-type current block increased, the length of the pacemaker potential also increased. At 100% T-type current block spikes were not abolished, however the increase in time between upstrokes was large enough that it is unlikely they would be maintained in physiological conditions.

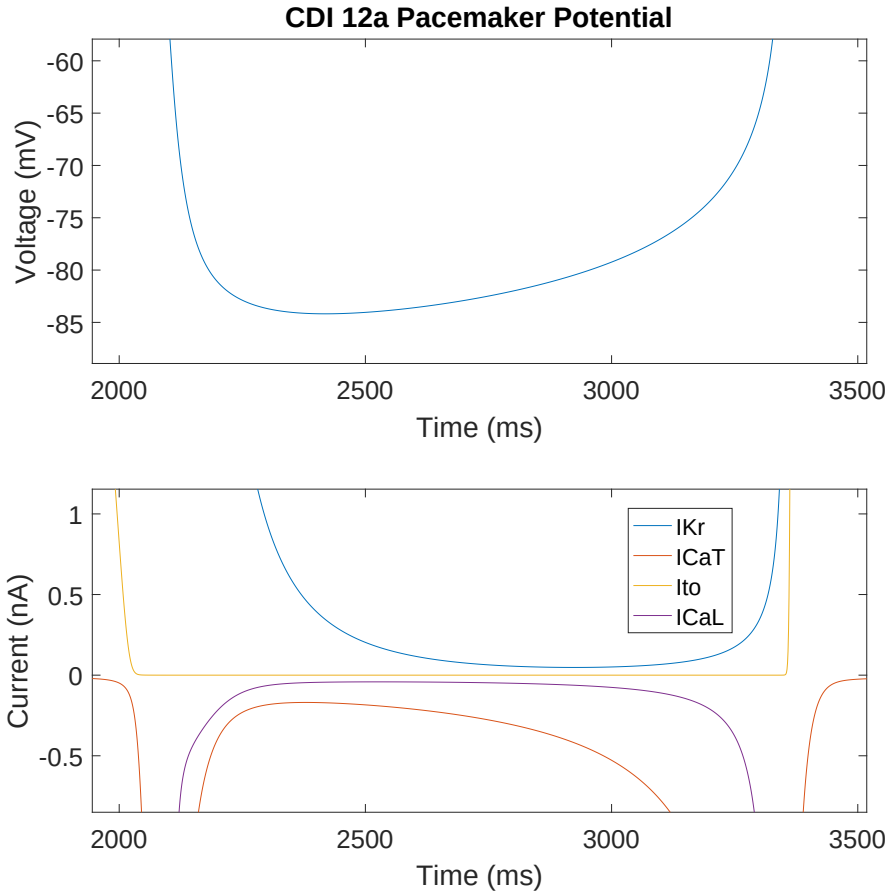

Figure 3.15: CDI 12a Model: Time course of action potentials and currents in physiological saline.

Simulations were run with increasing L-type current block by reducing P_{CaL} to 75%, 50%, 25%, and 0% of its value given in Table 3. Results are displayed in Figures 3.16, 3.17, and 3.18. Reducing the L-type current in the model by 75% abolished spiking altogether. In each case of increased L-type block, the net current reached a steady state value of approximately zero allowing the voltage to remain at an equilibrium potential. The inward L-type and T-type currents opposed the outward delayed rectifier current in each case.

Sodium concentrations were reduced to 75%, 50%, 25% and 0% of its physiological level. Results are displayed in Figures 3.19, 3.20, and 3.21. Reducing sodium had no effect on the peak of the upstroke or plateau, nor the length of the plateau phase. In both CDI 12a and CDI 12b models, the length of the pacemaker potential was increased with decreasing

Table 4: CDI 12a and 12b model results in physiological saline. Percent Difference highlights significant changes in characteristics when implementing the 12a or 12b T-type current model.

Physiological Saline	CDI 12a	CDI 12b	Percent Difference (%)
Period of Upstroke (s)	1.6726	2.3066667	31.868
Length of Plateau (ms)	260	260	0
Length of Pacemaker Potential (ms)	1100	1730	44.522
Upstroke Peak Potential (mV)	6.6525	6.3844	4.112

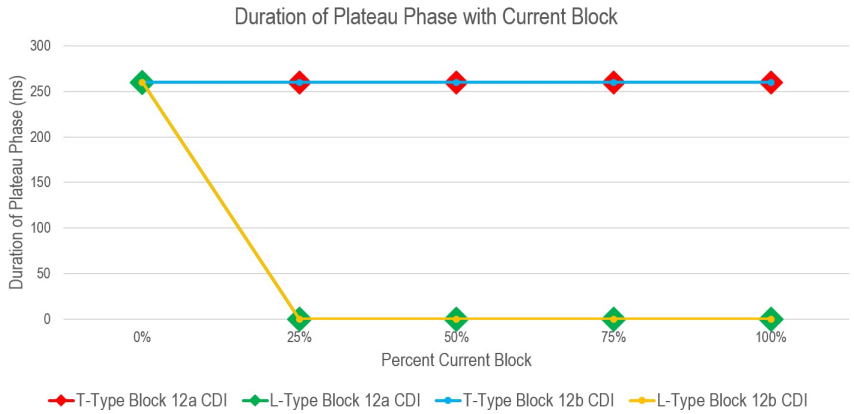

Figure 3.16: CDI plateau duration during current block. Percentages refer to the percent of the current present in the model. 0 ms indicates the plateau phase has been abolished.

sodium concentration. At 0% sodium, spikes were not abolished in the 12a model however spikes were generated once per 73 seconds which is unlikely to be maintained in physiological conditions. The 12b model had a pacemaker potential lasting 8.7 seconds in 0% sodium. The 12a model showed a 2333% increase in the length of the pacemaker potential from 25% sodium to 0% calcium concentration, versus a 217% increase in the 12b model.

Calcium concentrations were reduced to 75%, 50%, 25% and 0% of its physiological level. At 75% calcium concentration, spikes were abolished in both 12a and 12b models. The net current reaches a steady state value of approximately zero as the sum of the inward T-type and L-type currents equal the outward delayed rectifier current in each case of reduced calcium.

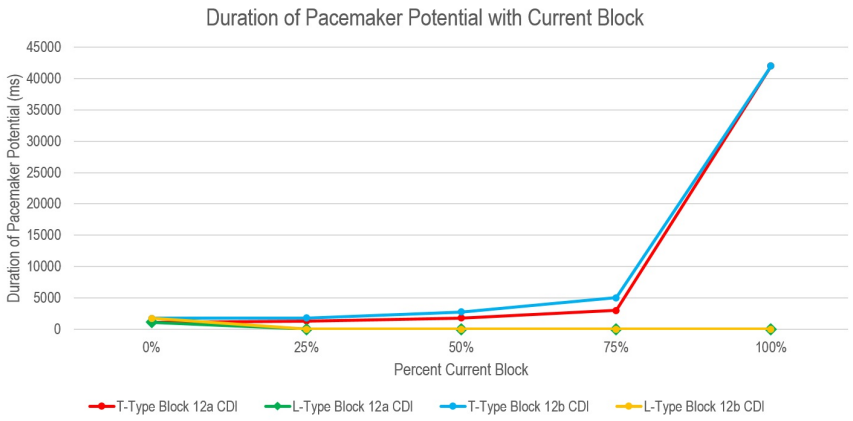

Figure 3.17: CDI pacemaker potential phase duration during current block. Percentages refer to the percent of the current present in the model. 0 ms indicates the plateau phase has been abolished.

4 Discussion

4.1 Physiological Role of Currents in the model

Numerical simulations of the *Lymnaea stagnalis* ventricular action potential provide insight into the physiological role of both the T-type current and sodium during the five phases of the action potential. Both 12a and 12b T-type currents of *Lymnaea stagnalis* play a major role as the primary pacemaker in our model by activating at a subthreshold voltage to bring the potential to the L-type activation level. The L-type current is primarily responsible for the upstroke and plateau phase of the action potential. The 12a and 12b currents play the same physiological role in our model but differ in rate of pacemaking. The sodium exclusive 12a current provides a shorter pacemaker potential in the action potential model than the sodium and calcium carried 12b current, suggesting the sodium carried current is responsible for spontaneous spike generation. The following discussion provides hypotheses of the physiological role of each current in our model comparing it to the roles played in both mammalian ventricle and SA node action potentials.

The time course of activation of the four currents during the simulated action potential using physiological ionic concentrations provides suggestions of their physiological roles.

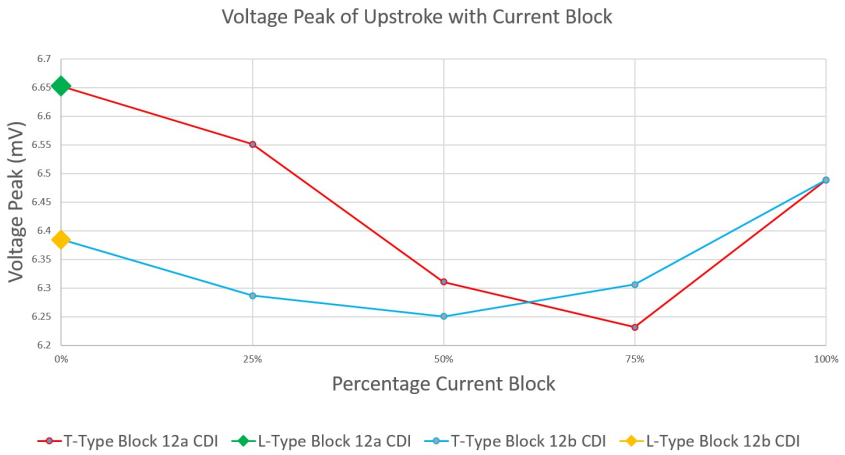

Figure 3.18: CDI voltage peak of the upstroke during current block. Percentages refer to the percent of the current present in the model. Spiking was abolished with any reduction in L-type current represented in the figure by an absent data points at 25%, 50%, 75%, and 100%.

Action potentials generated using the CDI and CDI-Free models showed similarities between both recordings performed in this thesis and by Yeoman & Benjamin, 1999. The CDI-free model generated behaviour similar to bursts of spike-plateau action potentials of *Lymnaea stagnalis* ventricle cells recorded in these experiments with approximately 250 ms between the final repolarization of a previous spike and upstroke of the next spike. The model lacked variation between spikes both seen in these recordings and described by Yeoman & Benjamin, 1999, and instead was highly rhythmic with conserved characteristics. The model does not account for the highly variable length of plateau duration. The CDI-free model features a plateau duration similar to that described by Yeoman & Benjamin, 1999, where the CDI model features a plateau duration closer to the recordings performed in the Spafford lab of 260 ms. The two L-type models encompass different characteristics of the recordings described both here and (Yeoman & Benjamin, 1999).

The transient outward current is responsible for the transient repolarization phase of the action potential. In simulations using physiological conditions, the transient outward current is only active during the upstroke and inactivates during the plateau phase. During the period when the voltage decreases during the transient repolarization phase, the transient

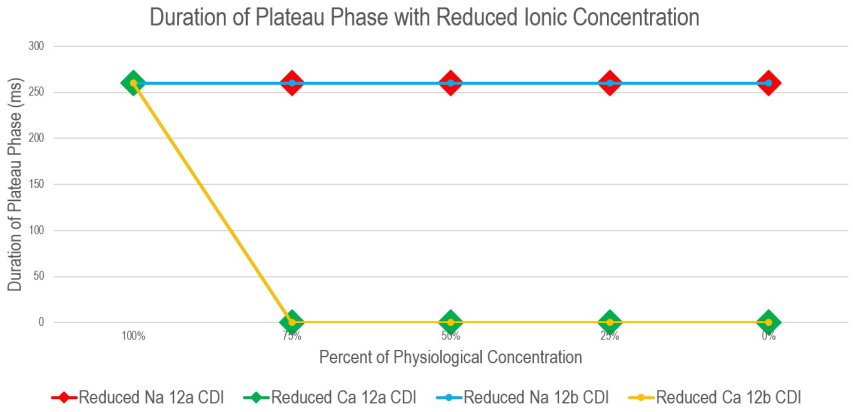

Figure 3.19: CDI plateau duration during current block. Percentages refer to the percent of the current present in the model. 0 ms indicates the plateau phase has been abolished.

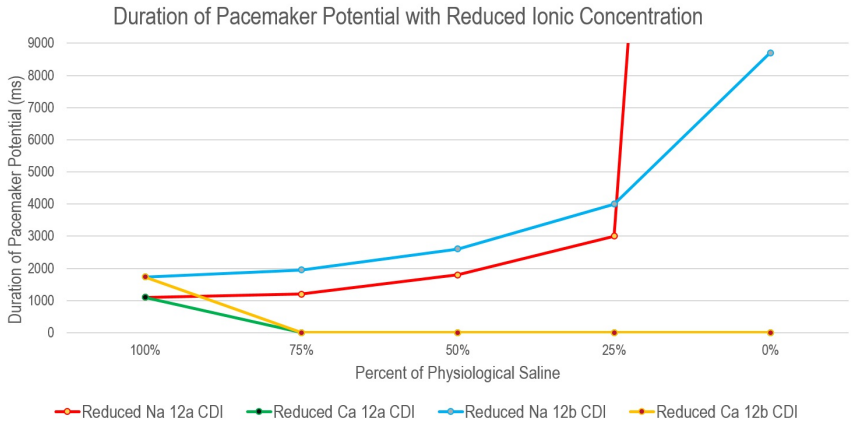

Figure 3.20: CDI pacemaker potential phase duration during current block. Percentages refer to the percent of the current present in the model. 0 ms indicates the plateau phase has been abolished.

outward current is the largest outward current active. Since it is not active during any other phase of the action potential, it is not assumed to play another significant role. This brief outward current would then act to contribute in controlling the peak of the action potential by opposing the inward currents raising the potential. This suggests that I_{to} is the major contributor to driving the potential down during this brief phase.

The delayed rectifier is responsible for the plateau and final repolarization phase of the action potential, and for activating the pacemaker current. The current is slow to activate relative to the other three currents present, and does not significantly contribute to the net

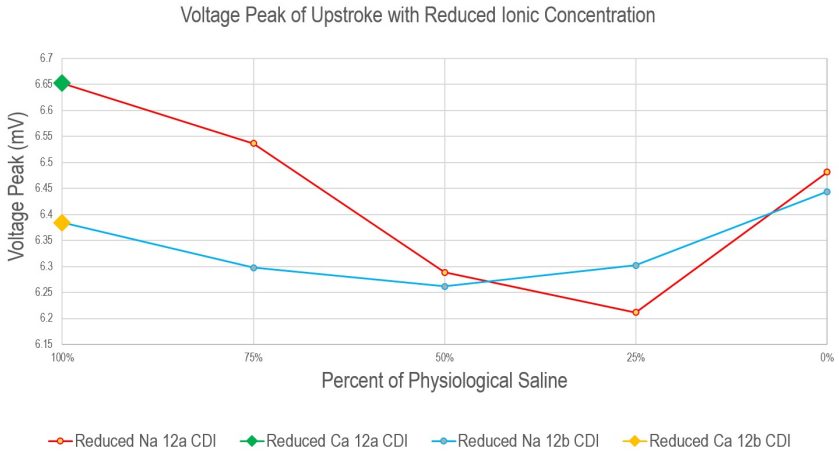

Figure 3.21: CDI voltage peak of the upstroke during current block. Percentages refer to the percent of the current present in the model. Spiking was abolished with any reduction in calcium concentration.

current until the plateau phase of the action potential. It is equal and opposite in amplitude to the L-type current, and is the only outward current active during the plateau. This balanced outward current contributes to the zero net current necessary for the plateau phase. I_{Kr} is also responsible for ending the action potential with a final repolarization phase. It remains active once the L-type current inactivates and is responsible for bringing the potential back to "rest." The delayed rectifier current causes the pacemaker potential to activate by driving the potential down to a level where a fraction of the T-type channels are able to recover from inactivation and activate their window current.

The T-type current in both the 12a and 12b models is responsible for pacemaking and initiating the upstroke. The 12a T-type current was initially postulated to carry the upstroke of the action potential since it passes almost exclusively sodium ions, assuming it plays a similar role to sodium channels during the vertebrate ventricular action potential. In the full Kyoto model, the rate of rise of the upstroke is dependent on the sodium current through sodium channels (Matsuoka et al., 2003). However in the model, the T-type current was only responsible for initiating the upstroke by bringing the potential to the level of activation for the L-type current. The T-type current is slower than traditional fast sodium currents, and the L-type current has to activate and contribute to the upstroke. The T-type channel then

is only responsible for raising the potential to a level for the L-type current to take over the upstroke. This is apparent when simulating T-type current block. Blocking the T-type current had no effect on the peak of the upstroke, suggesting that this is dictated by the L-type current. In the 12a and 12b models, varying external sodium concentrations also had no effect on the peak of the upstroke suggesting that this is not dependent on the T-type current.

The T-type current is primarily responsible for rhythmic firing. It is completely inactivated during the plateau phase of the action potential, and becomes active once again at the end of the final repolarization phase. The delayed rectifier current is able to activate it by bringing the cell membrane to a potential that begins to activate the T-type window current. This small leak current is large enough to slowly drive the membrane potential up through a pacemaking current. As the window current increases the cell potential, the amplitude of the T-type current increases causing a positive feedback loop to recruit more channels for the pacemaker current. The T-type current exponentially increases to increase the membrane potential to threshold of the L-type current which initiates a spike. The T-type current is thus able to dictate the rate of pacemaking by controlling the speed at which L-type current activation is reached to initiate a spike. In the model simulation, blocking the T-type current and reducing sodium concentration caused the largest decrease in pacemaking rate. The 12a models featured either abolished spiking behaviour from lack of pacemaker current (spiking could still occur with applied current [not shown]) in the CDI-free model or significant reduction to rate of spiking to a rate unlikely to be physiologically possible in a living organism. We postulate the T-type current is the primary pacemaker for *Lymnaea* ventricular cells.

The upstroke and plateau phase of the action potential are carried by the L-type current. In physiological conditions, the L-type current is activated at the peak of the T-type current and is the only active inward current during the plateau phase. The L-type current opposes the delayed rectifier current to delay final repolarization and cause the plateau phase. This is apparent in simulations blocking the L-type current. Increasing L-type block affects the

peak of the upstroke, duration of the plateau phase, and spiking activity. The peak of the upstroke and duration of the plateau decrease with increasing L-type current block, showing that this inward current is responsible for these two phases. Blocking L-type current eventually abolishes all spiking activity regardless of T-type activity. T-type current shows some fluctuation, but not enough to drive an action potential showing that spiking is entirely reliant on the L-type current. Blocking L-type current had little effect on the duration of the pacemaker potential, despite having a small residual current during this phase. Since spikes may still be generated in zero T-type current, the L-type current is still capable of slowly depolarizing the cell to threshold for the L-type to cause an upstroke, however again this rate is much too slow to be physiologically possible in a living organism.

The L-type current model used for the invertebrate cardiac action potential model controlled the length of the plateau phase by its calcium dependent inactivation kinetics. With no calcium dependent inactivation, the CDI-free model could provide plateaus lasting for 2-4 seconds, however this is not a correct assumption. Including calcium dependent inactivation modeled from guinea pig ventricle studies contributes to cardiac spikes lasting approximately 200 ms (Matsuoka et al., 2003). Although this is physiologically correct for vertebrates, this poses a limitation in simulating the elongated plateau phases seen in *Lymnaea stagnalis* (Yeoman & Benjamin, 1999). The L-type current of the *Lymnaea* ventricle cell may then show slower calcium dependent inactivation to achieve a longer plateau, or the model is missing necessary details from internal calcium stores providing this extended plateau phase.

The full Kyoto model is accessible through simBio, a java package for detailed cell models. The ventricular Kyoto model generates action potentials with a 3 nA current pulse. The T-type current of the Kyoto model was replaced with the 12a T-type current model from *Lymnaea stagnalis* and continued to produce action potentials. The sodium current of the Kyoto model was reduced to zero to reflect the lack of sodium current in *Lymnaea* ventricle cells and the simulation was performed again with the 12a T-type current. Maintaining the same parameters as the Kyoto model prevented the system from producing action potentials,

however by raising the convert factor of the T-type current, the system is able to generation action potentials. This is consistent with our model which is able to generate action potentials in the absence of a sodium current and a sodium permeable T-type current.

The roles of the currents of *Lymnaea stagnalis* ventricle cells implemented in the model show similarities between both human SA node and ventricular action potentials. T-type and L-type currents contribute to the action potential as a pacemaker in both SA node (Monfredi et al., 2010) and snail ventricle cell spike simulations, and blocking L-type current in SA node also abolishes spiking behaviour. In both action potentials, the upstrokes are calcium dependent and carried by the L-type current as sodium channels are not found in either cell types (Monfredi et al., 2010). *Lymnaea* ventricle cells are capable of generating spike-plateau action potentials where in both the invertebrate and vertebrate ventricle cells, the plateau phase is carried by the L-type and delayed rectifier currents, the delayed rectifier current repolarizes the cell, and the A-type or transient outward current causes the brief repolarization phase after the upstroke (Grant, 2009).

It was not clear whether the T-type current would play the role of the sodium current in the ventricle cell or the T-type current in the SA node cell. Despite carrying sodium ions, the 12a current did not carry the upstroke of the action potential in simulation and instead was responsible for initiating the upstroke carried by the L-type current. This assumes a more similar role to that of SA node than ventricle cell.

The 12a and 12b T-type models display similar trends in each simulation. Both currents are primarily responsible for pacemaking and initiating the upstroke of the action potential. This is expected since both currents show nearly identical kinetics and biophysical characteristics as found by Senatore et al., 2014. The only significant difference between the models is their ionic permeability which will only alter the amplitude of the current from the difference in driving force due to a smaller difference between internal and external calcium concentrations than sodium concentrations.

The 12b models featured longer pacemaker potentials than 12a models, likely due to dif-

ference in current amplitude. The 12b models had smaller peaks during upstroke generation forcing the L-type current amplitude to increase in order to reach a similar peak potential in the two models. The increased pacemaker potential is due to the difference in driving force from the 12a model because of the calcium carried current. This half of the current has a smaller driving force and therefore contributes less to the window current than an exclusively sodium carried current as in the 12a T-type model.

The 12b model was more resistant to changes in sodium or calcium concentration. Reducing sodium to 0% still allowed spontaneous activity because of the calcium carried current, although at a slower rate. Spiking behaviour was abolished with decreasing calcium concentration because of the dependence on the L-type current. This suggests the sodium current is acting to help carry the calcium current to initiate the upstroke, where the calcium current of the 12b T-type current may be serving another purpose involved in excitation-secretion coupling.

Numerical results from the model show that sodium is involved with action potential generation contrary to conclusions drawn by Yeoman & Benjamin, 1999. Since spikes were still capable of generation with zero sodium present, Yeoman & Benjamin assumed sodium must play no role in the action potential however we show through simulation that the sodium permeable T-type current is involved in pacemaking activity of the ventricle cell. Results agree with Yeoman et al. such that the L-type current carries the calcium dependent upstroke.

The prostate and albumen cells may not require spontaneous electrical activity as the heart, and pacemaking ability of the T-type current may not be its dominant function. Expression of specific channels aside from the 12b T-type current is not known in the prostate or albumen gland cells, however due to the large number of vesicles there is likely an abundance of L-type calcium channels to raise internal calcium levels needed for secretion. The 12b current may serve to both depolarize the cell through the stronger sodium driving force and begin calcium-dependent processes needed for secretion.

The cell features characteristics of both vertebrate ventricle and SA node cells. Since the snail heart is not known to have a localized region of pacemaking (Yeoman & Benjamin, 1999), this is expected as ventricle cells may have to play the role of both pacemaker and muscle cell. Other characteristics such as resting potential in the SA node range (approximately -60 mV, (Monfredi et al., 2010) versus approximately -90 for ventricle cell (Grant, 2009)), lack of inward rectifier current and high input resistance show similarities to SA node cell spikes to resemble the pacemaker region behaviour. However the ventricle cell is also not shown to have a hyperpolarized activated current or "funny" current that is characteristic of vertebrate SA node cells.

4.2 Limitations of the model

The model is used as a tool to qualitatively reverse engineer the invertebrate ventricular action potential but lacks details that may be necessary to provide more complete representation of the true action potential.

Simplifying assumptions made to reduce the complexity of the models may sacrifice visualizing the true behaviour of the action potential. For example, ions are assumed to pass independently of one another without interaction and to cross a channel instantaneously. Especially for the 12b T-type current this may not be the case. Increasing calcium concentration while maintaining sodium concentration showed increase calcium block of the 12b current and overall reduction of current amplitude (Senatore et al., 2014), contrary to an expected increase in current amplitude if these two ions passed independently. Further characterization of this mechanism is required before implementation into a current model, therefore the simplifying assumption on independent current flow was implemented instead.

The action potentials generated using the model do not exactly match the parameters discussed by Yeoman & Benjamin, 1999, however the general shape is similar. For example, the minimum potential reached by the model is between -75 to -80 mV, however *Lymnaea* ventricle cell rest potential is said to be on average -60 mV. Since the currents responsible

for dictating the resting potential are not directly modeled from *Lymnaea* data, the resting potential reflects those recorded in vertebrate cells. Guinea pig cardiac cell resting potentials are much more hyperpolarized than *Lymnaea* and are recorded at about -80 mV. To raise this potential to those seen in *Lymnaea*, further characterization of the delayed rectifier current is needed to set appropriate parameters to shift the resting potential.

The currents implemented in the Kyoto model were constructed from recordings of guinea pig cells. Currently there is no model available of the invertebrate cardiac action potential, and models for each current are taken from vertebrates. The models used for the model may not accurately represent the differences in modeling an invertebrate action potential through differences in voltage dependent rates and calcium dependent inactivation. Differences in the models may lead to changes in reported behaviour of currents in the action potential model. In order to properly reconstruct the invertebrate cardiac action potential, currents found in *Lymnaea stagnalis* ventricle cells must be recharacterized to include voltage dependent time constants and voltage dependent steady states for modeling each current's gates, as well as investigating L-type current calcium dependent inactivation kinetics.

The L-type current implemented in the Kyoto model was used to produce a simulated cardiac action potential that was only active for approximately 150 ms, however to replicate the results of Yeoman & Benjamin, 1999 the L-type needed to be active for 2-4 seconds. To extend the duration of the action potential using this model, the calcium dependent gate was omitted translating to reducing the rates of calcium binding to the gate to zero. This is not physiologically correct as voltage clamp experiments performed on ventricle cells by Yeoman et al., 1999 show calcium dependent inactivation when recording the L-type current in presence of calcium versus barium. To provide a better model for the L-type current, further experiments need to be performed to determine the kinetics of the calcium dependent inactivation gate.

Calcium dynamics of the model are presented in a general form omitting details of calcium uptake and release from the sarcoplasmic reticulum and calcium binding molecules.

These details may contribute to lengthening the plateau phase in the presence of calcium dependent inactivation by providing further currents causing calcium release after being triggered by currents on the cell membrane. Studies have not been performed on *Lymnaea stagnalis* regarding these processes of calcium dynamics and have been omitted from the model. Calcium dynamics instead have been adjusted to extend duration of the action potential by setting arbitrary rates of local calcium concentrations growing and decaying to produce a desired behaviour. Experiments to describe current density and calcium decay would provide insight into the proper rates that should be associated with the model.

The model only features the four currents described by Yeoman & Benjamin, 1999 and omits current models for ionic pumps, exchangers, and leak currents. The pump and exchanger models used in the full Kyoto model produce large currents relative to those of the model and would mask the behaviour of the currents of interest. No experiments have been performed to examine the presence of pumps or exchangers or their contribution to the action potential. To examine purely the behaviour of the four currents of interest, these details were omitted from the model. However a more accurate invertebrate model would require presence of such currents.

5 Conclusions

5.1 Future Directions and Proposed Experiments

Further experiments to provide more accurate representation of the currents found in *Lymnaea stagnalis* are necessary to provide a more accurate mathematical model. Currently, parameters for the delayed rectifier, A-type and L-type current are limited and not presented in a form enabling mathematical modeling. To provide a more accurate model of the invertebrate heart, voltage dependent time constant and steady state parameters need to be collected for these currents. These currents were shown to be isolated using blockers and subtraction techniques, and experiments may be performed again to provide these finer

details. A quantitative mathematical model using data directly from *Lymnaea* instead of qualitatively describing the currents from guinea pig models of the four currents described will provide a more accurate description of behaviour.

The results of the intended experiments will help dictate future directions to further examine the role of the 12a and 12b T-type current isoforms, and determine the reliability of the model. If spikes are still capable of generation in the absence of sodium, experiments using T-type current blockers such as yttrium (Yi^{3+}) can be used during microelectrode recordings to examine the pacemaking effects of blocking this current. It is expected to follow the results of the model where spiking is still capable but at a severely reduced rate without the T-type current.

Experiments on dissociated ventricle cells may be limited. The heart is a coordinated system because of the network of gap junctions allowing adjacent cells to stimulate activity. Dissociated cells lack this structure and behaviour of ventricle cells within this network may be different from what is observed in dissociated cells. Future work on semi intact or intact heart would provide the additional level of adding a network of cells connected via gap junctions. This would be expected to provide more accurate results and more closely resemble results in vivo because of the dependence of signals from neighbouring cells. Experiments may be performed in different locations of the heart to test for pacemaking ability based on region.

5.2 General Conclusions

Simulations of the two isoforms of the invertebrate T-type current display its role in the invertebrate heart. By simulating T-type and L-type current block, as well as altering the ionic concentrations of sodium and calcium, the T-type current was shown to be the prominent pacemaker in the invertebrate ventricular action potential as hypothesized. It was unclear whether the T-type current was responsible for carrying a sodium dependent upstroke, but this is hypothesized not to be the case based on simulations from the model. The T-type

current was shown to be responsible for initiating the upstroke but the upstroke was ultimately shown to be carried by the L-type calcium current. This follows the mechanism of the SA node action potential, despite it presenting in a ventricular cell. This illustrates the similar behaviour of pacemaking cells presented in contractile cells where the heart has no known localized region for pacemaking.

Results were not obtained for the majority of the electrophysiology recordings, but predictions of results and suggestions for improvement were provided. Action potential clamp records are expected to yield similar results to those of the model, and provide insight into the behaviour of the L-type current. This will assist in providing a more accurate L-type model to reflect calcium dependent and voltage dependent behaviour during the action potential. Microelectrode recordings of prostate and albumen cells are expected to display depolarizations associated with secretion and be heavily dependent on an L-type calcium current. It is also expected that the sodium and calcium permeable 12b T-type current is responsible for initiating the mechanism for secretion and possibly pacemaking activity. The modifications to the methods to provide more accessible cells and use sharp microelectrode recording tips for whole cell recording may provide more success for recording these cells in the future.

The results of the invertebrate T-type model provide hypotheses for the physiological role of the T-type family of channels, but much is still not known of the role in vertebrates. Additional complexities exist such as many more contributors to the pacemaker potential such as the "funny" current and sodium calcium exchanger, and the three T-type isoforms $Ca_v3.1$, $Ca_v3.2$ and $Ca_v3.3$ found in various tissues make identifying the vertebrate T-type physiological role more difficult. The invertebrate model acts as a general model to assist in understanding the T-type role to further drug development research to treat T-type related conditions such as epilepsy and arrhythmia. A known role of the T-type current will provide insight to guide further research for therapeutic treatment.

References

Ahir, B., & Pratten, M. (2014). Structure and function of gap junction proteins: Role of gap junction proteins in embryonic heart development. *The International Journal of Developmental Biology*, *58*, 649-662.

Bekius, R. (1971). The circulatory system of *Lymnaea stagnalis* (l.). *Netherlands Journal of Zoology*, *22*(1), 1-58.

Birkedal-Hansen, H., Moore, W. G. I., Bodden, M. K., Windsor, L. J., Birkedal-Hansen, B., DeCarlo, A., & Engler, J. A. (1993). Matrix metalloproteinases: A reivew. *Critical Reviews in Oral Biology and Medicine*, *4*(2), 187-250.

Bourne, G. B., Redmond, J. R., & Jorgensen, D. D. (1990). Dynamics of the molluscan circulatory system: Open versus closed. *Physiological Zoology*, *63*(1), 140-166.

Boyett, M. R. (2009). 'And the beat goes on' The cardiac conduction system: The wiring system of the heart. *Experimental Physiology*, *94*(10), 1035-1049.

Boyett, M. R., Honjo, H., Harrison, S. M., Zang, W.-J., & Kirby, M. S. (1994). Ultra-slow voltage-dependent inactivation of the in guinea-pig and ferret ventricular myocytes. *European Journal of Physiology*, *428*, 39-50.

Cheong, E., & Shin, H.-S. (2013). T-type Ca^{2+} channels in absence epilepsy. *Biochimica et Biophysica Acta (BBA) - Biomembranes*, *1828*(7), 1560-1571.

Dumaine, R., Towbin, J. A., Brugada, P., Vatta, M., Nesterenko, D. V., Nesterenko, V. V., ... Antzelevitch, C. (1999). Ionic mechanisms responsible for the electrocardiographic phenotype of the Brugada syndrome are temperature dependent. *Circulation Research*, *85*, 803-809.

Freshney, R. I. (2010). *Culture of animal cells* (6th ed.). John Wiley & Sons, Inc.

Gavaghan, M. (1998). Cardiac anatomy and physiology: A review. *AORN Journal*, *64*(4), 800-822.

Grant, A. O. (2009). Cardiac ion channels. *Circulation: Arrhythmia and Electrophysiology*, *2*, 185-194.

Hagiwara, N., Irisawa, H., & Kameyama, M. (1988). Contribution of two types of calcium currents to the pacemaker potentials of rabbit sino-atrial node cells. *Journal of Physiology*, *395*, 233-253.

Hille, B. (2001). Ion channels of excitable membranes. Sunderland, MA: Sinauer Associates.

Hodgkin, A. L., & Huxley, A. F. (1952). A quantitative description of membrane current and its application to conduction and excitation in nerve. *Journal of Physiology*, *117*, 500-544.

Kakei, M., Noma, A., & Shibasaki, T. (1985). Properties of adenosine-triphosphate-regulated potassium channels in guinea-pig ventricular cells. *Journal of Physiology*, *363*(1), 441-462.

Kiehn, L., Mukai, S. T., & Saleuddin, A. S. M. (2004). The role of calcium on protein secretion of the albumen gland in *Helisoma duryi Gastropoda*. *Invertebrate Biology*, *123*(4), 304-315.

Koene, J. (2006). Tales of two snails: sexual selection and sexual conflict in *Lymnaea stagnalis* and *Helix aspersa*. *Integrative and Comparative Biology*, *46*(4), 419-429.

Lambert, R. C., Bessaïh, T., Crunelli, V., & Leresche, N. (2014). The many faces of T-type calcium channels. *European Journal of Physiology*, *466*, 415-423.

Matsuoka, S., Sarai, N., Kuratomi, S., Ono, K., & Noma, A. (2003). Role of individual ion current systems in ventricular cells hypothesized by a model study. *Japanese Journal of Physiology*, *53*, 105-123.

McComb, C., Varshney, N., & Lukowiak, K. (2005). Juvenile *Lymnaea ventilate*, learn and remember differently than do adult *Lymnaea*. *Journal of Experimental Biology*, *208*(8), 1459–1467.

Misler, S. (2009). Unifying concepts in stimulus-secretion coupling in endocrine cells and some implications for therapeutics. *Advances in Physiology Education*, *33*(3), 175-186.

Monfredi, O., Dobrzynski, H., Mondal, T., Boyett, M. R., & Morris, G. M. (2010). The anatomy and physiology of the sinoatrial node - A contemporary review. *Pace*, *33*,

1392-1406.

Moreno, J. D., & Clancy, C. E. (2011). Heart rate and rhythm: Molecular basis, pharmacological modulation and clinical implications. In N. O. Tripathi, U. Ravens, & C. M. Sanguinetti (Eds.), (p. 175-194). Berlin, Heidelberg: Springer.

Nattel, S., & Carlsson, L. (2006). Innovative approaches to anti-arrhythmic drug therapy. *Nature Reviews Drug Discovery*, *5*, 1034-1049.

Noma, A., & Shibasaki, T. (1985). Membrane current through adenosine triphosphate regulated potassium channels in guinea pig ventricular cells. *The Journal of Physiology*, *363*(1), 463-480.

Ono, K., & Iijima, T. (2010). Cardiac T-type Ca^{2+} channels in the heart. *Journal of Molecular and Cellular Cardiology*, *48*, 65-70.

Ono, K., & Ito, H. (1995). Role of rapidly activating delayed rectifier K^+ current in sinoatrial node pacemaker activity. *American Journal of Physiology - Heart and Circulatory Physiology*, *269*(2), H453-H462.

Perez-Reyes, E. (2003). Molecular physiology of low-voltage-activated T-type calcium channels. *Physiology Reviews*, *83*, 117-161.

Senatore, A., Guan, W., Boone, A., & Spafford, J. D. (2014). T-type channels become highly permeable to sodium ions using an alternative extracellular turrent region (S5-P) outside the selectivity filter. *Journal of Biological Chemistry*, *289*(17), 11952–11969.

Senatore, A., Zhorov, B. S., & Spafford, J. D. (2012). Ca_v3 T-type calcium channels. *WIREs Membrane Transport and Signaling*, *1*, 467-491.

Shirokov, R., Levis, R., Shirokova, N., & Rios, E. (1993). Ca^{2+} dependent inactivation of L-Type Ca^{2+} channels does not affect their voltage sensor. *The Journal of General Physiology*, *102*(6), 1005-1030.

Spafford, J. D., Dunn, T., Smit, A., Syed, N., & Zamponi, G. (2006). In vitro characterization of L-type calcium channels and their contribution to firing behavior in invertebrate respiratory neurons. *Journal of Neurophysiology*, *95*(1), 45-52.

Syed, N. I., Ridgway, R. L., Lukowiak, K., & Bulloch, A. G. M. (1992). Transplantation and functional integration of an identified respiratory interneuron in *Lymnaea stagnalis. Neuron*, *8*(4), 767-774.

Vandemarliere, E., Mueller, M., & Martens, L. (2013). Getting intimate with trypsin, the leading protease in proteomics. *Mass Spectrometry Reviews*, *32*, 453-465.

Vassort, G., Talavera, K., & Alvarez, J. (2006). Role of T-typeCa^{2+} channels in the heart. *Cell Calcium*, *40*(2), 205 - 220.

Yeoman, M. S., & Benjamin, P. R. (1999). Two types of voltage gated K^+ currents in dissociated heart ventricular muscle cells of the snail *Lymnaea stagnalis*. *Journal of Neurophysiology*, *82*(5), 2415-2427.

Yeoman, M. S., Brezden, B. L., & Benjamin, P. R. (1999). LVA and HVA Ca^{2+} currents in ventricle muscle cells of the *Lymnaea* heart. *Journal of Neurophysiology*, *82*(5), 2428-2440.

A Appendix: Modeling Equations

A.1 List of Model Abbreviations

AI = probability of L-type channel being in state AI
AP = probability of L-type channel being in state AP
C = probability of L-type channel being in covered state
C_m = membrane capacitance (pF)
$[Ca]$ = local calcium concentration (mM)
CCa = probability of L-type channel being in calcium bound covered state
CF_x = constant field equation for ion X (mM)
F = Faraday's constant, 96.4867 (C mmol^{-1})
I_aX = ion X component of current I_a (nA)
I_{app} = applied current (nA)
I_{CaL} = L-type calcium current (nA)
$I_{CaT-12a}$ = 12a T-type current (nA)
$I_{CaT-12b}$ = 12b T-type current (nA)
I_{ion} = net ionic current (nA)
I_{Kr} = delayed rectifier current (nA)
I_{to} = transient outward current (nA)
P_x = convert factor of current x (nA mM^{-1})
$p(open)$ = probability of current being in an open state
R = ideal gas constant, 8.3134 (C mV K^{-1} mmol^{-1})
RI = probability of L-type channel being in state RI
RP = probability of L-type channel being in state RP
T = absolute temperature (K)
U = probability of L-type channel being in uncovered state
UCa = probability of L-type channel being in uncovered state
V_m = membrane potential (mV)
y_x = gating variable for gate with two state ($0 \leq y_x \leq 1$)
z_x = valence charge of ion X
$[X]_i$ = internal concentration of ion X (mM)
$[X]_o$ = external concentration of ion X (mM)
α_{y_x}, β_{y_x}, k_x = gating rate constants (ms^{-1})
α, β = rates of calcium dyanmics ($\frac{mM}{ms \cdot nA}$, ms^{-1})
$\tau_x(V_m)$ = voltage dependent time constant of current x (ms)
$y_\infty(V_m)$ = voltage dependent steady state of gate

A.2 Membrane Potential and Internal Ion Concentration Models

Membrane potential:

$$\frac{dV_m}{dt} = \frac{I_{app} - I_{ion}}{C_m}$$

$$I_{ion} = I_{Kr} + I_{to} + I_{CaL} + I_{CaT}$$

Dynamic local calcium concentration for 12a T-type model:

$$\frac{d[Ca]}{dt} = \alpha I_{CaL} - \beta([Ca] - [Ca]_i)$$

	α $(\frac{mM}{ms \cdot nA})$	β (ms^{-1})
CDI-free model	0.1	10
CDI model	0.05	10

Calcium constant field equation using local calcium concentration:

$$CF_{Ca}([Ca], V_m) = \frac{zFV_m}{RT} \frac{[Ca] - [Ca]_o \exp(\frac{-zFV_m}{RT})}{1 - \exp(\frac{-zFV_m}{RT})}$$

Constant field equation for sodium or potassium given by ion X:

$$CF_x(V_m) = \frac{zFV_m}{RT} \frac{[X]_i - [X]_o \exp(\frac{-zFV_m}{RT})}{1 - \exp(\frac{-zFV_m}{RT})}$$

A.3 Transient Outward Current Model

Current equation:

$$I_{to} = P_{to} C F_K y_1^3 y_2$$

General gating equations for all gates:

$$\frac{dy_i(t, V_m)}{dt} = \alpha_{y_i}(V_m)(1 - y_i(t, V_m)) - \beta_{y_i}(V_m) y_i(t, V_m)$$

Voltage dependent rates:

$$\begin{aligned}
\alpha_{y_1} &= \frac{1}{11 \exp\left(\frac{-V_m}{28}\right) + 0.2 \exp\left(\frac{-V_m}{400}\right)} \\
\beta_{y_1} &= \frac{1}{4.4 \exp\left(\frac{V_m}{16}\right) + 0.2 \exp\left(\frac{V_m}{500}\right)} \\
\alpha_{y_2} &= \frac{0.0038 \exp\left(-\frac{V_m + 13.5}{11.3}\right)}{1 + 0.051335 \exp\left(-\frac{V_m + 13.5}{11.3}\right)} \\
\beta_{y_2} &= \frac{0.0038 \exp\left(\frac{V_m + 13.5}{11.3}\right)}{1 + 0.067083 \exp\left(\frac{V_m + 13.5}{11.3}\right)}
\end{aligned}$$

A.4 Delayed Rectifier Current Model

Current equation:

$$I_{Kr} = P_{Kr} CF_K (0.6y_1 + 0.4y_2) y_3$$

General gating equations for all gates:

$$\frac{dy_i(t, V_m)}{dt} = \alpha_{y_i}(V_m)(1 - y_i(t, V_m)) - \beta_{y_i}(V_m) y_i(t, V_m)$$

Voltage dependent rates:

$$\begin{aligned}
\alpha_{y_1} &= \frac{1}{20\exp\left(-\frac{V_m}{11.5}\right) + 5\exp\left(-\frac{V_m}{300}\right)} \\
\beta_{y_1} &= \frac{1}{160\exp\left(\frac{V_m}{28}\right) + 200\exp\left(\frac{V_m}{1000}\right)} + \frac{1}{2500\exp\left(\frac{V_m}{20}\right)} \\
\alpha_{y_2} &= \frac{1}{200\exp\left(-\frac{V_m}{13}\right) + 20\exp\left(-\frac{V_m}{300}\right)} \\
\beta_{y_2} &= \frac{1}{1600\exp\left(\frac{V_m}{28}\right) + 2000\exp\left(\frac{V_m}{1000}\right)} + \frac{1}{10000\exp\left(\frac{V_m}{20}\right)} \\
\alpha_{y_3} &= \frac{1}{10\exp\left(\frac{V_m}{17}\right) + 2.5\exp\left(\frac{V_m}{300}\right)} \\
\alpha_{y_3} &= \frac{1}{0.35\exp\left(-\frac{V_m}{17}\right) + 2\exp\left(\frac{V_m}{150}\right)}
\end{aligned}$$

A.5 L-Type Current Model

CDI Current equation:

$$I_{CaL} = P_{CaL} CF_{Ca} AP(U + UCa)y$$

CDI-Free Current equation:

$$I_{CaL} = P_{CaL} CF_{Ca} AP \cdot y$$

Voltage dependent gating equations:

$$\begin{aligned}
\frac{dAP}{dt} &= k_{AI,AP} AI + k_{RP,AP} RP - (k_{AP,AI} + k_{AP,RP}) AP \\
\frac{dAI}{dt} &= k_{AP,AI} AP + k_{RI,AI} RI - (k_{AI,RI} + k_{AI,AP}) AI \\
\frac{dRP}{dt} &= k_{AP,RP} AP + k_{RI,RP} RI - (k_{RP,RI} + k_{RP,AP}) RP \\
RI &= 1 - AP - AI - RP
\end{aligned}$$

Calcium dependent gating equations:

$$\begin{aligned}
\frac{dU}{dt} &= k_{C,U} C + k_{UCa,U} UCa - (k_{U,C} + k_{U,UCa}) U \\
\frac{dCCa}{dt} &= k_{C,CCa} CCa + k_{UCa,CCa} UCa - (k_{CCa,C} + k_{CCa,UCa}) CCa \\
\frac{dUCa}{dt} &= k_{U,UCa} U + k_{CCa,UCa} CCa - (k_{UCa,U} + k_{UCa,CCa}) UCa \\
C &= 1 - U - UCa - CCa
\end{aligned}$$

Ultra slow gating equations:

$$\frac{dy(t, V_m)}{dt} = \alpha_y(V_m)(1 - y(t, V_m)) - \beta_y(V_m) y(t, V_m)$$

Voltage dependent gate rates:

Rates were modified by shifting the voltage by -20 mV in $k_{RP,AP}$ and $k_{AP,RP}$ to resembled the L-type current described by Senatore et al. in their voltage ramp experiments.

$$
\begin{aligned}
k_{AI,AP} &= 0.001 \\
k_{AP,AI} &= 0.004 \\
k_{RP,AP} &= \frac{1}{0.27\exp(\frac{-(V_m+20)}{5.9}) + 1.5\exp(\frac{-(V_m+20)}{65})} \\
k_{AP,RP} &= \frac{1}{480\exp(\frac{V_m+20)}{7}) + 2.2\exp(\frac{V_m+20}{65})} \\
k_{RI,AI} &= \frac{1}{0.0018\exp(\frac{-V_m}{7.4}) + 11\exp(\frac{-V_m}{100})} \\
k_{AI,RI} &= \frac{1}{2200000\exp(\frac{V_m}{7.4}) + 11\exp(\frac{V_m}{100})} \\
k_{RP,RI} &= 0.04/(1 + k_{AI,AP}k_{RI,AI}k_{AP,RP}/k_{AP,AI}/k_{RP,AP}/k_{AI,RI}) \\
k_{RI,RP} &= 0.04 - k_{RP,RI}
\end{aligned}
$$

Calcium dependent gate rates: Rates $k_{CCa,UCa}$ and $k_{UCa,CCa}$ are adjusted by factors of 30 and 0.01 respectively to slow calcium dependent inactivation.

$$
\begin{aligned}
k_{C,U} &= 0.143 \\
k_{U,C} &= 0.35 \\
k_{CCa,UCa} &= 30 \cdot 0.0003 \\
k_{UCa,CCa} &= 0.01 \cdot 0.35 \\
k_{C,\bar{C}Ca} &= 6.954 \\
k_{CCa,C} &= 0.0042 \\
k_{U,\bar{U}Ca} &= k_{C,\bar{C}Ca} \\
k_{UCa,U} &= k_{CCa,C}k_{UCa,CCa}/k_{U,C}/k_{CCa,UCa} \\
k_{U,UCa} &= k_{U,\bar{U}Ca}([Ca]AP + [Ca](1 - AP))U \\
k_{C,CCa} &= k_{C,\bar{C}Ca}C[Ca]AP
\end{aligned}
$$

Ultra slow gate rates:

$$\alpha_y = \frac{1}{250000\exp(\frac{V_m}{9}) + 58\exp(\frac{V_m}{65})}$$
$$\beta_y = \frac{1}{1800\exp(\frac{-V_m}{14}) + 66\exp(\frac{-V_m}{65})}$$

A.6 T-Type Current Model

A.6.1 12a T-Type Model

Current equation:

$$I_{CaT-12a} = P_{CaT-12a} CF_{Na} y_{1,12a} y_{2,12a}$$

General gating equations for all gates:

$$\frac{dy_i(t,V_m)}{dt} = \alpha_{y_i}(V_m)(1 - y_i(t,V_m)) - \beta_{y_i}(V_m) y_i(t,V_m)$$

Voltage dependent steady state and time constants:

$$y_{1,12a,\infty} = \frac{1}{1 + \exp(\frac{-(-53.63-V_m)}{5.60})}$$
$$y_{2,12a,\infty} = \frac{1}{1 + \exp(\frac{-(-70.21-V_m)}{2.73})}$$
$$\tau_{y_{1,12a}} = 0.1194\exp\left(\frac{-V_m}{15.2577}\right) + 0.3453$$
$$\tau_{y_{2,12a}} = 0.0154\exp\left(\frac{-V_m}{7.6448}\right) + 17.4009$$

A.6.2 12b T-type Model

Current equation:

$$I_{CaT-12a} = I_{CaT_1 2b} Na + I_{CaT-12b} Ca$$

$$I_{CaT-12a} = 0.5 P_{CaT-12b} CF_{Na} y_{1,12b} y_{2,12b} + 0.5 P_{CaT-12b} CF_{Ca} y_{1,12b} y_{2,12b}$$

General gating equations for all gates:

$$\frac{dy_i(t, V_m)}{dt} = \alpha_{y_i}(V_m)(1 - y_i(t, V_m)) - \beta_{y_i}(V_m) y_i(t, V_m)$$

Voltage dependent steady state and time constants:

$$y_{1,12b,\infty} = \frac{1}{1 + \exp(\frac{-(-53.48 - V_m)}{5.46})}$$

$$y_{2,12b,\infty} = \frac{1}{1 + \exp(\frac{-(-70.89 - V_m)}{2.93})}$$

$$\tau_{y_{1,12b}} = 0.8162 \exp\left(\frac{-V_m}{31.3185}\right) + 0.3865$$

$$\tau_{y_{2,12b}} = 0.03686 \exp\left(\frac{-V_m}{8.5179}\right) + 15.98$$

B Appendix: Electrophysiology Methods

To investigate the physiological role of T-type channels on the action potential, laboratory were performed on *Lymnaea stagnalis* ventricle, prostate, and albumen cells. The next three sections describe the methods used to dissociate cells and perform electrophysiological recordings to study both action potentials and their underlying currents.

B.1 Cell Culture

B.1.1 Organ Dissection

A colony of the pond snail *Lymnaea stagnalis* is maintained in the aquatic facility in room B1-177 at University of Waterloo where they are exposed to a 12 hour light/12 hour dark cycle. Juvenile and adult snails are primarily fed organic lettuce grown from seed in the University of Waterloo greenhouse with fish food pellets as a supplement, while new hatchlings are fed primarily spirulina flakes. Conductivity and pH is maintained by an automated YSI 5200 system which regularly doses the feeding tank to have a pH of 7.3 using sodium bicarbonate and conductivity of 500 μS using seasalt.

Snails are bred in their tanks to maintain the population. Once egg sacs are laid, the adult snails are removed from the tank to maximize the likelihood of hatchling survival. Young snails are reintroduced to adult snails once shell length reaches 1-1.5 cm. At this point, snails are considered juveniles (McComb, Varshney, & Lukowiak, 2005). The population was supplemented by a donation of snails from Dr. Petra Hermann of University of Calgary.

Adult snails with a shell length of at least 20 millimeters were chosen for dissection to ensure sexual maturity as this is the approximate shell length of adult snails (McComb et al., 2005). A solution of 10% Listerine and tank water was used to anesthetize snails for ten minutes. Once anesthetized, the shells were carefully removed with Vannas spring scissors. Deshelled snails were placed in a dissection dish with 10% Listerine and tank water solution to keep the animal unconscious and hydrated during the dissection under a Carl Zeiss SteREO

Discovery V8 microscope. The two tentacles at the head were pinned down, and an incision was made down the head to expose the internal male sexual organs for prostate removal (Figures B.1a and B.1b). The albumen gland is located posterior to the prostate (Figures B.1c and B.1d). In adult snails, it can be recognized by its orange colour and wedge shape. In juvenile snails (shell length of less than two centimeters), the albumen gland is grey in appearance. The two chambered heart is located to the left of the prostate and must be recovered from under the kidney (Figures B.1e and B.1f). The heart was carefully dissected to avoid puncturing the kidney, and the atrium and ventricle were separated. The organs were separated into separate dissection dishes and placed in 0.5 mM Ca^{2+} Leibowitz solution where they were cut up into approximately 1 mm pieces for cell dissociation.

B.1.2 Cell Dissociation

Trypsin and collagenase are two enzymes commonly used in tissue dissociation for cell culture to break down proteins of the extracellular matrix and separate individual cells (Freshney, 2010). Trypsin is naturally a digestive protease of the digestive tract used to break down dietary proteins into peptides, but is widely used in cell culture to break down nonspecific proteins of the extracellular matrix (Vandemarliere, Mueller, & Martens, 2013). It acts by cleaving the carboxy-terminal between arginine and lysine breaking down these different proteins into smaller fragments disrupting their structural function (Vandemarliere et al., 2013). To prevent residual enzymatic activity once trypsin has been used, an inhibitor extracted from soybeans (Sigma-Aldrich trypsin inhibitor from *Glycine max* (soybean)) may be used. 1 mg of inhibitor will act on 1-3 mg of trypsin by binding to the active site at an optimal pH of 8, where the snail culture medium is at pH of 7.8.

Collagenase is a metalloprotease which acts specifically on the structural protein collagen of the extracellular matrix (Birkedal-Hansen et al., 1993). Metalloproteases require a metal such as Ca^{+2} or Zn^{2+} for activation (Birkedal-Hansen et al., 1993), therefore collagenase was prepared and stored frozen in a balanced salt solution without calcium and the pH was

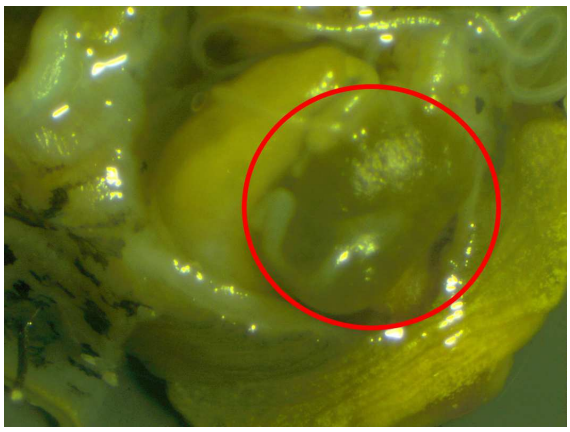

(a) *Lymnaea stagnalis* prostate within the animal (red circle).

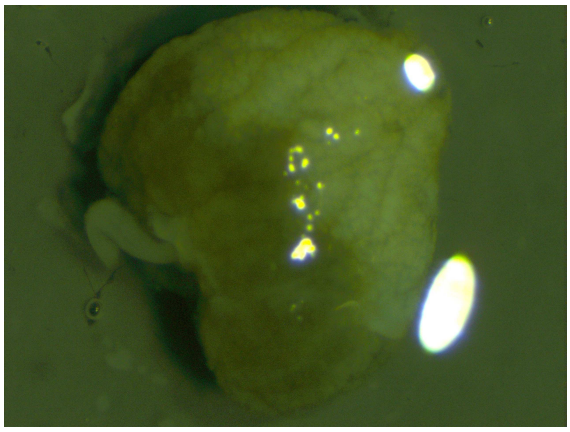

(b) *Lymnaea stagnalis* prostate dissected from the animal.

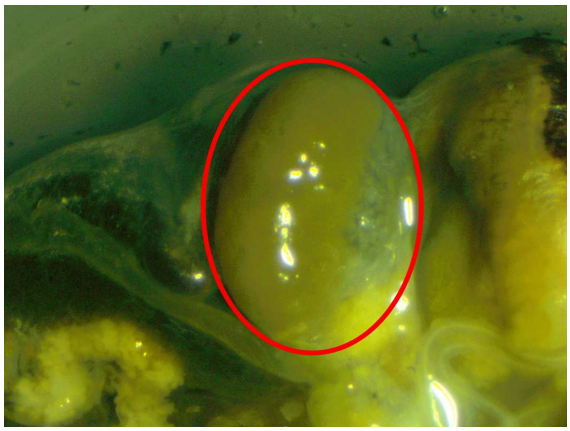

(c) *Lymnaea stagnalis* albumen gland within the specimen (red circle).

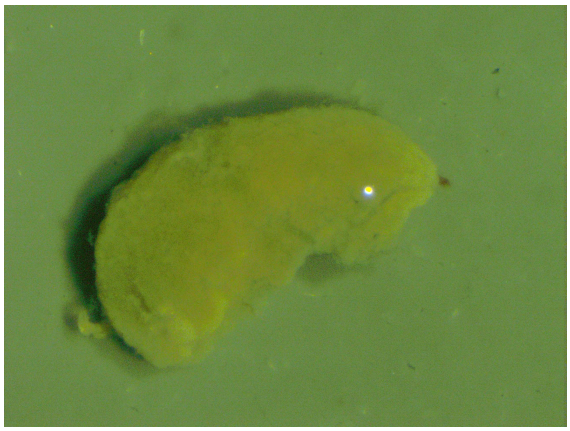

(d) *Lymnaea stagnalis* albumen dissected from the specimen.

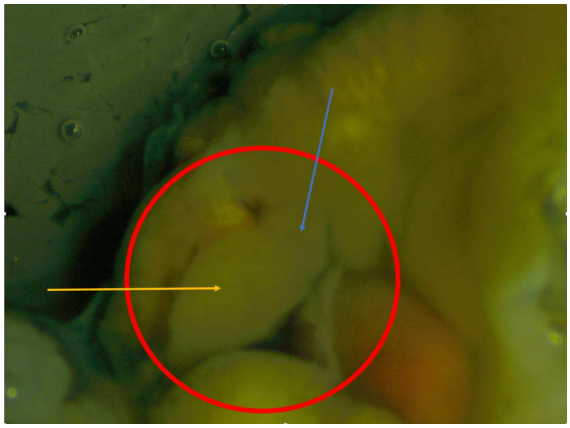

(e) *Lymnaea stagnalis* heart within the specimen (red circle). The yellow arrow points to the larger ventricle, the blue arrow points to the smaller and translucent atrium.

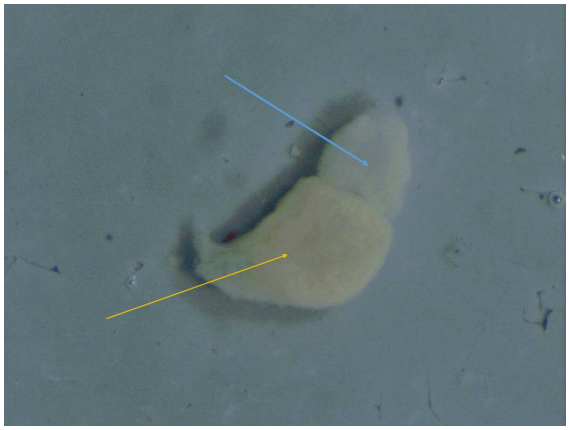

(f) *Lymnaea stagnalis* heart dissected from the specimen. Yellow arrow points to the ventricle, and blue arrow points to the atrium.

Figure B.1: *Lymnaea stagnalis* prostate, albumen gland, and heart within the animal and dissected out of the animal. Pictures were taken using a Carl Zeiss SteREO Discovery V8 microscope with an Axiocam 105 and ZenLite software.

adjusted to 7.9 using 3% v/v HCl or 30% w/v NaOH. Introduction to a culture medium containing Ca^{2+} is necessary for collagenase to both become activated and bind to collagen for cleavage (Birkedal-Hansen et al., 1993). To promote adhesion of cells to a culture flask or glass cover slip, several washes must be performed to remove all residual collagenase. Any remaining collagenase may continue to break down collagen secreted by the cell (Freshney, 2010).

Dissociation of prostate, albumen, and ventricle cells were carried out in a custom Leibowitz media designed for *Lymnaea stagnalis* (Gibco, Formula No. 82-5154EB) containing ingredients to promote cell culture such as vitamins, amino acids, and pH indicator phenol red but without inorganic salts . The Leibowitz media used for *Lymnaea* cell culture contains the custom package for cell culture, and added 0.9837 mM $MgCl_2$, 0.8114 mM $MgSO_4$, 5.364 mM KCl, 0.44 mM KH_2PO_4, 136.77 mM NaCl, 1.338 mM Na_2HPO_4, 2mM L-glutamine, and 30 mM glucose. Separate preparations were made for 0.5 mM Ca^{2+} and 3.5 mM Ca^{2+} Leibowitz media. The final culture media contained Leibowitz medium with 3.5 mM Ca^{2+}, 2% fetal bovine serum, and $500\frac{\mu g}{mL}$ of gentamicin.

Prostate and albumen cells were dissociated from primary tissue following the protocol for ventricle dissociation from Senatore et al. (2014). 1 mm pieces of the cut up tissue were placed in 0.5 mM Ca^{2+} Leibowitz medium with 0.25% fresh trypsin for 12 minutes on a rocking platform. The trypsin was inhibited with an equalmolar amount of trypsin inhibitor, then the suspension was centrifuged at 500 RCF for three minutes. The supernatant was discarded and replaced with 0.5 mM Ca^{2+} treated with 0.01% type I collagenase for 30 minutes on a rocking platform. The suspension was centrifuged at 500 RCF for three minutes, the supernatant discarded and replaced with 3.5 mM Ca^{2+} Leibowitz medium. This process was repeated two more times. The final media for cell culture was in 3.5 mM Ca^{2+} containing 2% fetal bovine serum and $500\frac{\mu g}{mL}$ gentamicin for up to five days.

Lymnaea stagnalis ventricle cells were cultured following the protocol from Yeoman & Benjamin, 1999. The ventricle was cut into small pieces of roughly 1 mm. 0.25% trypsin was

added fresh to 0.5 mM Ca^{2+} Leibowitz medium and digested for 20 minutes on a rocking platform. The trypsin was inhibited with an equal amount of trypsin inhibitor, then the suspension was centrifuged at 500 RCF for three minutes and the supernatant was removed. The cells were then treated with 0.01% collagenase in 0.5 mM Ca^{2+} Leibowitz medium for 75 minutes on a rocking platform. The suspension was centrifuged again at 500 RCF for 3 minutes, the supernatant was removed and replaced with 3.5 mM Ca^{2+} Leibowitz medium containing $500\frac{\mu g}{mL}$ gentamicin and 2% fetal bovine serum. The cells were centrifuged and the same media was replaced two more times. The cells were then plated on acid etched coverslips and left to adhere for 24 hours.

B.1.3 Cell Plating and Embedding

Prostate, albumen and ventricle cells were tested for adherence to circular glass coverslips of various coatings. Coverslips were treated with coatings such as poly-L-lysine, collagen, and acid to provide different methods to promote cell adherence. Prostate and albumen cells were also embedded in agarose gel as described in (Yeoman & Benjamin, 1999).

Poly-L-lysine coverslips were previously prepared in the lab from stock poly-L-lysine solution and diluted to 0.01% w/v with sterilized water. Coverslips were sterilized in 100% ethanol and dried before coating. In a sterile 60 mm petri dish, the coverslips were placed in a single layer covering the surface of the dish and a layer of 0.01% poly-L-lysine was added such that the surface of each coverslip was submerged in solution. The dish was left at room temperature for 30 minutes before being washed three times with sterile water. After the final wash, the water was removed by suction and the dish was placed in the oven to dry for one hour. When not in use, the dishes containing coverslips were covered in parafilm and stored in the refrigerator.

Circular glass coverslips were also coated with type I collagen from rat tail (Sigma Aldrich). Sterilized coverslips were placed in a single layer in a sterile 60 mm petri dish. The stock collagen solution was diluted to 0.01% w/v with sterile water and added to the petri

dish until coverslips were submerged in solution. The dishes were covered in parafilm and left overnight in a refrigerator to allow collagen to bind to the glass surface. The excess fluid was then removed and the dishes were allowed to dry in the refrigerator overnight. Dishes were then covered with parafilm and stored in the refrigerator until needed.

Ventricle cells were previously found to be adherent to acid etched coverslips (Senatore et al., 2014). Coverslips were prepared using 3% HCl and 0.1% Na_2CO_3. Glass coverslips were placed side by side in 60 mm petri dishes such that none overlapped. 6 mL of 3% HCl was added to the dish and left for 30 minutes. The acid was removed and three washes were performed with sterile water. 6 mL of 0.1% Na_2CO_3 was added to the dish and left for 30 minutes. The coverslips were washed five times with sterile water, then left in the oven to dry for at least 1.5 hours. When not in use, the coverslips were covered with parafilm and stored in a refrigerator.

Cell suspensions of prostate or albumen cells were embedded in agarose gel to provide structural support. Various concentrations of low melting point agarose (Biobasic) of 0.6%, 0.7%, and 0.8% w/v were tested in varying volumes of solution placed in a 35 mm petri dish to provide the best scaffold for cells. A solution of agarose was heated to 65°C to allow agarose to melt. Once melted, the solution was cooled to 45°C, just above its gelling point to prevent cell death from heat. 1.5 mL of cell suspension in 2x saline solution was combined with an equal volume of agarose solution then left to cool until the gel had solidified. Cells had fallen to the bottom of the gel once cooled. The gel can be inverted once solid to allow access to cells at the surface.

B.2 Microelectrode Recording

B.2.1 External Recording Solutions

Sharp microelectrode recording was performed to measure the native resting membrane potential without an imposed stimulus and observe the voltage fluctuations in prostate, albumen, and ventricle cells when an injected current was applied to stimulate the cell.

Table 5: Concentration changes in sodium used in varying sodium salines. Reduced sodium was replaced with NMDG. Concentrations of other salts remain the same.

Percent Sodium	[NaCl] (mM)	[NMDG] (mM)
100	50	0
75	37.5	12.5
50	25	25
25	12.5	37.5
0	0	50

Table 6: Concentration changes in calcium used in varying calcium salines. Concentrations of other salts remain the same.

Percent Calcium	[$CaCl_2$] (mM)
100	3.5
75	2.625
50	1.75
25	0.875
0	0

External recording solutions were prepared to perform recordings in physiological saline and various conditions of varying sodium concentration and calcium concentration. The pH was adjusted to 7.8 using NaOH in all saline preparations. The physiological saline solution was taken from (Yeoman & Benjamin, 1999) consisting of 50 mM NaCl, 1.7 mM KCl, 3.5 mM $CaCl_2$, 4 mM $MgCl_2$, and 10 mM HEPES.

Saline solutions were prepared with varying concentrations of sodium and calcium to explore ionic dependence in microelectrode recordings. Solutions containing 75%, 50%, 25% and 0% sodium were prepared by replacing NaCl with equimolar N-methyl-d-glucamine (NMDG), an impermeant monovalent ion. Concentrations are provided in Table 5. Solutions containing 75%, 50%, 25% and 0% calcium were prepared by removing $CaCl_2$ from the solution. Concentrations are provided in Table 6.

B.2.2 Current Clamp Recording

Sharp microelectrodes were pulled from borosilicate glass pipettes with 1.5 mm outer diameter and 0.86mm inner diameter using a Sutter P-97 pipette puller with a 2.5x2.5 mm

platinum box filament. Pipettes were pulled for a resistance of 20-50 MΩ and filled with 3 M KCl. A Ag/AgCl reference cell (World Precision Instruments) was used as the ground electrode. Data was collected by using pClamp 10 software on a PC computer to control an Axoclamp 900A amplifier (Molecular Devices) sampling through a Digidata1440a A/D converter (Molecular Devices). Cells were recorded by current clamp such that the injected current was 0 nA.

Cells are recorded once adhered to coverslips or embedded in agarose gel to provide structural support. To perform sharp microelectrode recording, the tip of the pipette is brought near the surface of the cell until it just touches the membrane. The tip is able to break through the membrane by adding mechanical pressure and piercing through, or buzzing the tip causing vibration to break through.

Protocols were performed with no injected current to record voltage fluctuations without current stimulus to test for spontaneous electrical activity. Current could also be injected to depolarize or hyperpolarize the cell and record cell electrical activity during these various electrical stimuli. Protocols were created using pClamp 10 software.

B.3 Whole Cell Voltage Clamp

B.3.1 Recording Solutions

External and internal solutions for whole cell recording differ from solutions used in sharp microelectrode recording. The external solution contained tetraethylammonium (TEA) to block potassium currents and consisted of 2 mM $BaCl_2$, 100 mM NaCl, 50 mM TEA-Cl, 1 mM $MgCl_2$, and 10 mM HEPES with pH adjusted to 7.8 using TEA-OH taken from Senatore et al., 2014. Internal solutions contained 135 mM CsCl, 5 mM 4-AP, 2 mM Mg-ATP, and 10 mM HEPES taken from Senatore et al., 2014.

B.3.2 Voltage Clamp and Action Potential Clamp Recording

Borosilicate glass pipettes with 1.5 mm outer diameter and 0.86 mm inner diameter were pulled with a Sutter P-1000 pipetter puller using a trough filament and fire polished using a MicroForge-830 to provide a resistance of 2-4 MΩ. Data was recorded using pClamp 10 software controlling a Multiclamp 700B sampling through a Digidata 1440A A/D converter.

Voltage clamp recordings are performed by bringing the tip of the pipette near the cell membrane, then applying suction to create a tight seal between the membrane and pipette tip. Once a seal is established by resistance reading in the GΩ range, the membrane may be broken by further suction or zapping the membrane. The internal solution within the pipette and intracellular solution become one continuous solution. The membrane potential is then able to be controlled or "clamped." Since the membrane potential is fixed, fluctuations in current are recorded to various changes in voltage.

Voltage clamp recordings feature voltage stimuli such as voltage steps involving an instantaneous step in voltage, or a voltage ramp where the voltage linearly increases in time. Action potential clamp may also be performed in whole cell recording. A stimulus waveform in the shape of an action potential may be used to identify currents activated during an action potential.

C Appendix: Electrophysiology Results and Discussion

C.1 Cell Culture

Dissociated prostate and albumen cells appear very similar in morphology (Figures C.1a and C.1b). Both are large, spherical cells containing large numbers of secretory vesicles. This is expected as albumen gland cells are responsible for secretion of nutrients for developing embryos in molluscs (Kiehn, Mukai, & Saleuddin, 2004), and prostate cells are responsible for secreting seminal fluid for male pattern mating behaviour (Koene, 2006).

Prostate and albumen cells were tested for adherence on various coated glass coverslips. Glass coverslips were prepared with 0.01% collagen coating, acid etched coating, and poly-L-lysine coating separately. Only collagen coated coverslips provide slight adherence for cells when transporting the coverslip from culture media to recording media. However because of the spherical shape of the cells, there is a lack of contact between the cell membrane and coated glass coverslip that does not allow enough adherence to support the mechanical stress of microelectrode recording. Although not ideal, cells are still capable of whole cell voltage clamp recording in solution without adherence to coverslips by applying suction to the cells to draw them near the pipette.

Prostate and albumen cells were also embedded in agarose gel to provide structural support for sharp microelectrode recording. Cells were provided adequate structural support without loss of viability compared to cells used on coated coverslips in culture media. Unfortunately cells were not accessible at the surface of the gel when the dish was inverted and therefore not accessible for recording. Cells that need to be reached by penetrating the gel were likely clogged by agarose gel at the tip of the pipette preventing microelectrode recordings. Recordings of cells below the surface of the gel showed no change in voltage when expected to fall to the cell's resting potential of approximately -40 to -60 mV when the cell was penetrated.

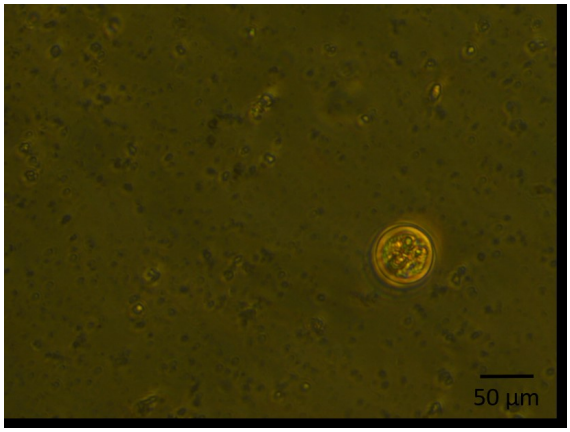

(a) *Lymnaea stagnalis* cultured albumen cells.

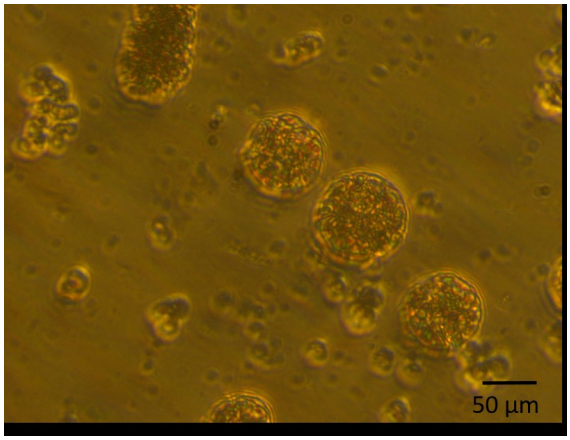

(b) *Lymnaea stagnalis* cultured prostate cells.

(c) *Lymnaea stagnalis* cultured ventricle muscle cell in a relaxed state.

(d) *Lymnaea stagnalis* cultured ventricle muscle cell in a contracted state.

Figure C.1: Cultured prostate, albumen and ventricle muscle cell of *Lymnaea stagnalis* in a relaxed state and contracted state. Ventricle cells are typically 40-120 μm long and 10-20 μm wide (Yeoman & Benjamin, 1999) when relaxed. Pictures were taken with a Zeiss Axiovert microscope using an Axiocam 105 and ZenLite software.

Ventricle cells were successfully dissociated and adhered to acid etched coverslips for recordings. Healthy cells could be visualized by their ability to spontaneously contract on the coverslip (Figure C.1c and C.1d).

C.2 Electrophysiology Results

Sharp microelectrode recordings of ventricle cells were obtained for physiological saline conditions. Action potentials recorded were consistent with what was described by Yeoman & Benjamin, 1999 in terms of being highly variable in shape. The resting membrane potential of recordings was -40 mV, but spike peak amplitudes were only about a maximum of 10 mV. The small waves may be action potentials with lower amplitude due to inactivated channels at this higher potential, or subthreshold voltage fluctuations (Figure C.2). The "action potentials" that were recorded were consistent with descriptions from Yeoman & Benjamin, 1999. Some spikes generated appeared similar in shape to a spike-plateau action potential with a broad plateau phase (Figure C.2a) while others resembled a fast spike shape (Figure C.2b). Both recordings of Figure C.2 were performed on the same cell, supporting that these cells are capable of firing both types of spikes.

Both spike-plateau and fast spike action potentials were variable in shape, duration, and rhythmicity. Voltage traces of microelectrode recordings were examined with Clampfit software where a set of cursors could be moved by the user to approximate the duration of spikes and time between spikes. Times are approximated to ± 0.5 ms. Spike-plateau action potentials were categorized as having a period of little voltage change causing a shoulder in the spike shape, where fast spike action potentials were categorized by their rapid upstroke and immediate repolarization (Figure C.2). These appeared to be the only two general spike shapes observed. Spikes tended to fire in close succession and feature the same shape during bursting activity; 2-5 spikes per burst of either spike-plateau or fast spike shapes would tend to fire with at least 3-4 seconds between the next burst of spikes with variable time in between individual spikes. Between these groups of consecutive spikes, the shape of the

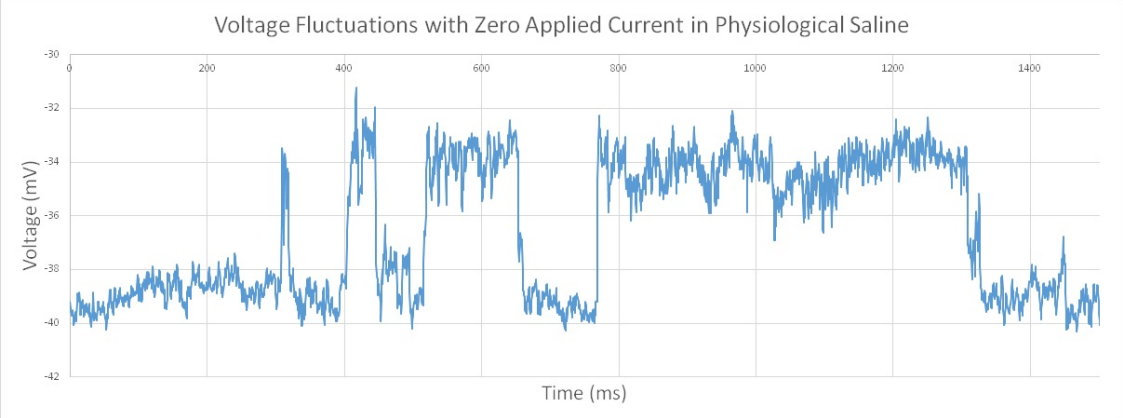

(a) Voltage fluctuations in ventricle cells resembling spike-plateau action potential shapes.

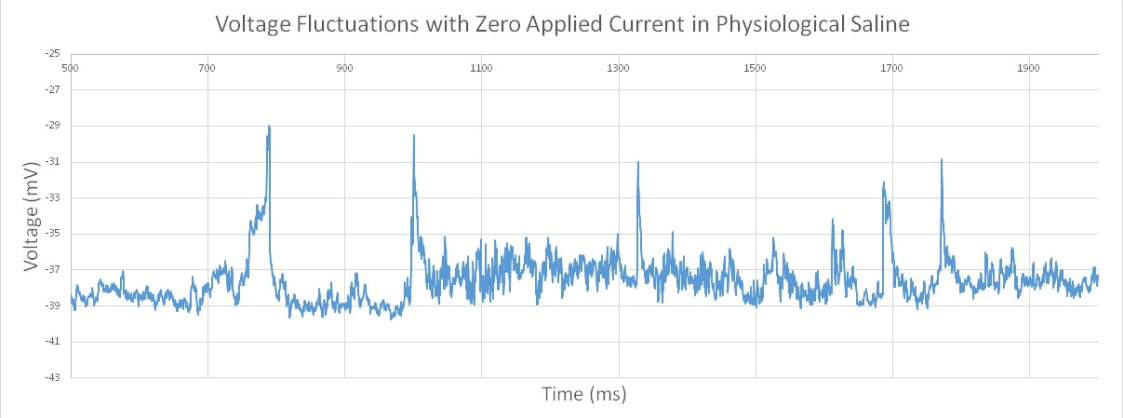

(b) Voltage fluctuations in ventricle cells resembling fast spike action potential shapes.

Figure C.2: Microelectrode recordings of ventricle cells in physiological saline show two types of action potentials in the same cultured ventricle cell from the snail *Lymnaea stagnalis*. (Top) The spikes generated feature a period of depolarization similar to a plateau phase. These resemble spike-plateau action potentials of the mammalian ventricle action potential. (Bottom) The spikes generated show a fast spike shape with immediate repolarization and lack the plateau phase.

observed spikes could potentially change. Spike-plateau and fast spike shapes appeared sporadic and without rhythmicity, such that spike-plateau action potentials ranged from 17.5 to 278.5 ms between individual spikes and fast spikes ranged from 4.5 to 910.0 ms between individual spikes. Spike duration was also variable, especially for spike-plateau action potentials. Fast spikes ranged in duration from 7.0 to 47.0 ms with the majority of spikes between 15.0 to 30.0 ms. Spike-plateau action potential duration ranged from 17.5 to 537.5 ms; spikes tended to increase in duration after each consecutive spike within a burst. Approximately equal numbers of fast spike and spike-plateau action potentials were observed.

Recordings of ventricle cells in various ionic concentrations were not obtained due to unhealthy cells. Ventricle cells displayed permanent contraction after 24 hours, potentially in the state of rigor mortis. Cells in this contracted state did not resemble healthy cells, nor did they provide recordings of action potentials.

Action potential clamp recordings of ventricle cells were not recorded. Ventricle cells contain large numbers of invaginations (Yeoman & Benjamin, 1999) providing uneven surfaces making patch clamp recording difficult. Due to the uneven surface and relatively large pipette tip, a seal on the surface of the membrane was not able to form for recordings.

Whole cell patch clamp recordings were not obtained from prostate or albumen cells. Since the cells are packed with vesicles, it is likely that they cause the membrane to become uneven. Forming seals onto the membrane was likely difficult due to this. When seals were able to form, breaking through the cell provided no recordings likely from the tip clogging with vesicles as the solutions of the pipette and internal cell environment become continuous.

Sharp microelectrode recordings of prostate and albumen cells were unsuccessful. Cells lacked sufficient adherence to coated coverslips, causing them to detach and move away from the pipette tip when attempting to pierce the membrane. Cells embedded in agarose gel had proper structural support to withstand the mechanical pressure applied to pierce the membrane, however cells were not available at the surface of the gel. Cells that required recording below the gel caused the pipette tip to become blocked by gel and prevent recording of the

intracellular solution.

C.3 Prediction of Electrophysiology Results

Recordings of ventricle cells in presence of blockers or reducing ionic concentrations, action potential clamp of ventricle cells, microelectrode recording of prostate and albumen gland cells, and voltage clamp recordings of prostate and albumen cells were not obtained, however predictions can be made of expected results based on the results of the model.

Microelectrode recording dissociated ventricle cells provided some recordings in physiological saline but were limited. With a more complete collection of recordings, the average resting membrane potential is expected to drop to a potential closer to those previously recorded for *Lymnaea stagnalis*, near -60 mV (Yeoman & Benjamin, 1999). Spikes would be expected to resemble those described by Yeoman & Benjamin, 1999 and vary considerably in shape since they are dissociated cells. Recordings performed on intact heart would be expected to have a more consistent shape due to the signals from gap junctions within the motor unit.

Reducing sodium and calcium concentrations to the same levels used in the model simulations would be expected to provide similar results as the model cell. Yeoman & Benjamin, 1999 showed that rebound spikes were still possible when no sodium was present, and lack of sodium would be expected to lower the rate of spike generation in the cell. The L-type current would still be expected to be able to carry the action potential and cause spiking activity during either a rebound spike or with an applied current to raise the potential to L-type activation. The L-type current of the model contributed to the pacemaker potential, however the L-type current of *Lymnaea stangalis* may not be active at the resting potential. Recordings in reduced sodium would be expected to cause spikes to become more infrequent, but may not impede spiking behaviour.

Reducing calcium concentrations would be expected to impede spiking behaviour and eventually abolish spiking altogether, but not affect rate of spike generation. From the

model results, it is expected that the upstroke and plateau of the action potential is carried by calcium ions through the L-type current. Some small voltage fluctuations may occur on a rebound spike due to T-type current activation, however it is not expected that it will cause spiking behaviour. It is expected that the major contributor to pacemaking is the T-type current which is essentially sodium permeant in the heart, therefore pacemaking is not expected to be affected by reduced calcium concentration. Reducing calcium concentration would provide shorter plateaus and smaller upstroke peaks, ultimately leading to abolished spiking behaviour as described by Yeoman & Benjamin, 1999.

Action potential clamp of ventricle cells in the presence of outward potassium current blocks would reveal the net inward current during the action potential. It is expected that this inward current would follow the shape of the action potential. Using an L-type current blocker that does not interfere with the T-type current such as isradipine would separate T-type and L-type currents in the net inward current recorded. It is expected that the T-type current would be active before and at the beginning of the upstroke, while the L-type current would be active at the end of the upstroke and the plateau phase, as in the model. Determining when the T-type current is active during this protocol would contribute in defining its physiological role in the upstroke. If it is active through the entire upstroke, the sodium permeable T-type current is acting in place of the absent sodium channel current. This would also help to contrast its role against the L-type calcium current in terms of which current plays a more prominent role during the upstroke. The L-type current is expected to be the major contributor to the plateau phase and carry the upstroke to its peak after activation from the T-type current.

Prostate and albumen gland cells of *Lymnaea stangalis* have not previously been recorded, and channels aside from the 12b T-type isoform have not been studied in these cells. Since both cell types are primarily secretory and possess large quantities of vesicles as seen after cell dissociation, the cells would be expected to possess excitation-secretion coupling. Cells may not produce spontaneous spiking activity similar to the ventricle cells, and may

need an applied current to raise the potential to threshold for a spike. If action potentials are able to be produced by either cell type, they would likely be long and broad to allow significant increase of internal calcium concentration to allow vesicle release, likely due to an L-type current. The 12b current is likely present exclusively in these secretory cells to initiate excitation-secretion coupling.

Pacemaking and spike generation are likely both calcium dependent. The 12b T-type current is permeable to sodium and calcium, and reduced calcium concentrations would be expected to lower rate of spike generation contrary to the 12a current of the heart. Reduced calcium concentrations would also be expected to reduce the size and duration of any spikes and with sufficient reduction abolish spiking activity completely due to the dependence of calcium in secretion. Reducing sodium is expected to reduce frequency of spikes as well, but spiking activity may not be abolished in zero sodium due to the calcium permeability of the 12b T-type current. It is expected that any spikes generated by these cells would be largely calcium dependent with sodium contributing to its pacemaking ability and perhaps spike initiation.

A voltage ramp protocol of prostate and albumen cells in the presence of potassium channel blockers would reveal the inward currents present. An experiment similar to the ramp performed by Senatore et al., 2014 would be expected to yield similar results. It would be expected that the low voltage activated sodium and calcium permeable T-type current would activate at a lower potential, and a high activated L-type calcium current would activate once the T-type current had inactivated. A voltage ramp would also determine if the T-type and L-type currents are the only inward currents present in the prostate and albumen cells. Since sodium currents are very rapid with faster kinetics than T-type currents, it is not expected that a sodium current would be present in prostate or albumen gland cells as inward calcium current would likely be a higher priority to the cell than speed of conduction.

C.4 Improvements to Methods

Difficulties due to cell morphology and cell accessibility made it difficult to obtain electrophysiology results. Improvements to the methods may provide future success in performing these experiments.

The largest issue with sharp microelectrode recording of prostate and albumen cells was providing sufficient structural support to withstand mechanical pressure and having accessible cells on the gel surface. The collagen coated coverslips showed some adherence for prostate and albumen cells in order to transfer cells between different media, but were not sufficient to hold the cell in place while being touched by the pipette tip nor buzzed by the tip.

Future considerations can be made for alternate coatings such as the double layered collagen coated coverslip. The double layered collagen coverslip protocol involved covering glass coverslips with collagen solution, neutralizing with ammonium hydroxide to cause the collagen to gel, covering the coverslip once more with collagen solution and allowing this second layer to air dry (Grace Bio-labs). Other coatings using extracellular matrix constituents include fibronectin and laminin coatings. Alternatively, gelatin may also be used as a coverslip coating.

For electrophysiological recordings, using a coated coverslip for cells is ideal as they are always directly exposed to the external solution. Using agarose gel to to embed cells caused complications with cells not reaching the surface of the gel for exposure to the external solution. Yeoman & Benjamin, 1999 reported using agarose gel to embed ventricle cells for their microelectrode and patch clamp recordings, however this method did not provide accessible prostate or albumen cells for this study. It is possible that some cells were present at the surface of the gel, however for the cells recorded this was not the case. Recording cells contained completely inside the gel caused the pipette tip to become clogged and prevent recordings. This was apparent by visualizing the pipette penetrating the cell but seeing no drop in voltage through pClamp 10 software.

To improve the success rate for accessible cells on the surface of the gel, multiple organs could be dissected at once to increase the number of cells available for recording. Due to low snail populations, only one organ was dissected at a time for dissociation. Increasing this to up to three organs would provide more cells to give a higher chance of some reaching the surface. Further manipulation of the gel may be required to provide access to cells at the surface. Cell suspension may be added to the gel, allowed to cool and left for the cells to fall to the bottom. Inverting the gel itself within the dish may provide access to cells that have fallen to bottom of the gel. The gel may also be sliced into thin strips and examined for cells available at the surface.

Difficulties in whole cell patch clamp recording prostate, albumen and ventricle cells arose due to the morphology of the cell. Ventricle cells are reported to have several invaginations, and prostate and albumen cells are densely packed with vesicles. These features may prevent whole cell recording because of a lack of smooth surface necessary to form a seal with a pipette tip. Pipettes traditionally used for whole cell recording are low resistance and cover a relatively large surface area of the cell. Since accessing a large surface on these cell types poses problems, the protocol by Yeoman & Benjamin, 1999 may be followed instead.

Instead of pulling patch pipettes with a resistance between 2-5 MΩ, microelectrodes with resistances between 20-30 MΩ may be used instead. These sharp tips cover less surface area on the cell membrane than patch pipettes, and therefore are more likely to find a small patch of smooth membrane. These tips are also smaller than the vesicles found in prostate and albumen cells are would help prevent clogging. Pipettes were also filled with 3 M KCl as the internal solution. Using this method of voltage clamp recording may help yield results for action potential clamp of ventricle cells, and voltage ramp protocols for prostate and albumen cells.